

ISTANBUL TECHNICAL UNIVERSITY ★ INFORMATICS INSTITUTE

**MODELING OF BLOOD FLOW AND VESSEL WALL INTERACTION
FOR STENOSED CORONARY ARTERIES**

M.Sc. THESIS

Yağmur GÜLKANAT

Department of Computational Science and Engineering

Computational Science and Engineering Programme

MAY 2014

ISTANBUL TECHNICAL UNIVERSITY ★ INFORMATICS INSTITUTE

**MODELING OF BLOOD FLOW AND VESSEL WALL INTERACTION
FOR STENOSED CORONARY ARTERIES**

M.Sc. THESIS

**Yağmur GÜLKANAT
(702111009)**

Department of Computational Science and Engineering

Computational Science and Engineering Programme

Thesis Advisor: Prof. Dr. M. Serdar ÇELEBİ

MAY 2014

**TIKANIK KORONER DAMARLARDA KAN AKIŞI VE
DAMAR DUVARI MODELLEMESİ**

YÜKSEK LİSANS TEZİ

**Yağmur GÜLKANAT
(702111009)**

Hesaplamalı Bilim ve Mühendislik Anabilim Dalı

Hesaplamalı Bilim ve Mühendislik Programı

Tez Danışmanı: Prof. Dr. M. Serdar ÇELEBİ

MAYIS 2014

To my family...

FOREWORD

This thesis is about modeling blood flow and vessel wall interaction for the stenosed coronary arteries. Because of in vivo techniques are not enough, realistic computational modeling and simulations can prevent lots of diseases. I want to thank a lot to my thesis advisor M. Serdar Çelebi for all his helps, motivations and make me a part of this research activity. I am glad to be a part of this important research group. Also thanks to Şenol Pişkin, İbrahim Özküçük and our Computational Fluid Dynamics research group for their support.

May 2014

Yağmur GÜLKANAT

TABLE OF CONTENTS

	<u>Page</u>
FOREWORD	ix
TABLE OF CONTENTS	xi
ABBREVIATIONS	xiii
LIST OF TABLES	xv
LIST OF FIGURES	xvii
SUMMARY	xxi
ÖZET	xxiii
1. INTRODUCTION	1
1.1 Thesis Objective	1
1.2 Literature Review	2
2. BLOOD FLOW MODELING	17
2.1 Introduction	17
2.2 Constituents of Human Blood	17
2.3 Navier-Stokes Equations	18
2.3.1 Velocity field.....	18
2.3.2 Turbulence	19
2.3.3 Applicability	19
2.3.3.1 Continuity equation	20
2.4 Viscous and Inviscid Flow	20
2.5 Laminar and Turbulent Flow	21
2.5.1 $K-\omega$ sst turbulence model.....	23
2.6 Newtonian and Non-Newtonian Fluids	24
2.6.1 Non-Newtonian Carreau model.....	25
3. VESSEL WALL	27
3.1 Introduction	27
3.2 Governing Equations	29
3.2.1 Constitutive equations for hyperelastic material	29
3.2.1.1 Fung-elastic material	30
4. FLUID-STRUCTURE COUPLING MODELS	33
4.1 Introduction	33
4.2 Monolithic	33
4.3 Partitioned.....	34
4.3.1 Loose-coupling	34
4.3.2 Tight-coupling	35
5. NUMERICAL SIMULATIONS AND RESULTS	37
5.1 Introduction	37
5.2 Pre-processing for Simulations.....	37

5.3 Test Cases	40
5.3.1 Fixed model	40
5.3.1.1 Flow in cylindrical pipe without stenosis	40
5.3.1.2 Flow in cylindrical stenosed pipe	46
5.3.1.3 Flow in cylindrical stenosed pipe with bypass	50
5.3.2 FSI model	65
5.4 Results and Discussions	67
6. CONCLUSION	71
REFERENCES.....	73
CURRICULUM VITAE.....	79

ABBREVIATIONS

CVD	: Cardiovascular disease
CFD	: Computational fluid dynamics
ALE	: Arbitrary Lagrangian-Eulerian
AML	: Adaptive modeling language
CT	: Computed tomography
FEM	: Finite element method
GMRES	: Generalized minimal residual
WSS	: Wall shear stress
MCA	: Middle cerebral artery
FSI	: Fluid-structure interaction
SSTFSI	: Stabilized space-time fluid-structure interaction
NURBS	: Non-uniform rational B-splines
PAE	: Peri-aneurysmal environment
MR	: Magnetic resonans
AAA	: Abdominal aortic aneurysm
DSD	: Deforming-spatial-domain
SST	: Stabilized space-time
LVAD	: Left ventricular assist device

LIST OF TABLES

	<u>Page</u>
Table 2.1 : Bird-Carreau model constitutive law parameters.....	26
Table 5.1 : Bird-Carreau model parameters.....	44

LIST OF FIGURES

	<u>Page</u>
Figure 1.1 : Instantaneous distributions of velocity in the particular cross-sections. [5] (The vectors indicate the flow patterns of secondary flow while the color contours indicate the distributions of axial velocity.)	3
Figure 1.2 : Detail of the surface of the finite-element grids generated using sources (a) and adaptive background grids (b) to specify the element size distribution [6].	4
Figure 1.3 : Velocity field and WSS distribution of 2 ruptured aneurysms. The velocity field in cross-sectional plane (upper) and the WSS distribution in 3-D geometry (lower) are shown. Black arrowheads indicate the site of moderately elevated WSSs in the aneurysm region. Yellow arrows and lines show the site of a markedly low WSS area and the flow stasis with recirculating zones at the tip of the aneurysm, respectively. The numbers near the arrows indicate the magnitude of WSSs at the sites [7].	5
Figure 1.4 : Streamlines in the terminal aneurism (A1 model, left) and in side aneurism (A2M3 model, right) at phase 2 [8].	6
Figure 1.5 : Carotid-artery bifurcation. Flow field at various instants. Velocity vectors coloured by magnitude [9].	7
Figure 1.6 : Flow in a patient-specific abdominal aorta with aneurysm. (a) Patient-specific imaging data; (b) Skeleton of the NURBS mesh; (c) Smoothed and truncated NURBS model and mesh. In c, every NURBS patch is assigned a different color [10].	8
Figure 1.7 : (a) Aneurysms with concentrated inflow jet and regions of locally elevated wall shear stress (WSS) (top panels) and with diffuse inflow jet and WSS uniformly lower than the parent artery (bottom panels). (b) Aneurysms with large (top panels) and small (bottom panels) impingement regions compared to the aneurysm size [15]. ..	9
Figure 1.8 : Wall shear stress in the deforming geometry at end-diastole (a), peak-systole (b), late-systole (c), end-systole (d), and mid-diastole (e) in the fourth period [22].	10
Figure 1.9 : Patient-specific abdominal aorta mesh consisting of 52,420 quadratic NURBS elements [23].	11
Figure 1.10 : Flow velocity in Model 2 (left: elastic wall, right: rigid wall). (a) Cutting plane for Section A. (b) Velocity vectors at Section A. (c) Velocity magnitude at Section B. (d) Velocity magnitude at Section C [24].	12
Figure 1.11 : Transient behavior of the velocity distribution in Section A for the elastic wall model [25].	12

Figure 1.12: Transient behavior of the velocity distribution in Section A for the rigid wall model [25].	13
Figure 1.13: Instantaneous principal-stress distributions [26].	13
Figure 2.1 : Blood features.	18
Figure 2.2 : Laminar flow of an incompressible fluid of viscosity η through a tube of length l and radius r .	21
Figure 2.3 : Human blood viscosity varies dynamically during each cardiac cycle. At systole, blood is thinner, while at diastole, blood is 2-5 times thicker.	21
Figure 2.4 : Laminar vs. turbulent flow in a pipe.	22
Figure 2.5 : Reynolds number for laminar and turbulent flow in a pipe.	22
Figure 2.6 : Shear/strain relationship for a Newtonian fluid.	25
Figure 2.7 : Variation of viscosity with shear rate according to the Carreau model.	26
Figure 3.1 : Structure of blood vessels walls.	27
Figure 4.1 : Loose-Coupling solver sequence.	35
Figure 4.2 : Tight-Coupling solver sequence with fixed point iteration with under-relaxation.	36
Figure 5.1 : Cylindrical pipe without stenosis.	38
Figure 5.2 : Inlet of the cylindrical pipe.	38
Figure 5.3 : Mesh of solid part for FSI.	38
Figure 5.4 : Stenosed pipe.	39
Figure 5.5 : Grid for the stenosis region.	39
Figure 5.6 : Numerical grid used for the stenosed bypass simulation.	39
Figure 5.7 : Inlet of the stenosed pipe with bypass.	40
Figure 5.8 : Intersection region as seen from the inside of the broad branch.	40
Figure 5.9 : Velocity in cylindrical pipe without stenosis.	41
Figure 5.10: Pressure in cylindrical pipe without stenosis.	41
Figure 5.11: Residuals of the flow.	41
Figure 5.12: Womersley velocity inlet profile.	42
Figure 5.13: Residuals of the flow.	42
Figure 5.14: Velocity profile for constant value inlet.	43
Figure 5.15: Velocity profile for womersley inlet profile.	43
Figure 5.16: Taking a point at the center of the slice that took in the middle of the vessel.	44
Figure 5.17: The point on the top of the slice (pink one).	44
Figure 5.18: Comparison of wall shear stress distribution.	45
Figure 5.19: Comparison of pressure distribution.	45
Figure 5.20: Comparison of velocity distribution.	46
Figure 5.21: Slices that analyzed on the stenosed pipe.	46
Figure 5.22: Comparison of wall shear stress distribution.	47
Figure 5.23: Comparison of pressure distribution.	47
Figure 5.24: Comparison of velocity distribution.	47
Figure 5.25: Comparison of wall shear stress distribution.	48
Figure 5.26: Comparison of pressure distribution.	48
Figure 5.27: Comparison of velocity distribution.	48

Figure 5.28: Comparison of wall shear stress distribution.	49
Figure 5.29: Comparison of pressure distribution.	49
Figure 5.30: Comparison of velocity distribution.	49
Figure 5.31: Slices that are analyzed on the stenosed pipe.	50
Figure 5.32: Comparison of wall shear stress distribution.	50
Figure 5.33: Comparison of pressure distribution.	51
Figure 5.34: Comparison of velocity distribution.	51
Figure 5.35: Comparison of wall shear stress distribution.	52
Figure 5.36: Comparison of pressure distribution.	52
Figure 5.37: Comparison of velocity distribution.	53
Figure 5.38: Comparison of wall shear stress distribution.	53
Figure 5.39: Comparison of pressure distribution.	54
Figure 5.40: Comparison of velocity distribution.	54
Figure 5.41: Comparison of wall shear stress distribution.	55
Figure 5.42: Comparison of pressure distribution.	55
Figure 5.43: Comparison of velocity distribution.	56
Figure 5.44: Comparison of wall shear stress distribution.	56
Figure 5.45: Comparison of pressure distribution.	57
Figure 5.46: Comparison of velocity distribution.	57
Figure 5.47: Comparison of wall shear stress distribution.	58
Figure 5.48: Comparison of pressure distribution.	58
Figure 5.49: Comparison of velocity distribution.	59
Figure 5.50: Comparison of wall shear stress distribution.	59
Figure 5.51: Comparison of pressure distribution.	60
Figure 5.52: Comparison of velocity distribution.	60
Figure 5.53: Comparison of wall shear stress distribution.	61
Figure 5.54: Comparison of pressure distribution.	61
Figure 5.55: Comparison of velocity distribution.	62
Figure 5.56: Comparison of wall shear stress distribution.	62
Figure 5.57: Comparison of pressure distribution.	63
Figure 5.58: Comparison of velocity distribution.	63
Figure 5.59: Comparison of wall shear stress distribution.	64
Figure 5.60: Comparison of pressure distribution.	64
Figure 5.61: Comparison of velocity distribution.	65
Figure 5.62: Comparison of wall shear stress distribution.	66
Figure 5.63: Comparison of pressure distribution.	66
Figure 5.64: L: Length of the vessel, l: Length of stenosis region.	68
Figure 5.65: d1: Diameter of the vessel, d2: Diameter of stenosis region, l1: Length of stenosis region, l2: Length of stenosis.	68
Figure 5.66: L: Length of bypass, a1,a2: Angle of bypass inlet and outlet, d1,d2: Distance of bypass inlet and outlet from the stenosis region.	69

MODELING OF BLOOD FLOW AND VESSEL WALL INTERACTION FOR STENOSED CORONARY ARTERIES

SUMMARY

Cardiovascular diseases, including infarction, thrombosis, atherosclerosis and aneurism, are one of the most important health problems of the world. Because of the in vivo techniques are not enough to prevent these diseases, computational modeling and simulations have an important role to analyse the hemodynamic factors, like wall shear stress, that lead to these diseases. So it is important to model the vessel and the flow and get the velocity, pressure and wall shear stress results to compare, analyse and maybe prevent the disease before it happens.

The aim of this study is to model blood flow and the vessel wall interaction and try to understand the basic role and the impact of hemodynamic parameters. We have two cases, for the first one, we will model the blood flow by assuming the vessel wall is rigid, and for the second one we will model the blood flow and vessel wall interaction (FSI case). For these cases, we have constructed three different geometries, first is the vessel without stenosis, second is the vessel with stenosis and the third is the vessel with stenosis and bypass. First, it will be shown that womersley velocity profile gives more realistic results as an incoming blood flow condition. Second, it will be demonstrated that non-Newtonian flow gives more realistic results compared to Newtonian model because the blood exhibits non-Newtonian characteristics. Then for all cases, non-Newtonian flow is used. For non-Newtonian flow, Bird-Carreau model is used. The flow is modeled both laminar and turbulent. And for turbulent flow, $k-\omega$ shear stress transform (STT) model is used. Hyperelastic solid mechanics model based on Fung's material parameters is used for the vessel wall. A nonNewtonianIcoFoam solver is used for laminar case for rigid body, that solves incompressible non-Newtonian fluid. For fluid-structure interaction, OpenFOAM has only icoFsiFoam solver, which we can not use it because it does not solve non-Newtonian flow. So nonNewtonianIcoFsiFoam solver has to be created by modifying nonNewtonianIcoFoam. And for turbulent case, a simpleFoam solver is used for rigid body, that solves incompressible non-Newtonian turbulent flow. For fluid-structure interaction case, simpleFsiFoam solver has to be created by using simpleFoam solver. Results are obtained and compared for two cases. Our results show that blood flow and vessel wall interaction gives more realistic results, especially for the wall shear stress, where differences are up to % 50 percentage.

TIKANIK KORONER DAMARLARDA KAN AKIŞI VE DAMAR DUVARI MODELLEMESİ

ÖZET

Damar tıkanıklığı, kan pıhtılaşması, damar sertleşmesi ve damar genişlemesi hastalıklarını içeren kardiyovasküler (kalp ve damarla ilgili) hastalıklar dünyadaki en önemli sağlık sorunlarından biridir ve dünya genelinde ölümlerin çoğu bu hastalıklar yüzünden meydana gelmektedir. Hastalar üzerinde uygulanan teknikler bu hastalıkları önlemekte yeterli olmadığı için, bu hastalıklara neden olan duvar kayma gerilmesi (wall shear stress), basınç ve hız gibi hemodinamik (kan dolaşım) etkenleri analiz etmekte hesaplamalı modelleme ve simülasyonlara önemli bir rol düşmektedir. Bu nedenle damar duvarı ve kan akışını modelleyerek hız, basınç ve duvar kayma gerilmesi sonuçlarını elde etmek, analiz etmek ve karşılaştırmak, olası sonuçları incelemek, belki de bu hastalıkları meydana gelmeden önleyebileceği için çok önemlidir.

Bu çalışmanın amacı, kan akışı ve damar duvarı etkileşimini modelleyerek hemodinamik etkenleri anlamaya ve analiz etmeye çalışmaktır. Bu çalışmada iki durum inmiştir, ilk durumda damar duvarını hareketsiz kabul ederek, kan akışı modellenmiştir. İkinci durumda ise kan akışı ve damar duvarının etkileşimi (FSI) modellenmiş ve iki durum için aradaki hemodinamik farklılıklar incelenmiştir.

Modellemenin ilk adımı olan geometri oluşturma kısmında OpenFOAM yazılımı kullanılarak üç farklı geometri oluşturuldu, ilk geometri tıkanık olmayan silindirik damar, ikinci geometri ortasında simetrik bir tıkanıklık olan silindirik damar ve üçüncü geometri ise tıkanıklık olan ve bypass uygulanmış silindirik damar şeklinde oluşturuldu. Bu geometrilere altı yüzlü (hexahedral) ağ (mesh) atıldı. Başlangıç ve sınır değer koşulları oluşturularak, çözücü (solver) ayarları yapıldı. Simülasyon sonucu karşılaştırmaları için ilk olarak akışın giriş koşulu olarak Womersley hız profili ve sabit hız profili verildi. Geometrilerin belirli bölgelerinden kesitler alınarak, belli noktalardaki hemodinamik etkenlerin ve hızın zamana bağlı değişimi analiz edildi. Womersley hız profilinin, gelişmiş bir akış profiline sahip olması ve üç boyutlu veri olması nedeniyle, daha gerçekçi sonuçlar verdiği gösterildi. Bu nedenle daha sonraki simülasyonlar için giriş hızı olarak hep Womersley hız profili verildi. İkinci adım olarak, akış koşulları olarak Newtonian, Newtonian olmayan ve türbülanslı akış modeli kabulleri yapıldı. Bu üç koşulun sonuçları tüm geometriler için belirli yerlerde kesitler alınarak bu kesitlerin belli noktalarında zamana bağlı incelenerek karşılaştırıldı. Kan Newtonian olmayan bir akış özelliğine sahip olduğu için, Newtonian olmayan akış modellemesinin diğer modellemelere göre daha gerçekçi sonuçlar verdiği görüldü. Ayrıca tıkanıklık ve bypassın olduğu bölgelerde akışın daha dar geometrilerden geçmesinden dolayı dalgalanmalar meydana geldiği için, akışın Newtonian olmayan ve aynı zamanda türbülanslı olan kabulünün bu bölgelerde daha gerçekçi sonuçlar verdiği ortaya konuldu. Newtonian olmayan akış modellenirken, Newtonian olmayan Bird-Carreau model ve parametreleri kullanıldı. Kan akışı, laminer ve türbülanslı olarak iki durumda çözüldü.

Türbülanslı akış için $k-\omega$ kayma gerilimi taşınımı (SST) modeli ve parametreleri kullanıldı.

Tüm bu hareketsiz damar ve kan akışı etkileşimi simülasyon sonuçları elde edildikten sonra, hareketli damar ve kan akışı etkileşimi incelenmiştir. Akış için ayrı, damar duvarı için ayrı geometriler oluşturulup, iki geometriye de altı yüzlü ve eşit sayıda ağ atılmıştır. Damar duvarını modellerken, Fung'un madde parametrelerini baz alan hiperelastik katı mekaniği modeli ve parametreleri kullanılmıştır. Başlangıç ve sınır şartları belirlendikten sonra çözücü ayarları yapılmıştır. Hareketsiz damar modellenirken, sıkıştırılamayan, Newtonian, laminer akışları çözen icoFoam çözücüsü, Newtonian olmayan akışlar için, sıkıştırılamayan, laminer akışları çözen nonNewtonianIcoFoam çözücüsü, türbülanslı akış için ise simpleFoam çözücüsü kullanılmıştır. OpenFOAM yazılımı, akış ve hareketli damar duvarı etkileşimi modellemeleri için sadece laminer ve Newtonian akış çözen icoFsiFoam çözücüsünü içermektedir, bu nedenle kan akışı ve damar duvarı etkileşimi laminer ve Newtonian akış koşulları kabul ederek çözülmüştür. FSI iki türlü bağlama (coupling) yöntemi içermektedir, bunlar gevşek bağlama (loose coupling) ve sıkı bağlama (tight coupling) olarak adlandırılmaktadır. Bu çalışmada kullanılan icoFsiFoam çözücüsü gevşek bağlama yöntemi ile FSI modellemesini çözmektedir. Simülasyon için ilk deneme olarak Womersley giriş hız profili değil, sabit giriş hız profili kullanılmıştır. Elde edilen sonuçlar, Newtonian, Newtonian olmayan ve türbülanslı akış modellemelerin sabit giriş hız profili sonuçları ile karşılaştırılmıştır. FSI modelinin, duvar kayma gerilmesi ve basınç hemodinamik etkenlerinde daha gerçekçi sonuçlar verdiği gösterilmiştir. Özellikle, sabit damar modeli ve hareketli damar modeli karşılaştırıldığında, duvar kayma gerilmeleri farkının % 50'ye kadar çıkabildiği görülmüştür.

Bu çalışmalar, ilk adım olarak Womersley giriş profili eklenerek devam edecek ve OpenFOAM yazılımının FSI için halihazırda bulunan çözücülerini değiştirerek devam edecektir. Örneğin Newtonian olmayan FSI çözümlerini elde edebilmek için, Newtonian akışı çözen icoFsiFoam çözücüsü değiştirilerek, Newtonian olmayan parametreler eklenerek nonNewtonianIcoFsiFoam gibi, kendi problemimize yönelik yeni bir çözücü oluşturulacaktır. Daha sonra bu çözücüye, Newtonian olmayan ve türbülanslı olan modelleri çözen simpleFoam çözücüsü eklenerek türbülans modeli çözen simpleFsiFoam gibi yeni bir çözücü oluşturmak gerekmektedir. Ayrıca icoFsiFoam çözücüsü değiştirilerek sıkı bağlama (tight coupling) yapan bir çözücü oluşturup icoFsiFoam çözücüsünden elde edilen sonuçlar ile karşılaştırılacaktır. Tüm bu çözücüler oluşturulup simülasyonlar yapılarak sonuçlar karşılaştırılmalı ve hemodinamik etkenler yorumlanmalıdır. Bu çalışmadan daha sonra parametrik çalışmalar yapılacaktır. Örneğin tıkanıklığın derinliği, uzunluğu veya bypass için eklenen damarın giriş ve çıkış noktaları ve uzunluğu gibi parametreler değiştirilerek elde edilen sonuçlar, tüm hemodinamik faktörler için karşılaştırılacaktır ve yorumlanacaktır.

Tüm bu analizler, damar tıkanıklığı, kan pıhtılaşması, damar sertleşmesi ve damar genişlemesi gibi kardiyovasküler hastalıkları meydana getiren etkenleri incelemek, yorumlamak ve anlamak için yapılmaktadır. Bu analiz ve modellemeler, bu alandaki teorik bilgilere dayanılarak uygulama olarak yapılmaktadır. Önce yapay geometriler oluşturularak başlayan çalışmalar, son yıllarda dünya çapında yapılan modellemelerde, hastanelerden alınan gerçek hasta verileri ile yapılmakta ve hastaya özgü sonuçlar üretilebilmektedir. Bu şekilde hesaplamalı modellemeler ile hastalıkların çözümünde ilerlemeler kaydedilmesi beklenmektedir. Hatta bu çalışmadaki bypass

simülasyonlarından elde edilen sonuçların yorumlanması ile, bypass ameliyatlarında eklenen damarın hangi noktalardan, ne kadar uzunlukta ve ne kadar açıyla eklendiğinde daha iyi sonuçlar verdiği, kanın akışının hangi koşullarda en iyi şekilde olduğu incelenebilir ve en iyi koşul seçilerek, hastanın ömrünü daha fazla uzatmak bu şekilde olası olabilir. Bu nedenle hesaplamalı modelleme, simülasyon ve analiz, uygulamalı bilimler için önemli bir araştırma dalıdır.

1. INTRODUCTION

In this thesis, blood flow and vessel wall interaction is studied with the stenosed coronary arteries to study the hemodynamic flow characteristics. Hemodynamic factors are known to affect a number of cardiovascular disease, so it is important to understand the relations between cardiovascular diseases and hemodynamic factors. Because of the in vivo measurement techniques capabilities are not enough, computer modeling is important. For a long time, researchers studied the blood flow by assuming the vessel wall is rigid but then some techniques are developed and fluid-structure interactions (FSI) are included into the simulations. Rigid and FSI models are compared and it is showed that FSI modeling gives more realistic results. Here in this study, initially the vessel wall is assumed as rigid and blood flow is modeled with rigid vessel wall interaction. Then fluid-structure interaction is modeled between the blood flow and vessel wall. In our simulations, blood flow is assumed as non-Newtonian flow based on Carreau model and considered as mild-turbulent flow based on $k-\omega SST$ (shear stress transform) turbulence model. Finally results are compared to show that FSI model gives more realistic results.

1.1 Thesis Objective

Our main objective is to model the blood flow and vessel wall interaction for the stenosed coronary arteries. Three dimensional stenosed vessel geometries are created by OpenFOAM, a free, open source CFD software package. Womersley velocity profile is used as input at the inlet of the stenosed vessel. The vessel wall is modeled as hyper elastic model and its coupled effects with blood flow is included in our model. The strong-coupling model is used for the blood flow and vessel wall interaction. A quadrilateral mesh is used for the surface and hexahedral mesh is used for volume of stenosis geometry. Minimum mesh size is obtained by using converging criteria for modeling blood flow physics and for vessel wall geometry to model the actual physical phenomena properly. By using this model, our aim is both to identify the actual flow

dynamics parameters for resulting early deflections in stenosed geometry, and to model blood flow in rigid wall and implement fluid-structure interaction (FSI) for the blood flow and stenosed vessel then comparing the results. By this way, it will be showed that FSI approach gives more realistic results for the hemodynamic factors that is tested.

1.2 Literature Review

Cardiovascular disease (CVD) including infarction, thrombosis, atherosclerosis, stenosis and aneurism is one of the most important health problem for the people all around the world. [1–3]. And hemodynamic factors are known to affect a number of CVD including atherosclerosis and aneurysm. Because of the in vivo measurement techniques capabilities are not enough, computer modeling is playing an important role for a better understanding of the relations between the CVD and hemodynamic factors. In recent years, researchers, who wants to simulate blood flow in three-dimensional model of arteries, have widely used the computational techniques. These techniques applied to model blood flow in arteries examined only the velocity field, not pressure field, vessel walls treated as rigid [4–8] or considered significantly simplified or reduced geometries of deformable wall models [9, 10]. Also flow analysis are studied of three dimensional arteries using realistic geometry and numerical blood flow simulation with predefined artery movement is studied by Piskin et al. [11, 12] and three dimensional blood flow simulation at the geometry of thirteen main arteries are studied by Aribas et al. [13].

For more details, for example in [4], Taylor et al. solved three-dimensional, transient flow equations in deforming blood vessels with arbitrary Lagrangian-Eulerian (ALE) description of continuous media in which the fluid and solid domains are allowed to move to follow the distensible vessels and deforming fluid domain. And as a first approximation, the vessel walls are treated as being rigid, in diseased vessels which are often the subject of interest, the arteries are even less compliant and wall motion is further reduced. And they assumed the flow as Newtonian fluid flow. For the inlet profile, they used Womersley solution for fully developed pulsatile flow in a straight circular cylinder. The Adaptive Modeling Language (AML), the knowledge-based engineering and object modeling software used to create the integrated system. Quantities of interest including pressure and velocity fields, wall shear stress distributions, and particle residence times are studied. And they got all result by assuming the vessel wall as rigid.

Also in [5], Oshima et al. constructed three-dimensional solid model from the computed tomography (CT) angiography raw data. The finite element method (FEM) is used in order to simulate flow in a complicated geometry. Blood flow is considered to be Newtonian. The simulation is conducted to investigate hemodynamics of blood flow in the carotid siphon under real flow conditions measured by Doppler ultrasound velocimetry technique. Hexahedral meshes are used created by ICEM CFD software. Pulsatile boundary condition is prescribed on the infow boundary. In reality, the artery walls are elastic but here, the walls are assumed rigid walls with no-slip boundary conditions. The results are visualized for a better understanding of the flow characteristics such as distributions of the flow pattern and the wall shear stress in the carotid siphon. See the Figure 1.1 for instantaneous distributions of velocity in the particular cross-sections. The distribution of the wall shear stress showed high magnitudes in the area where the carotid siphon starts to bend. The distribution varied with the cardiac cycle, and its variation in time tended to become large in the areas of high shear stress. It was found that secondary flow becomes quite large downstream of the carotid siphon due to curvature. The numerical results showed that the magnitudes of secondary flow velocity downstream area were 10-20% of that of axial velocity.

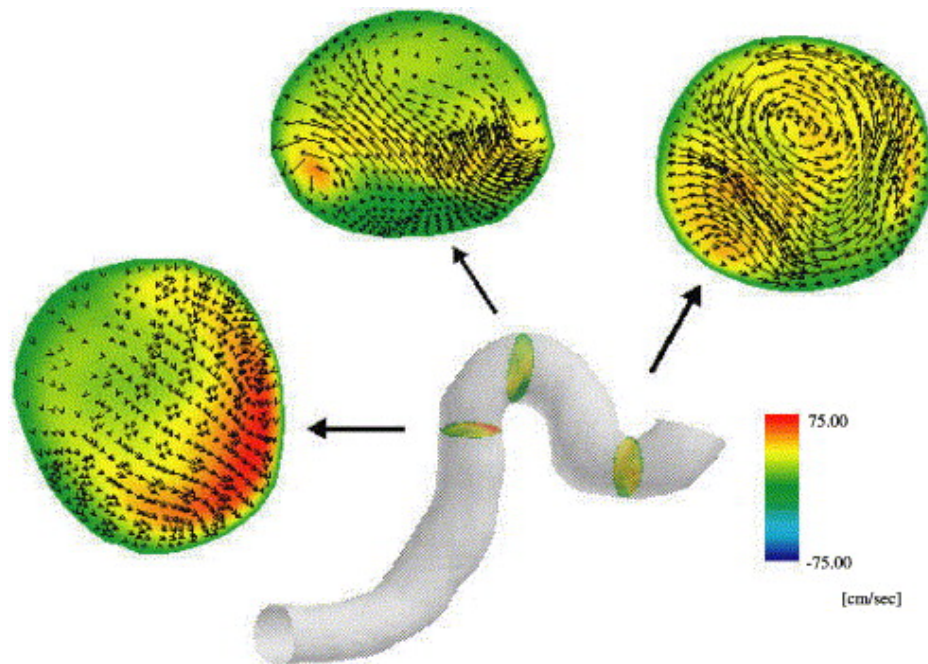


Figure 1.1: Instantaneous distributions of velocity in the particular cross-sections. [5]
(The vectors indicate the flow patterns of secondary flow while the color contours indicate the distributions of axial velocity.)

In [6], Cebal et al. studied on image-based methodology for constructing patient-specific models of the cerebral circulation. This methodology combines anatomical and physiologic imaging techniques with computer simulation technology and illustrated with a finite element model constructed from magnetic resonance image data of a normal volunteer. They used unstructured grids composed of tetrahedral elements because of their geometrical flexibility, see in Figure 1.2. A CFD simulation was then performed using the non-Newtonian model of Casson. Periodicity in the pulsatile flow field was achieved in less than two cardiac cycles. Blood is mathematically modeled as a time-dependent viscous incompressible fluid.

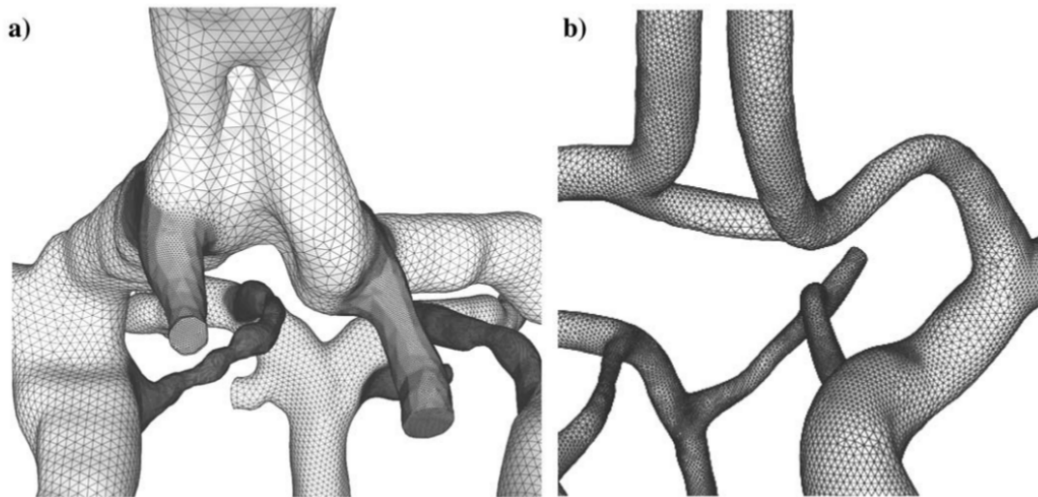


Figure 1.2: Detail of the surface of the finite-element grids generated using sources (a) and adaptive background grids (b) to specify the element size distribution [6].

In [7], Shojima et al. analyzed the magnitude and distribution of the WSS in and around human middle cerebral artery (MCA) aneurysms using the method of computational fluid dynamics (CFD). Twenty mathematical models of MCA vessels with aneurysms were created by 3-dimensional computed tomographic angiography. Blood was assumed to be an incompressible isothermal Newtonian fluid with a specific gravity of 1000 kg/m^3 and a viscosity of $4.0 \times 10^{-3} \text{N}/\text{m}^2$ per second. The viscoelastic properties of the vessel wall were neglected and a rigid wall with no-slip condition was applied. For the inlet condition, a pulsatile flow with a Womersley velocity profile was simulated. CFD calculations were performed by using their original finite-element solver with the assumption of Newtonian fluid property for blood and the rigid wall property for the

vessel and the aneurysm. As a result, they showed that in contrast to the pathogenic effect of a high WSS in the initiating phase, a low WSS may facilitate the growing phase and may trigger the rupture of a cerebral aneurysm by causing degenerative changes in the aneurysm wall, see in Figure 1.3. The WSS of the aneurysm region may be of some help for the prediction of rupture.

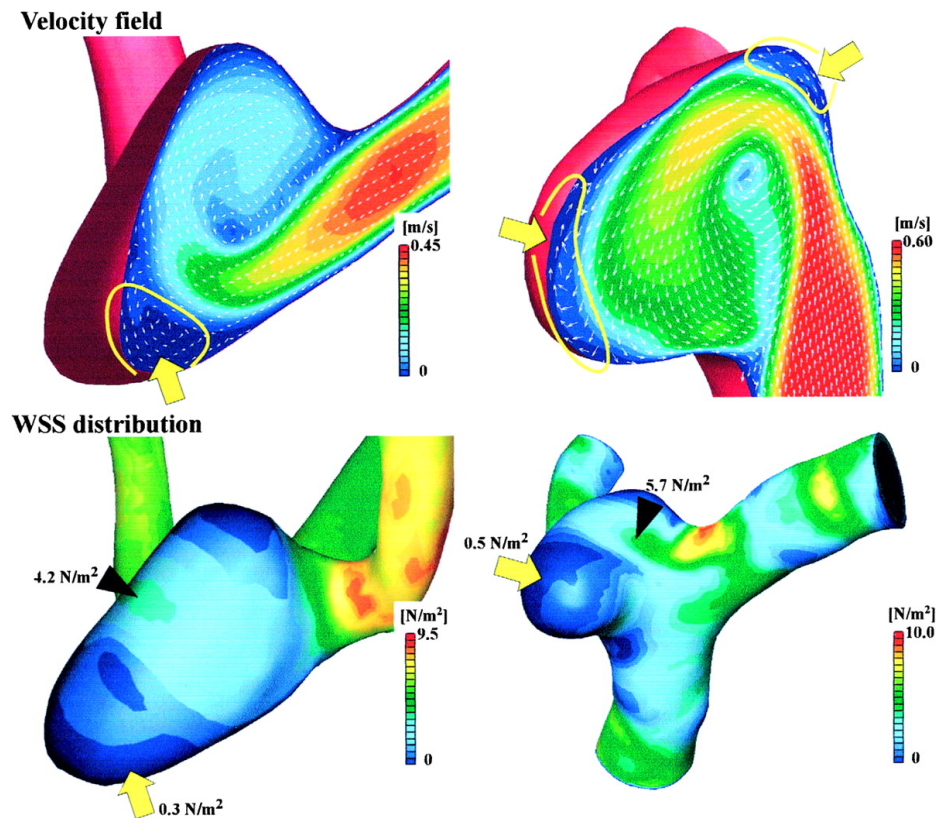


Figure 1.3: Velocity field and WSS distribution of 2 ruptured aneurysms. The velocity field in cross-sectional plane (upper) and the WSS distribution in 3-D geometry (lower) are shown. Black arrowheads indicate the site of moderately elevated WSSs in the aneurysm region. Yellow arrows and lines show the site of a markedly low WSS area and the flow stasis with recirculating zones at the tip of the aneurysm, respectively. The numbers near the arrows indicate the magnitude of WSSs at the sites [7].

In [8], Salmon et al. studied about saccular aneurysms, see Figure 1.4. They assumed vessel wall to be rigid and used the finite element method for numerical simulations, performed in three-dimensional aneurysms. A geometrical model is obtained to be meshed for a finite element use. The pulsatile flow of incompressible Newtonian blood is illustrated by numerical simulations carried out in two saccular aneurysm types, a side- and a terminal-aneurysm. High pressure zones are observed in the aneurysm cavity,

especially in the terminal one. As a result, they suppose that there is a risk of wall rupture where the aneurism pressure is high, assuming that the within-wall high stress concentration is correlated to high pressure.

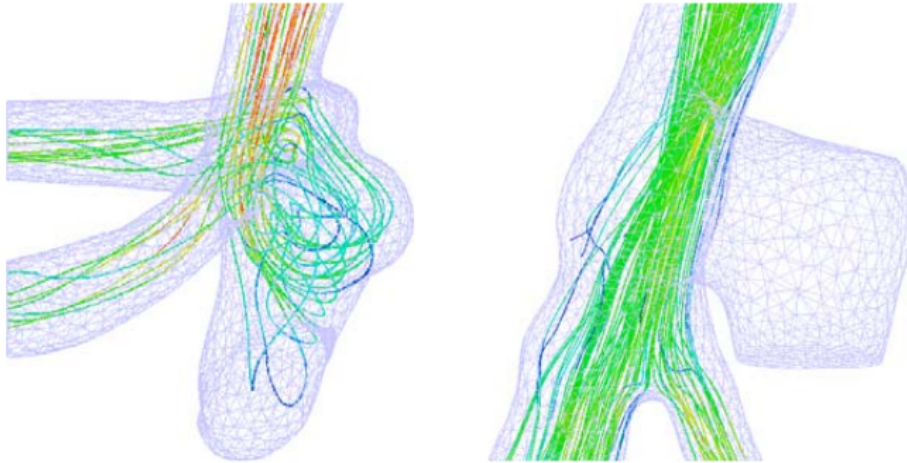


Figure 1.4: Streamlines in the terminal aneurism (A1 model, left) and in side aneurism (A2M3 model, right) at phase 2 [8].

After all studies that assume the vessel wall rigid, to find more realistic results, researchers studied more about fluid-structure interaction (FSI) because the blood flow depends on the arterial geometry, and the deformation of the arterial wall depends on the blood flow. The equations governing the blood flow and arterial deformation need to be solved simultaneously, with proper kinematic and dynamic conditions coupling the two physical systems.

In [9], Tezduyar et al. applied the stabilized space–time fluid–structure interaction (SSTFSI) techniques developed by the Team for Advanced Flow Simulation and Modeling (T \star AFSM) to FSI modelling in arterial fluid mechanics. Test computations are presented for cerebral and abdominal aortic aneurysms and carotid-artery bifurcation, where the arterial geometries used in the computations are close approximations to the patient-specific image-based data, see in Figure 1.5. Test computations with the continuum element are carried out for both linearly elastic and hyperelastic (Mooney–Rivlin) materials. With the test computations presented, they showed that the new SSTFSI techniques can successfully deal with different types of arterial problems and structural models.

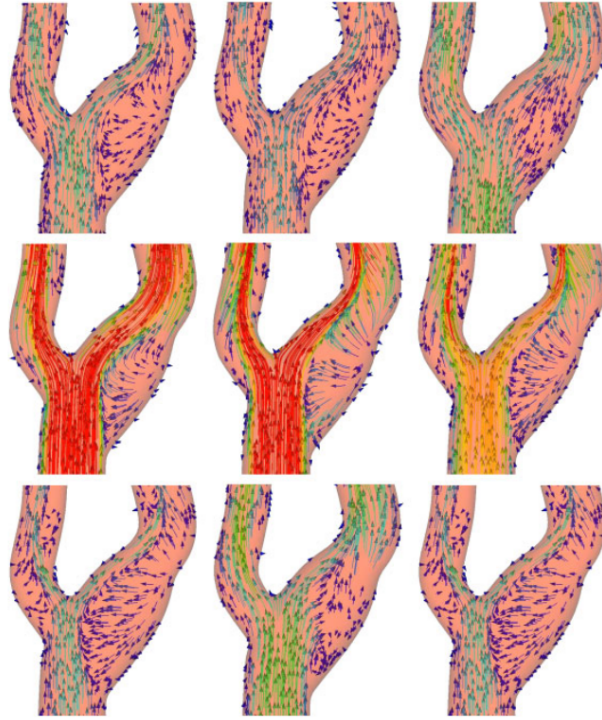


Figure 1.5: Carotid-artery bifurcation. Flow field at various instants. Velocity vectors coloured by magnitude [9].

And also in [10], Bazilevs et al. presented a fully-coupled monolithic formulation of the fluid-structure interaction of an incompressible fluid on a moving domain with a nonlinear hyperelastic solid. The arbitrary Lagrangian–Eulerian description is utilized for the fluid subdomain and the Lagrangian description is utilized for the solid subdomain. Particular attention is paid to the derivation of various forms of the conservation equations; the conservation properties of the semi-discrete and fully discretized systems; a unified presentation of the generalized- α time integration method for fluid-structure interaction; and the derivation of the tangent matrix, including the calculation of shape derivatives. A NURBS-based isogeometric analysis methodology is used for the spatial discretization and three numerical examples are presented which demonstrate the good behavior of the methodology, see in Figure 1.6.

Under normal conditions, wall deformability doesn't significantly change the velocity field and because of coupling blood flow and vessel wall was very difficult to solve, the rigid-wall approximation widely used for a long time as it's seen in [9]. But this approximation is valid when the wall motion is small. And when the deformation is larger, rigid-wall approximation gives us the wrong results of the hemodynamic factors as wall shear stress (WSS), one of the most studied quantity because it is connected

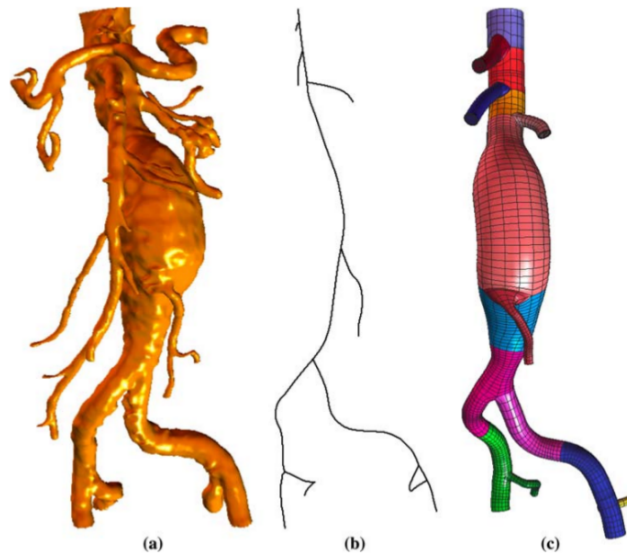


Figure 1.6: Flow in a patient-specific abdominal aorta with aneurysm. (a) Patient-specific imaging data; (b) Skeleton of the NURBS mesh; (c) Smoothed and truncated NURBS model and mesh. In c, every NURBS patch is assigned a different color [10].

with the origination and progression of CVD [14, 15].

In [14], Shaaban et al. describes the importance of wall shear stress. As a result, they established the relation between wall shear stress and the development and progression of atherosclerosis. They showed that, low and oscillating wall shear stress seems to favor the development of atherosclerosis as determined by the inverse relation between wall shear stress and arterial wall thickness. Wall shear stress also seems to depend on age, blood pressure, and body mass index. The value of wall shear stress is subject-specific and vessel-specific. Wall shear stress varies along the same vessel and around the vessel circumference.

In [15], Sforza et al. review recent progress on the basic mechanisms of aneurysm formation and evolution, with a focus on the role of hemodynamic patterns, see in Figure 1.7. As a result, they showed that the role of blood-flow physiological parameters regulating aneurysm morphology and natural history is poorly understood. It is necessary to model intra-aneurysmal hemodynamics using realistic aneurysm geometries because aneurysm geometry is one of the most important factors determining aneurysm flow patterns and WSS distributions that influence aneurysm progression. Most models tend to oversimplify the complex flow patterns observed in aneurysms in vivo. The difficulty of developing reliable in vitro and animal models has

hampered an accurate evaluation of those physiologic parameters. Furthermore, better understanding of the mechanisms of aneurysmal growth requires the study of the interaction among hemodynamics, wall mechanobiology, wall biomechanics, and contacts with the peri-aneurysmal environment (PAE) structures. This will help improve patient evaluation and treatment.

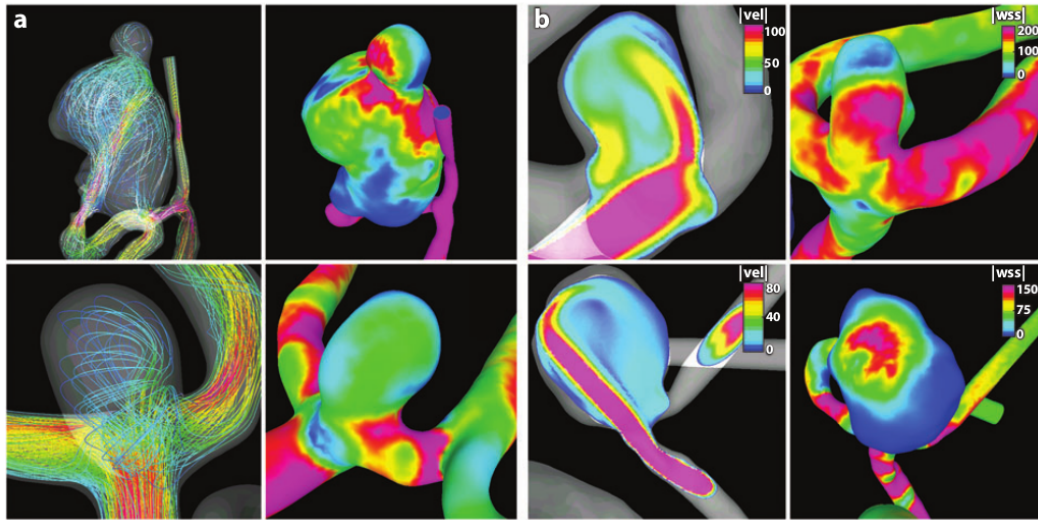


Figure 1.7: (a) Aneurysms with concentrated inflow jet and regions of locally elevated wall shear stress (WSS) (top panels) and with diffuse inflow jet and WSS uniformly lower than the parent artery (bottom panels). (b) Aneurysms with large (top panels) and small (bottom panels) impingement regions compared to the aneurysm size [15].

The high WSS have important effects to the formation of aneurisms [16–18], while the low WSS may lead to the growth and rupture of them [7, 19, 20].

We can obtain such hemodynamic quantities of interest from pure computational fluid dynamics (CFD) simulations. However, very recent studies showed that the elastic motion of the arterial wall has a significant effect on the hemodynamic quantities of interest [9, 10, 21–37].

In [22], Wolters et al. studied on abdominal aortic aneurysm (AAA). In order to facilitate the incorporation of fluid/structure interaction (FSI) in the assessment of AAA wall stress, a method for generating patient-specific hexahedral finite element meshes of the AAA lumen and wall has been presented. The method of mesh generation provides a flexible, semi-automated approach for generating patient-specific hexahedral meshes of the AAA lumen and wall with pre-defined element distributions. The

combined fluid/solid mesh allows for simulations of AAA blood dynamics and AAA wall mechanics and the interaction between the two. And the presented method provides a basis for the development of models for studying the role of blood/wall interaction in processes associated with AAA formation such as wall adaptation and thrombus formation. Results are in Figure 1.8.

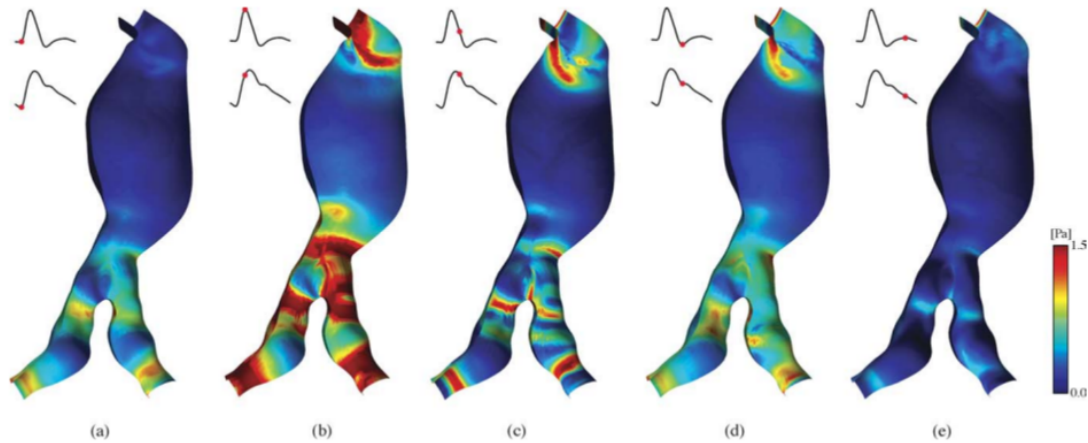


Figure 1.8: Wall shear stress in the deforming geometry at end-diastole (a), peak-systole (b), late-systole (c), end-systole (d), and mid-diastole (e) in the fourth period [22].

In [23], A NURBS (non-uniform rational B-splines)-based isogeometric fluid–structure interaction formulation, coupling incompressible fluids with non-linear elastic solids, and allowing for large structural displacements, is developed by Bazilevs et al. and applied to problems of arterial blood flow modeling and simulation. See Figure 1.9. The approach is compared with representative benchmark problems, yielding very good results. Computation of a patient-specific abdominal aorta is also performed, giving qualitative agreement with computations by other researchers using similar models.

Torii et al. have a lot of studies about FSI. For example in [24], they carried out a computational fluid–structure interaction analysis of the blood flow in arteries with cerebral aneurysm. They have observed that the arterial-wall deformation has a significant influence on the WSS distribution, which is an important factor in creation, growth and rupture of cerebral aneurysm. This influence depends on whether the large displacements and the large WSS occur in the same area. Their simulations illustrate that the arterial geometry plays an important role on that. See Figure 1.10. In [25], they developed a computer modeling technique for cardiovascular hemodynamic simulations.

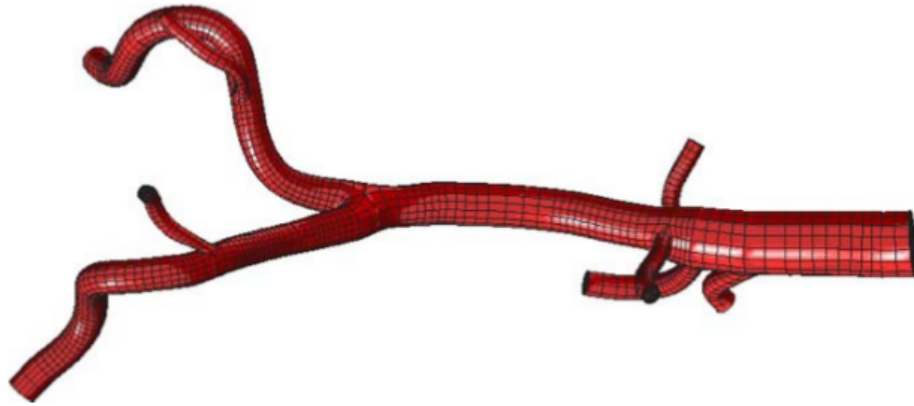


Figure 1.9: Patient-specific abdominal aorta mesh consisting of 52,420 quadratic NURBS elements [23].

With this modeling technique, patient-specific 3D geometry of an artery can be analyzed. They take into account some of the important factors in human body for the purpose of demonstrating in vivo situations in a virtual world. The interaction between the blood flow and the deformation of the arterial walls is a factor that they are specifically focusing on. For such fluid–structure interactions, they have developed a computer modeling tool based on the deforming-spatial-domain/stabilized space–time (DSD/SST) formulation. This simulation tool is applied to a patient-specific model under pulsatile blood flow conditions. The simulations show that the flow behavior with compliant arterial walls is different from what we see with rigid arterial walls in Figure 1.11 and Figure 1.12. Consequently, the distribution of the wall shear stress on the compliant arterial walls is significantly different from that on the rigid arterial walls.

In [26], they applied the technique to a patient-specific arterial model showed the effect of wall deformation on the WSS distribution, Figure 1.13. They compute the interaction between the blood flow and the arterial wall for a patient-specific cerebral aneurysm with various hemodynamic conditions, such as hypertension. They focus on the effects of hypertensive blood pressure on the interaction and the WSS, because hypertension is reported to be a risk factor in rupture of aneurysms. The transient behavior of the blood-flow velocity, and the resulting WSS and the mechanical stress in the aneurysmal

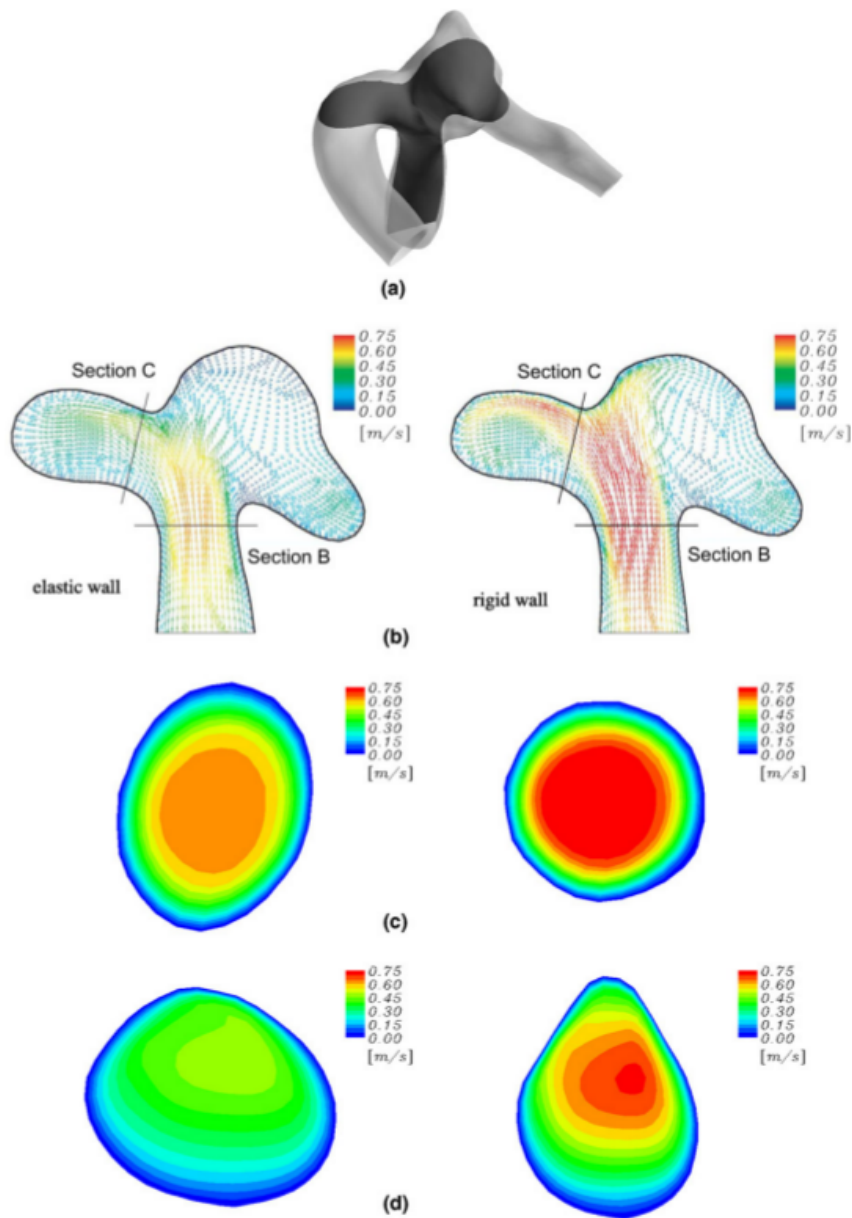


Figure 1.10: Flow velocity in Model 2 (left: elastic wall, right: rigid wall). (a) Cutting plane for Section A. (b) Velocity vectors at Section A. (c) Velocity magnitude at Section B. (d) Velocity magnitude at Section C [24].

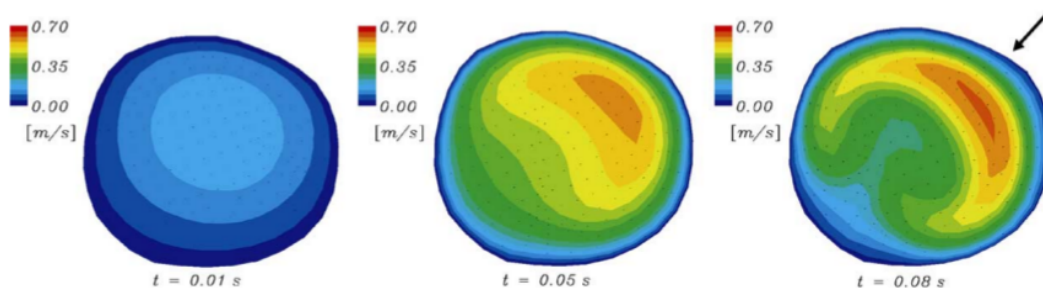


Figure 1.11: Transient behavior of the velocity distribution in Section A for the elastic wall model [25].

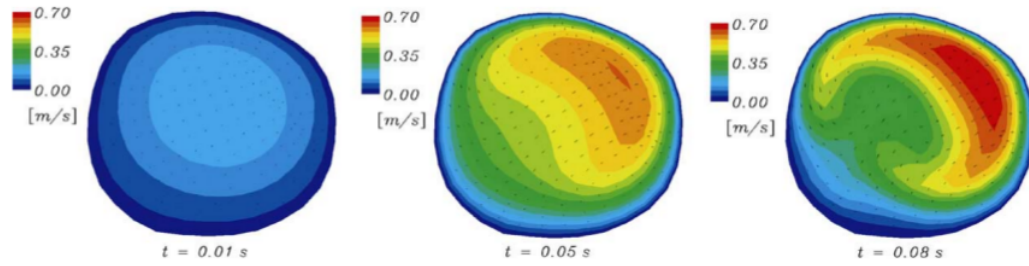


Figure 1.12: Transient behavior of the velocity distribution in Section A for the rigid wall model [25].

wall, are significantly affected by hypertension. The results imply that hypertension affects the growth of an aneurysm and the damage in arterial tissues.

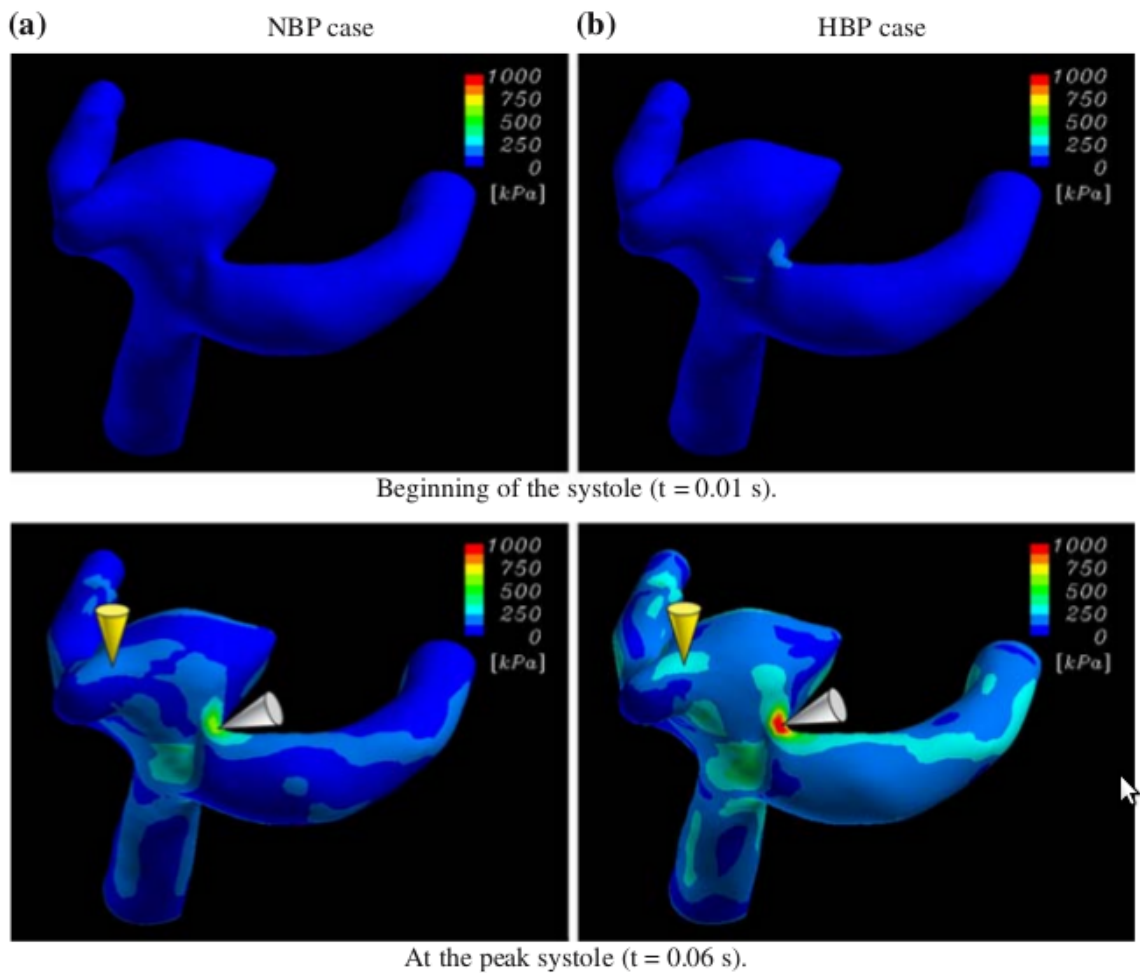


Figure 1.13: Instantaneous principal-stress distributions [26].

In [28], Bazilevs et al. focus on a patient-specific configuration in which the left ventricular assist device (LVAD) is implanted in the descending thoracic aorta.

They perform computations for three pump settings and report our observations for several quantities of hemodynamic interest. They present the first three-dimensional, patient-specific fluid–structure interaction simulation of LVADs.

In [29], fluid–structure interaction (FSI) simulations of a cerebral aneurysm with the linearly elastic and hyper-elastic wall constitutive models are carried out to investigate the influence of the wall-structure model on patient-specific FSI simulations by Torii et al. High flow velocities due to the interaction between the blood flow and aneurysmal wall are seen to be independent of the wall model. The present results indicate that both linearly elastic and hyper-elastic models can be useful to investigate aneurysm FSI.

In [33], a new anisotropic material model of abdominal aortic aneurysm (AAA) was applied to FSI numerical models of patient based AAA geometries for calculating the ensuing stresses developing within the aneurysmal wall in order to develop a more reliable predictor for its risk of rupture by Rissland et al.. Results clearly indicate larger stress values for the anisotropic material and a broader range of stress values, as compared to the isotropic material. While the locations of high and low stresses are consistent between both material models, the differences between the anisotropic and isotropic models become pronounced at large values of strain—a range that becomes critical when the AAA risk of rupture is imminent.

In [34], a fully coupled fluid-structural simulation approach is reviewed, and main aspects of mesh generation in support of patient-specific vascular FSI analyses are presented. Quantities of hemodynamic interest such as wall shear stress and wall tension are studied to examine the relevance of FSI modeling as compared to the rigid arterial wall assumption. They demonstrate the importance of including the flexible wall modeling in vascular blood flow simulations by performing a comparison study that involves four patient-specific models of cerebral aneurysms varying in shape and size.

In [35], a computational vascular fluid–structure interaction framework for the simulation of patient-specific cerebral aneurysm configurations is presented by Bazilevs et al. A new approach for the computation of the blood vessel tissue prestress is also described. Simulations of four patient-specific models are carried out, and quantities of hemodynamic interest such as wall shear stress and wall tension are studied to examine

the relevance of fluid–structure interaction modeling when compared to the rigid arterial wall assumption. The blood flow is governed by the Navier–Stokes equations of incompressible flow posed on a moving domain. The Arbitrary Lagrangian–Eulerian (ALE) formulation is used. They demonstrate that flexible wall modeling plays an important role in accurate prediction of patient-specific hemodynamics. Discussion of the clinical relevance of our methods and results is provided.

The rigid-wall assumption overestimates WSS, precludes pressure wave propagation in blood vessels, and most importantly, disregards stresses in the wall tissue. Wall tissue stress information is critical for the assessment of rupture risk, because rupture occurs when wall stress exceeds its strength [38,39]. As a result, in order to determine accurate criteria for predicting aneurysm formation, growth and rupture, it is important to model vascular flow in conjunction with vessel wall deformation, which leads to coupled fluid–structure interaction (FSI) modeling. The mechanical behavior of blood vessel tissue is well described by means of large-deformation three-dimensional solid or shell modeling [40,41]. Modeling the fluid–structure interaction (FSI) between the blood and the arterial wall is a challenging task. The research in this field is developing fast concerning both modeling aspects and computational efficiency. Taking into account the compliance of the vessels can be achieved by introducing a 3D or 2D elastic structure, using a Lagrangian [42], Eulerian [43] or Arbitrary Lagrangian Eulerian (ALE) formulation [44–46]. Studies of Tezduyar [47,48] and Farhat [49,50] describes the development and applications of ALE methods. In recent years, significant progress has been made in solving blood flow problems in deformable domains using ALE methods [51–54]. More knowledge and theoretical analysis of the ALE method can be found in [55,56]. But considering large models, ALE methods are computationally expensive and not very robust. There are also other formulations that includes the wall deformation based on immersed boundary method [57,58], transpiration techniques based on linearization principles [59,60] or the coupled momentum method [21,61].

As it is seen from other studies, rigid wall assumption gives us wrong results. So implementing fluid-structure interaction is inevitable to obtain realistic results. So here in this study, the rigid wall modeling and the fluid structure modeling will be compared. Like in most of other studies, it will be used Womerley inlet profile. The blood flow will be assumed as non-Newtonian flow based on Carreau model and will be considered

as mild-turbulent flow based on $k-\omega$ SST (shear stress transport) turbulence model. The vessel wall will be modeled as hyperelastic model. The loose-coupling model will be used for the blood flow and vessel wall interaction. Aim of this study is to obtain hemodynamic factors and comparing them in two cases, rigid wall assumption and fluid-structure coupling, and showing that FSI case gives us the more realistic results than the rigid vessel wall assumption.

2. BLOOD FLOW MODELING

2.1 Introduction

Blood flow modeling is an important issue to prevent cardiovascular disease (CVD) as the details has been given in the literature review section. To understand the details of blood flow modeling, blood features, types of flows, boundary conditions, turbulent flow mechanics and modeling techniques has to be well understood.

2.2 Constituents of Human Blood

Blood accounts for 7% of the human body weight, with an average density of approximately 1060 kg/m^3 , very close to pure water's density of 1000 kg/m^3 . The average adult has a blood volume of roughly 5 liters (1.3 gal), which is composed of plasma and several kinds of cells. These blood cells (which are also called corpuscles or "formed elements") consist of erythrocytes (red blood cells, RBCs), leukocytes (white blood cells), and thrombocytes (platelets). By volume, the red blood cells constitute about 45% of whole blood, the plasma about 54.3%, and white cells about 0.7%.

Whole blood (plasma and cells) exhibits non-Newtonian fluid dynamics; its flow properties are adapted to flow effectively through tiny capillary blood vessels with less resistance than plasma by itself. In addition, if all human hemoglobin were free in the plasma rather than being contained in RBCs, the circulatory fluid would be too viscous for the cardiovascular system to function effectively.

Blood is circulated around the body through blood vessels by the pumping action of the heart. In humans, blood is pumped from the strong left ventricle of the heart through arteries to peripheral tissues and returns to the right atrium of the heart through veins. It then enters the right ventricle and is pumped through the pulmonary artery to the lungs and returns to the left atrium through the pulmonary veins. Blood then enters the left ventricle to be circulated again. Arterial blood carries oxygen from inhaled air to all of the cells of the body, and venous blood carries carbon dioxide, a waste product

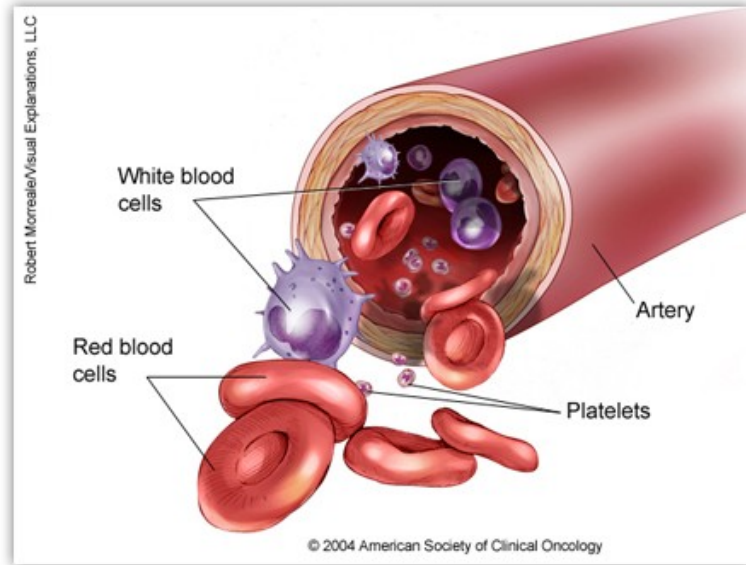


Figure 2.1: Blood features.

of metabolism by cells, to the lungs to be exhaled. However, one exception includes pulmonary arteries, which contain the most deoxygenated blood in the body, while the pulmonary veins contain oxygenated blood.

2.3 Navier-Stokes Equations

In physics, the Navier–Stokes equations describe the motion of fluid substances. These equations arise from applying Newton’s second law to fluid motion, together with the assumption that the stress in the fluid is the sum of a diffusing viscous term (proportional to the gradient of velocity) and a pressure term - hence describing viscous flow.

Following equation is the Navier-Stokes equation tensor notation.

$$\underbrace{\rho \frac{\partial}{\partial t}(u_j)}_{\text{Local rate of change of j-directed momentum}} + \underbrace{\rho u_k \frac{\partial}{\partial x_k}(u_j)}_{\text{Advection of j-directed momentum}} = \underbrace{-\frac{\partial P}{\partial x_j}}_{\text{j-directed pressure gradient force}} + \underbrace{\mu \frac{\partial^2}{\partial x_i \partial x_i}(u_j)}_{\text{j-directed force due to fluid stress (i.e., viscous force)}} + \underbrace{\rho f_j}_{\text{j-directed body force (e.g., gravity)}} \quad (2.1)$$

2.3.1 Velocity field

The Navier–Stokes equations dictate not position but rather velocity. A solution of the Navier–Stokes equations is called a velocity field or flow field, which is a description of the velocity of the fluid at a given point in space and time. Once the velocity field is

solved for, other quantities of interest (such as flow rate or drag force) may be found. This is different from what one normally sees in classical mechanics, where solutions are typically trajectories of position of a particle or deflection of a continuum. Studying velocity instead of position makes more sense for a fluid; however for visualization purposes one can compute various trajectories.

2.3.2 Turbulence

Turbulence is the time-dependent chaotic behavior seen in many fluid flows. It is generally believed that it is due to the inertia of the fluid as a whole: the culmination of time dependent and convective acceleration; hence flows where inertial effects are small tend to be laminar (the Reynolds number quantifies how much the flow is affected by inertia). It is believed, though not known with certainty, that the Navier–Stokes equations describe turbulence properly.

The numerical solution of the Navier–Stokes equations for turbulent flow is extremely difficult, and due to the significantly different mixing-length scales that are involved in turbulent flow, the stable solution of this requires such a fine mesh resolution that the computational time becomes significantly infeasible for calculation (see Direct numerical simulation). Attempts to solve turbulent flow using a laminar solver typically result in a time-unsteady solution, which fails to converge appropriately. To counter this, time-averaged equations such as the Reynolds-averaged Navier–Stokes equations (RANS), supplemented with turbulence models, are used in practical computational fluid dynamics (CFD) applications when modeling turbulent flows. Some models include the Spalart-Allmaras, $k-\omega$ (k-omega), $k-\varepsilon$ (k-epsilon), and SST models which add a variety of additional equations to bring closure to the RANS equations. In this study, mild-turbulent $k-\omega$ SST model is used.

2.3.3 Applicability

Together with supplemental equations (for example, conservation of mass) and well formulated boundary conditions, the Navier–Stokes equations seem to model fluid motion accurately; even turbulent flows seem (on average) to agree with real world observations.

The Navier–Stokes equations assume that the fluid being studied is a continuum (it is infinitely divisible and not composed of particles such as atoms or molecules), and is not moving at relativistic velocities. At very small scales or under extreme conditions, real fluids made out of discrete molecules will produce results different from the continuous fluids modeled by the Navier–Stokes equations.

Another limitation is simply the complicated nature of the equations. Time tested formulations exist for common fluid families, but the application of the Navier–Stokes equations to less common families tends to result in very complicated formulations which are an area of current research. For this reason, these equations are usually written for Newtonian fluids. Studying such fluids is "simple" because the viscosity model ends up being linear; truly general models for the flow of other kinds of fluids (such as blood) do not.

2.3.3.1 Continuity equation

Regardless of the flow assumptions, a statement of the conservation of mass is generally necessary. This is achieved through the mass continuity equation, given in its most general form as:

$$\frac{\partial \rho}{\partial t} + \nabla \cdot (\rho \mathbf{v}) = 0 \quad (2.2)$$

or, using the substantive derivative:

$$\frac{D\rho}{Dt} + \rho(\nabla \cdot \mathbf{v}) = 0 \quad (2.3)$$

2.4 Viscous and Inviscid Flow

Viscous problems are those in which fluid friction has significant effects on fluid motion. The Reynolds number, which is a ratio between inertial and viscous forces, can be used to evaluate whether viscous or inviscid equations are appropriate to problem.

Stokes flow is flow at very low Reynolds numbers, $Re \ll 1$, such that inertial forces can be neglected compared to viscous forces.

On the contrary, high Reynolds numbers indicate that the inertial forces are more significant than the viscous (friction) forces. Therefore, we may assume the flow to be an inviscid flow, an approximation in which we neglect viscosity completely, compared to inertial terms.

This idea can work fairly well when the Reynolds number is high. However, certain problems such as those involving solid boundaries, may require that the viscosity be included. Viscosity often cannot be neglected near solid boundaries because the no-slip condition can generate a thin region of large strain rate (known as Boundary layer) which enhances the effect of even a small amount of viscosity, and thus generating vorticity. Therefore, to calculate net forces on bodies (such as wings) we should use viscous flow equations.

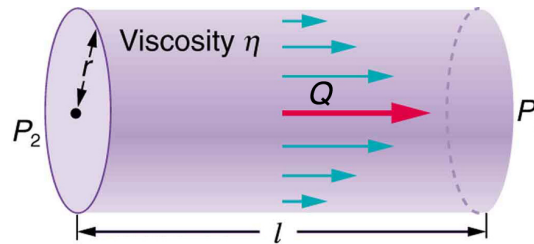


Figure 2.2: Laminar flow of an incompressible fluid of viscosity η through a tube of length l and radius r .

Blood is a viscous flow so, viscous flow conditions will be used in this study. In the Figure 2.3 below shows viscosity curves for two apparently healthy males.

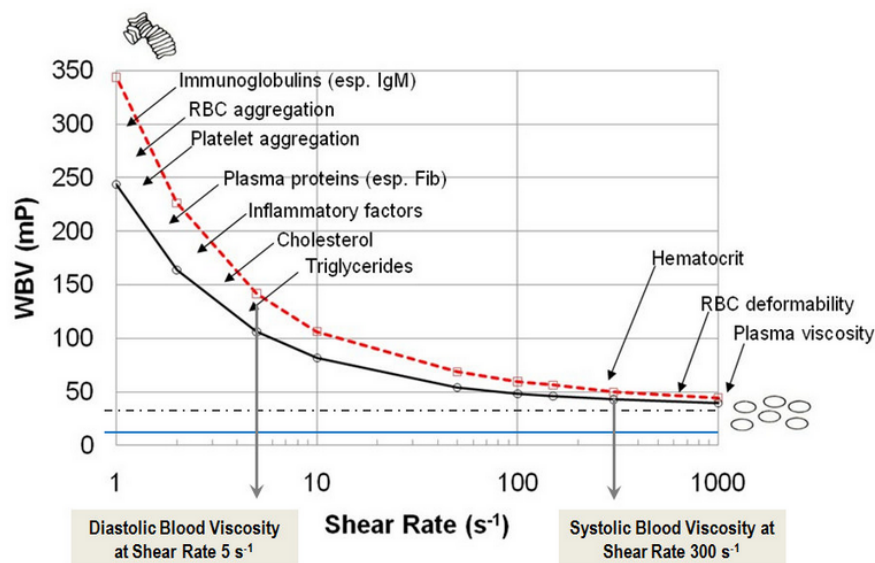


Figure 2.3: Human blood viscosity varies dynamically during each cardiac cycle. At systole, blood is thinner, while at diastole, blood is 2-5 times thicker.

2.5 Laminar and Turbulent Flow

Turbulence is flow characterized by recirculation, eddies, and apparent randomness. Flow in which turbulence is not exhibited is called laminar. It should be noted, however,

that the presence of eddies or recirculation alone does not necessarily indicate turbulent flow—these phenomena may be present in laminar flow as well. Mathematically, turbulent flow is often represented via a Reynolds decomposition, in which the flow is broken down into the sum of an average component and a perturbation component.

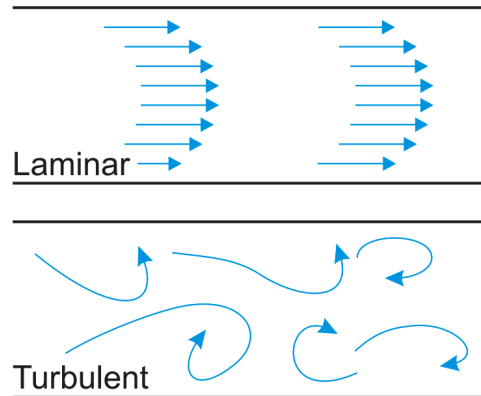


Figure 2.4: Laminar vs. turbulent flow in a pipe.

It is believed that turbulent flows can be described well through the use of the Navier–Stokes equations. Direct numerical simulation (DNS), based on the Navier–Stokes equations, makes it possible to simulate turbulent flows at moderate Reynolds numbers.

When the air flow is smooth and the velocity rises evenly through the boundary layer, the air flow is known as “laminar flow.” Uneven flow through the boundary layer is called “turbulent flow.” Turbulent flow creates a larger boundary area and thus more drag than laminar flow. The boundary layer will tend to have laminar flow initially as the air moves across or down the object.

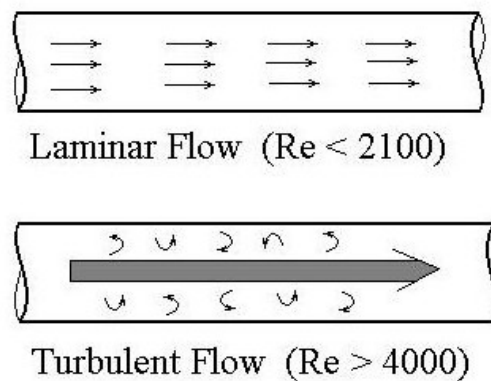


Figure 2.5: Reynolds number for laminar and turbulent flow in a pipe.

Laminar and turbulent flows can be characterized and quantified using Reynolds number. Reynolds number for a flow in a pipe or tube is:

$$\text{Re} = \frac{\rho v D_H}{\mu} = \frac{v D_H}{\nu} = \frac{Q D_H}{\nu A} \quad (2.4)$$

where D_H is the hydraulic diameter of the pipe; its characteristic travelled length, L , (m). Q is the volumetric flow rate (m^3/s). A is the pipe cross-sectional area (m^2). v is the mean velocity of the fluid (SI units: m/s). μ is the dynamic viscosity of the fluid (Pa.s or N. s/ m^2 or kg/(m.s)). ν is the kinematic viscosity ($\nu = \mu / \rho$) (m^2/s). ρ is the density of the fluid (kg/m^3).

When units are considered Re is dimensionless. It should be noted that Reynolds number directly proportional to velocity and inversely proportional to viscosity.

2.5.1 k - ω SST turbulence model

The k - ω SST turbulence model (Menter 1993) is a two-equation eddy-viscosity model which has become very popular. The shear stress transport (SST) formulation combines the best of two worlds. The use of a k - ω formulation in the inner parts of the boundary layer makes the model directly usable all the way down to the wall through the viscous sub-layer, hence the SST k - ω model can be used as a Low-Re turbulence model without any extra damping functions. The SST formulation also switches to a k - ϵ behaviour in the free-stream and thereby avoids the common k - ω problem that the model is too sensitive to the inlet free-stream turbulence properties. Authors who use the SST k - ω model often merit it for its good behaviour in adverse pressure gradients and separating flow. The SST k - ω model does produce a bit too large turbulence levels in regions with large normal strain, like stagnation regions and regions with strong acceleration. This tendency is much less pronounced than with a normal k - ϵ model though.

Kinematic Eddy Viscosity:

$$\nu_T = \frac{a_1 k}{\max(a_1 \omega, SF_2)} \quad (2.5)$$

Turbulence Kinetic Energy:

$$\frac{\partial k}{\partial t} + U_j \frac{\partial k}{\partial x_j} = P_k - \beta^* k \omega + \frac{\partial}{\partial x_j} \left[(v + \sigma_k v_T) \frac{\partial k}{\partial x_j} \right] \quad (2.6)$$

Specific Dissipation Rate:

$$\frac{\partial \omega}{\partial t} + U_j \frac{\partial \omega}{\partial x_j} = \alpha S^2 - \beta \omega^2 + \frac{\partial}{\partial x_j} \left[(v + \sigma_\omega v_T) \frac{\partial \omega}{\partial x_j} \right] + 2(1 - F_1) \sigma_{\omega 2} \frac{1}{\omega} \frac{\partial k}{\partial x_i} \frac{\partial \omega}{\partial x_i} \quad (2.7)$$

Closure Coefficients and Auxilary Relations:

$$\begin{aligned} F_2 &= \tanh \left[\left[\max \left(\frac{2\sqrt{k}}{\beta^* \omega y}, \frac{500v}{y^2 \omega} \right) \right]^2 \right] \\ P_k &= \min \left(\tau_{ij} \frac{\partial U_i}{\partial x_j}, 10\beta^* k \omega \right) \\ F_1 &= \tanh \left\{ \left\{ \min \left[\max \left(\frac{\sqrt{k}}{\beta^* \omega y}, \frac{500v}{y^2 \omega} \right), \frac{4\sigma_{\omega 2} k}{CD_{k\omega} y^2} \right] \right\}^4 \right\} \\ CD_{k\omega} &= \max \left(2\rho \sigma_{\omega 2} \frac{1}{\omega} \frac{\partial k}{\partial x_i} \frac{\partial \omega}{\partial x_i}, 10^{-10} \right) \\ \phi &= \phi_1 F_1 + \phi_2 (1 - F_1) \\ \alpha_1 &= \frac{5}{9}, \alpha_2 = 0.44 \\ \beta_1 &= \frac{3}{40}, \beta_2 = 0.0828 \\ \beta^* &= \frac{9}{100} \\ \sigma_{k1} &= 0.85, \sigma_{k2} = 1 \\ \sigma_{\omega 1} &= 0.5, \sigma_{\omega 2} = 0.856 \end{aligned} \quad (2.8)$$

2.6 Newtonian and Non-Newtonian Fluids

A non-Newtonian fluid is a fluid whose flow properties differ in any way from those of Newtonian fluids. Most commonly the viscosity (the measure of a fluid's ability to resist gradual deformation by shear or tensile stresses) of non-Newtonian fluids is dependent on shear rate or shear rate history. Some non-Newtonian fluids with shear-independent viscosity, however, still exhibit normal stress-differences or other non-Newtonian behavior. Many salt solutions and molten polymers are non-Newtonian

fluids, as are many commonly found substances such as ketchup, custard, toothpaste, starch suspensions, paint, blood, and shampoo. In a Newtonian fluid, the relation between the shear stress and the shear rate is linear, passing through the origin, the constant of proportionality being the coefficient of viscosity. In a non-Newtonian fluid, the relation between the shear stress and the shear rate is different and can even be time-dependent. Therefore, a constant coefficient of viscosity cannot be defined.

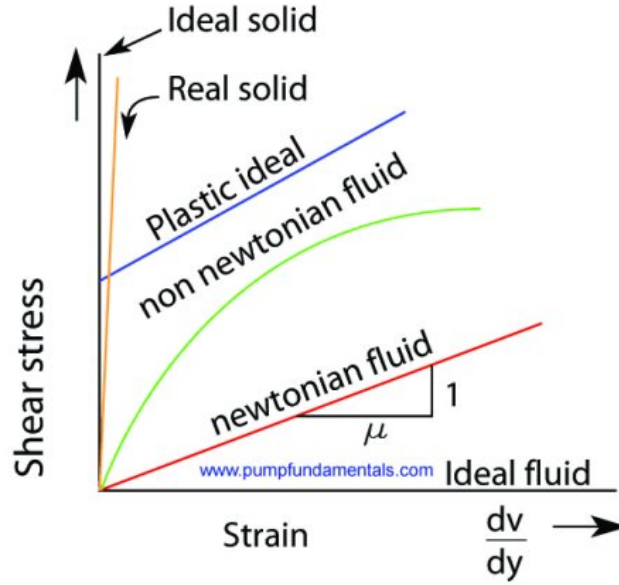


Figure 2.6: Shear/strain relationship for a Newtonian fluid.

In this thesis, blood flow will be modeled as non-Newtonian fluid. Blood density will be taken as 1060 kg/m^3 and non-Newtonian dynamic viscosity will be denoted by the Carreau model.

2.6.1 Non-Newtonian Carreau model

The Carreau model attempts to describe a wide range of fluids by the establishment of a curve-fit to piece together functions for both Newtonian and shear-thinning ($n < 1$) non-Newtonian laws. Viscosity, μ_{eff} , depends upon the shear rate, $\dot{\gamma}$, by the following equation:

The Carreau blood model constitutive law and its parameters will be as following:

$$\mu_{\text{eff}}(\dot{\gamma}) = \mu_{\text{inf}} + (\mu_0 - \mu_{\text{inf}}) \left(1 + (\lambda \dot{\gamma})^2 \right)^{\frac{n-1}{2}} \quad (2.9)$$

where μ_0 , μ_{inf} , λ and n are material coefficients that:

μ_0 = viscosity at zero shear rate (Pa.s)

μ_{inf} = viscosity at infinite shear rate (Pa.s)

λ = relaxation time (s)

n = power index

Bird Carreau model parameters that used in this study are in the table:

Table 2.1: Bird-Carreau model constitutive law parameters

μ_0	3.03E-02
μ_{inf}	3.67E-03
Power law index n	3.37E-01
λ	9.73E-01

Following figure shows the variation of viscosity with shear rate according to the Carreau model.

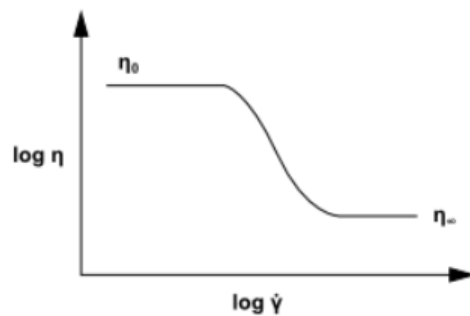


Figure 2.7: Variation of viscosity with shear rate according to the Carreau model.

More detailed studies about non-Newtonian and Newtonian blood viscosity models are in [62].

3. VESSEL WALL

3.1 Introduction

One of the most important components of the circulatory system is the blood vessels. In order to better understand how the vessels within the circulatory system work, we must understand the basic structure of the vessels.

There are three major types of blood vessels found in the body; arteries, veins and capillaries. Arteries are thicker, containing muscular and elastic tissue making the vessel strong and resilient, capable of withstanding the high blood pressure that accompanies the bursts of blood released from the heart into the arteries. Arteries are efferent vessels, meaning they are responsible for carrying blood away from the heart. Veins are much more flaccid, containing less muscular and elastic tissue and are capable of expanding greatly to accommodate increased blood pressure and flow. Lastly, capillaries are much smaller vessels which serve as the site for transfer of nutrients, hormones and substances between the tissues and bloodstream.

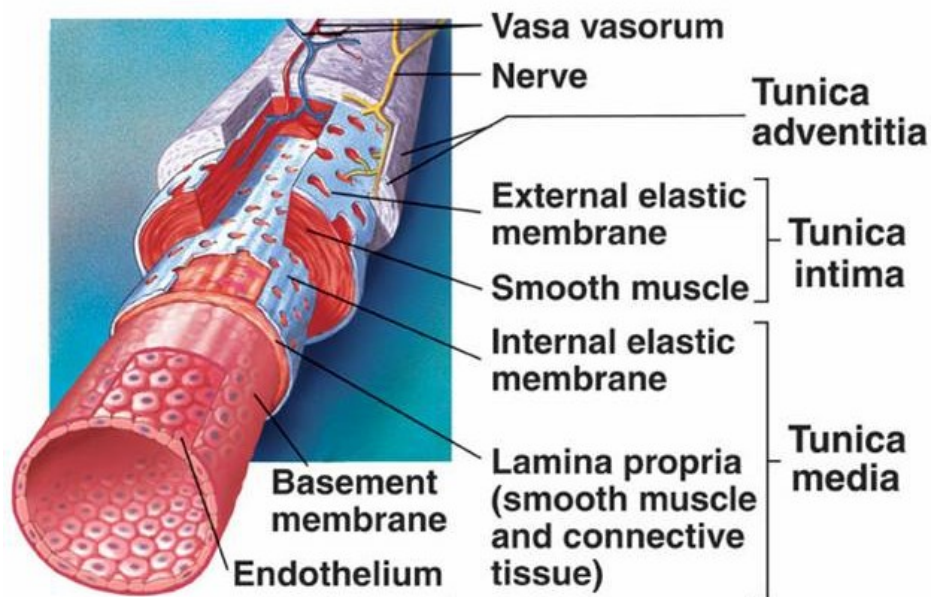


Figure 3.1: Structure of blood vessels walls.

Arteries and veins are similar to one another in the composition of their walls. Arteries and veins both contain three layers known as tunics. By thinking of these tunics as layers of clothing (much like the type of "tunic" most are familiar with) these three layers are easier to remember.

The first layer of the vessel wall is known as the tunica interna. This layer is sometimes referred to as the tunica intima. The tunica interna is the innermost of the tunics, forming the circular space through which blood flows. The tunica interna is composed of simple squamous epithelium known as the endothelium. The endothelium acts as a semi-permeable membrane allowing the passage and retention of certain substances. The endothelium found within the tunica interna is also responsible for the secretion of hormones that directly control and influence vasomotion; the dilation and constriction of the vessels. Additionally, the endothelium is also capable of repelling the blood cells and other substances within the blood due to the flat, slick nature of the cells it is composed of. This repulsion allows the blood to flow freely through the vessels without sticking to the sides of the vessel walls or forming clots. If the endothelium is damaged, however, the blood will respond, forming a clot and sending immune cells to the damaged site.

The second layer of a blood vessel is known as the tunica media. The tunica media is the thickest of the three layers and is composed of smooth muscle, collagen, and in certain vessels, elastic tissue. The tunica media is a strengthening layer, providing a vessel with the ability to withstand the force of increased blood pressure, thus preventing vessels from rupturing when blood volume or pressure increases. Additionally, the muscles found within the tunica media is responsible for carrying out vasomotion, signalled by the hormones secreted by the endothelium of the tunica interna.

The final layer of the vessel walls is known as the tunica externa, the most external layer of the vessel walls. The tunica externa is sometimes referred to as the tunica adventitia. The tunica externa is composed of loose connective tissue, responsible for strengthening and reinforcing the vessel even further. The tunica externa often converges with neighboring vessels, organs and tissues. The tunica externa is also responsible for securing the placement of the vessel within the body among neighboring tissues and structures.

Capillary walls differ from the walls of arteries and veins, as capillary walls are only one endothelial cell thick, allowing for the passage of substances through this wall. This especially thin wall makes the capillaries much more fragile and susceptible to injury, however, the thin nature of the capillaries is necessary for the transfer of substances between the bloodstream and surrounding tissues.

3.2 Governing Equations

Solids and fluids are both continua, whose behaviour can be described by the same continuity and momentum equations. There are no simplifying assumptions in the momentum and continuity equations for fluids and solids and both are treated as compressible. Only the constitutive laws are different. Therefore, this will be presented separately. Details can be found in most continuum mechanics text books, such as Malvern (1969) and Segel (1977). The constitutive law for vessel wall presented here assumes an incompressible hyperelastic material by using Fung's material parameters.

3.2.1 Constitutive equations for hyperelastic material

In physics and engineering, a constitutive equation is a relation between two physical quantities (especially kinetic quantities as related to kinematic quantities) that is specific to a material or substance, and approximates the response of that material to external stimuli, usually as applied fields or forces. They are combined with other equations governing physical laws to solve physical problems; for example in fluid mechanics the flow of a fluid in a pipe, in solid state physics the response of a crystal to an electric field, or in structural analysis, the connection between applied stresses or forces to strains or deformations. Constitutive relations are modified to account for the rate of response of materials and their non-linear behavior. The first constitutive equation (constitutive law) was developed by Robert Hooke and is known as Hooke's law. It deals with the case of linear elastic materials. In its simplest form, the law defines the spring constant constant (or elasticity constant) k in a scalar equation, stating the tensile/compressive force is proportional to the extended (or contracted) displacement x :

$$F_i = -kx_i \tag{3.1}$$

meaning the material responds linearly. Equivalently, in terms of the stress σ , Young's modulus E , and strain ε (dimensionless):

$$\sigma = E \varepsilon \quad (3.2)$$

In general, forces which deform solids can be normal to a surface of the material (normal forces), or tangential (shear forces), this can be described mathematically using the stress tensor:

$$\sigma_{ij} = C_{ijkl} \varepsilon_{kl} \Leftrightarrow \varepsilon_{ij} = S_{ijkl} \sigma_{kl} \quad (3.3)$$

where C is the elasticity tensor and S is the compliance tensor.

One solid-state deformation in elastic material is, hyperelastic deformation. A hyperelastic material is a type of constitutive model for ideally elastic material for which the stress-strain relationship derives from a strain energy density function. The hyperelastic material is a special case of a Cauchy elastic material. Hyperelasticity provides a means of modeling the stress-strain behavior of materials. Ronald Rivlin and Melvin Mooney developed the first hyperelastic models, the Neo-Hookean and Mooney–Rivlin solids. Many other hyperelastic models have since been developed. Other widely used hyperelastic material models include the Ogden model and the Arruda–Boyce model. The Fung's material will be used in this study as hyperelastic material.

3.2.1.1 Fung-elastic material

Fung developed a constitutive equation for preconditioned soft tissues which is

$$W = \frac{1}{2} \left[q + c \left(e^Q - 1 \right) \right] \quad (3.4)$$

with

$$q = a_{ijkl} E_{ij} E_{kl} \quad Q = b_{ijkl} E_{ij} E_{kl} \quad (3.5)$$

quadratic forms of Green-Lagrange strains E_{ij} and a_{ijkl} , b_{ijkl} and c material constants.

ω is the strain energy function per volume unit, which is the mechanical strain energy for a given temperature.

The Fung-model, simplified with isotropic hypothesis (same mechanical properties in all directions) is written as follows. This form of equation is written in respect of the principal stretches (λ_i):

$$W = \frac{1}{2} \left[a(\lambda_1^2 + \lambda_2^2 + \lambda_3^2 - 3) + b \left(e^{c(\lambda_1^2 + \lambda_2^2 + \lambda_3^2 - 3)} - 1 \right) \right], \quad (3.6)$$

where a , b and c are constants.

An experiment is conducted by [63] M. S. Celebi to obtain material coefficients of a soft tissue using Inverse Finite Element Method.

4. FLUID-STRUCTURE COUPLING MODELS

4.1 Introduction

Fluid–structure interaction (FSI) is the interaction of some movable or deformable structure with an internal or surrounding fluid flow. Fluid–structure interactions can be stable or oscillatory. In oscillatory interactions, the strain induced in the solid structure causes it to move such that the source of strain is reduced, and the structure returns to its former state only for the process to repeat. There are two major FSI coupling in the literature, these are called monolithic and partitioned.

4.2 Monolithic

In monolithic coupling also called strongly-coupled, governing equations for both fluid and structure subdomains are cast in terms of the same primitive variables. In other words, a new governing equations are derived by using both fluid equations and structure equations which would then be applied on the same level of discretized mesh interface. Consequently, the equations of fluid, structure and mesh moving are solved simultaneously at the same time step. In order to accomplish that Arbitrary Lagrangian-Eulerian (ALE) formulation can be used. To use ALE formulation in a FSI problem, advanced mesh update techniques must be deployed in order to adapt changing boundaries of the domains as well as depending on the discretization parameters, special predictor-multicorrector algorithms and interface projection techniques for non-matching fluid and structure interface discretizations must also be implemented. For further information about ALE and its FSI techniques, see (Bazilevs, Takizawa, & Tezduyar, 2013e), (Bazilevs, Takizawa, & Tezduyar, 2013c) and (Bazilevs, Takizawa, & Tezduyar, 2013b).

Due to fully-coupled fashion, the strongly-coupled solvers are more robust than partitioned-coupled solvers. However, strongly-coupled solver must be designed from scratch by virtually precluding fluid and structure solvers. There are three categories

of coupling techniques in strongly-coupled FSI methods which are block-iterative, quasi-direct and direct-coupling. In all three coupling techniques, iterations are performed within a time-step to simultaneously converge the solutions of all the equations involved. For further informations about the techniques, see (Bazilevs, Takizawa, & Tezduyar, 2013a)

4.3 Partitioned

In partitioned coupling, both fluid and structure domains are modeled and discretized separately. On the fluid part, traditional CFD techniques are used for the flow properties. On the structure part, finite element on structural mechanics are applied. Therefore, existent fluid solvers and structure solvers can be used which make this approach very flexible and desirable. However, stress and displacement terms must be transferred across the domain interface. Moreover, this coupling between fluid solver and structure solver must produce accurate results without deteriorating the convergence of the system too much. Meeting with those criteria are the hardest part of partitioned coupling in FSI. There are two main techniques under partitioned-coupling: loose-coupling and tight-coupling.

4.3.1 Loose-coupling

In loose-coupling, the equations of fluid mechanics, structural mechanics and mesh moving are solved sequentially as in Figure 4.1.

As can be seen from the Figure 4.1,

- Dynamic mesh solver updates the mesh according to the displacement at the structure part and velocity at the interface is extrapolated from the rate of displacement.
- Fluid mechanics equations are solved by using that received values from the extrapolation.
- Structural mechanics equations with the updated fluid mechanics interface traction are solved.
- By using the new displacements from structure solver, mesh moving algorithm updates the meshes.

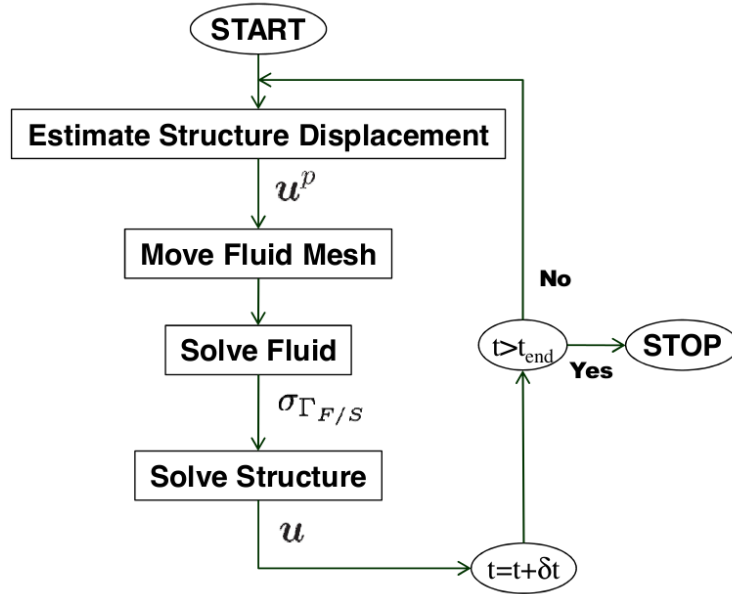


Figure 4.1: Loose-Coupling solver sequence.

Although this solver looks very promising, there is a significant stability issue that must be handled carefully. The origin of the problem is if the following equality holds or not?

$$u^p = u \quad (4.1)$$

In other words, the new fluid forces are calculated by using the predicted(extrapolated) displacements instead of the actual displacements due to the mesh update at the end of the solver. Consequently, an artificial added mass problem is encountered during the solutions. Inaccuracy of the extrapolation approximation of the displacements, fluid flow solver encounters with an added mass input to the system which in turn affects the convergence significantly. Moreover, decreasing time step does not improve the stability derived from the added mass. According to the previous works, when

$$\frac{\text{fluid density}}{\text{solid density}} \geq 1 \quad (4.2)$$

significant instabilities on the solution were observed.

4.3.2 Tight-coupling

In tight-coupling, an outer fixed-point iteration is used in order to ensure the convergence at every given time-step. In order to accomplish this, well-known Aitken Method which

is an under-relaxation factor injected into the fixed-point iteration as can be seen from the Figure 3 is used. By using an under-relaxation multiplier the effects of the extrapolation is minimized so that the stability and the rate of convergence are improved. The algorithm of the tightly-coupled solver can be described as:

- Solve the mesh equation
- Transfer interface velocity to fluid solver
- Solve the flow equations
- Transfer interface pressures into structure solver
- Solve the structure equations
- Restrict new interface deformations by using under-relaxation
- Check the residuals between the last time step and the new one

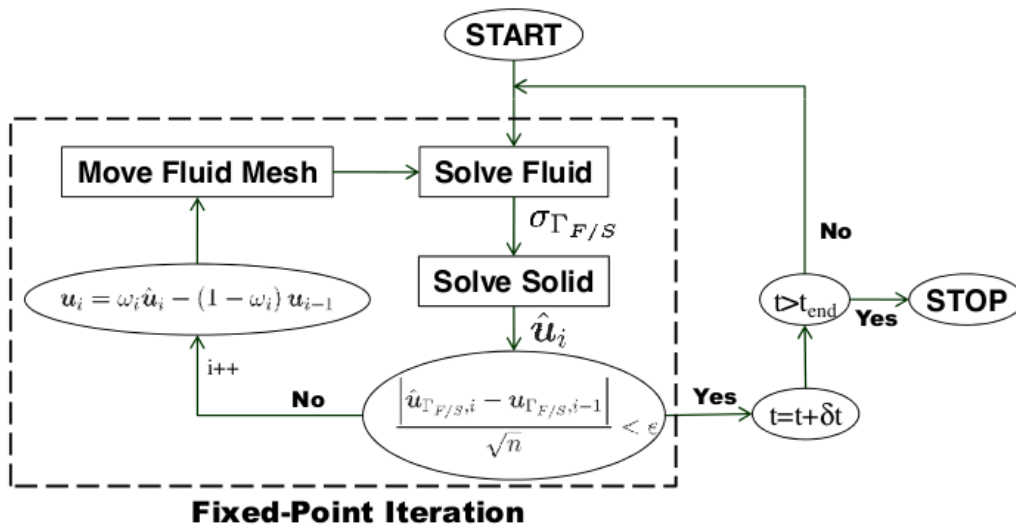


Figure 4.2: Tight-Coupling solver sequence with fixed point iteration with under-relaxation.

5. NUMERICAL SIMULATIONS AND RESULTS

5.1 Introduction

In this section, a cylindrical pipe without stenosis, artificially generated stenosed coronary artery and bypassed artery are constructed. Uniform and Womersley incoming flows are used for Newtonian, non-Newtonian and turbulent flows.

5.2 Pre-processing for Simulations

Pre-processing is very important part of the blood flow simulation process. Because if geometry and mesh does not constructed good enough, the results will be wrong and even flow won't move inside of the geometry. For obtaining good and converged results, mesh have to be constructed good, solver settings have to be set properly, boundary conditions have to be physical and the models that we select to solve the problem has to be the right one.

Firs of all geometry and mesh will be constructed. Our first case is cylindrical pipe without stenosis, second case is cylindrical pipe with stenosis and third case is cylindrical stenosed pipe with bypass. For all cases, we will compare the results for newtonian and non-newtonian models. Also for velocity profile, the constant inlet value and Womersley velocity profile are used and compared.

All geometries are constructed in OpenFOAM software, and then meshed with blockMesh utility inside of the software.

IcoFoam solver is used for Newtonian flow model, nonNewtonianIcoFoam solver is used for non-Newtonian flow model, simpleFoam solver is used for turbulent flow model and finally icoFsiFoam is used for fluid-structure interaction model.

The geometry and mesh for the fluid part of cylindrical pipe without stenosis is in Figure 5.1 and 5.2. Figure 5.3 shows the mesh of solid part for fluid structure interaction model.

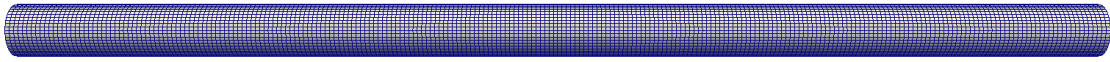


Figure 5.1: Cylindrical pipe without stenosis.

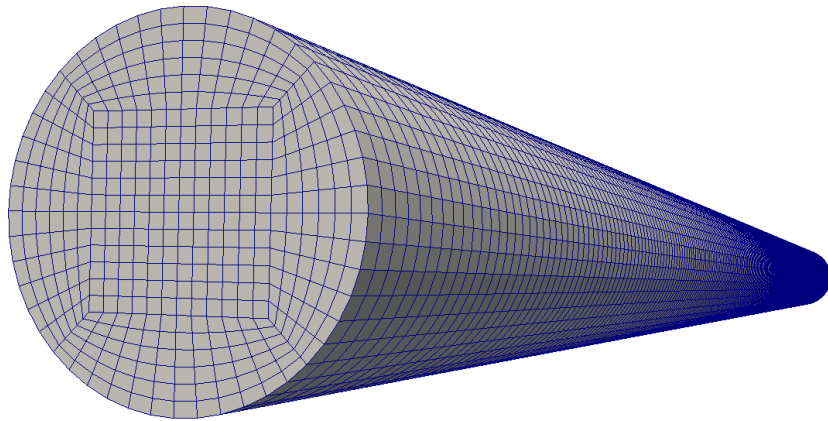


Figure 5.2: Inlet of the cylindrical pipe.

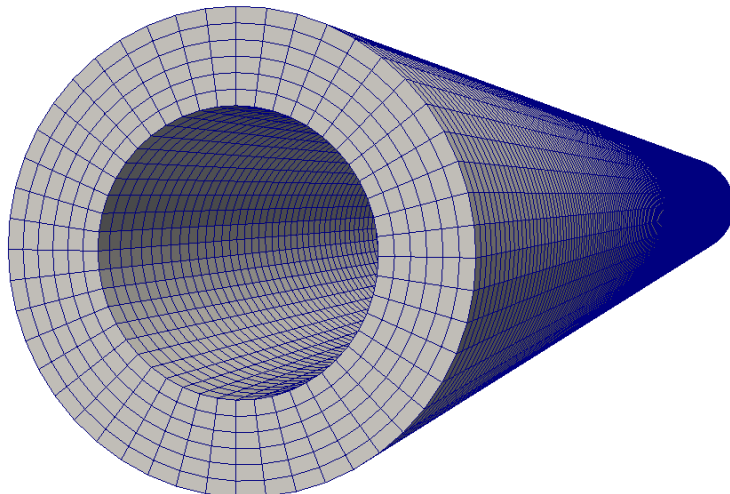


Figure 5.3: Mesh of solid part for FSI.

The geometry of stenosed pipe is in Figure 5.4.

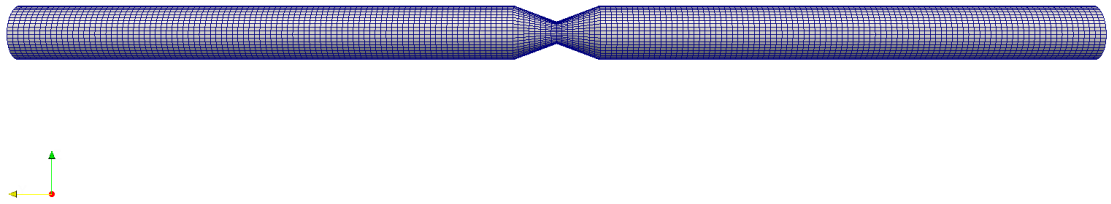


Figure 5.4: Stenosed pipe.

The mesh of stenosed pipe is in Figure 5.5.

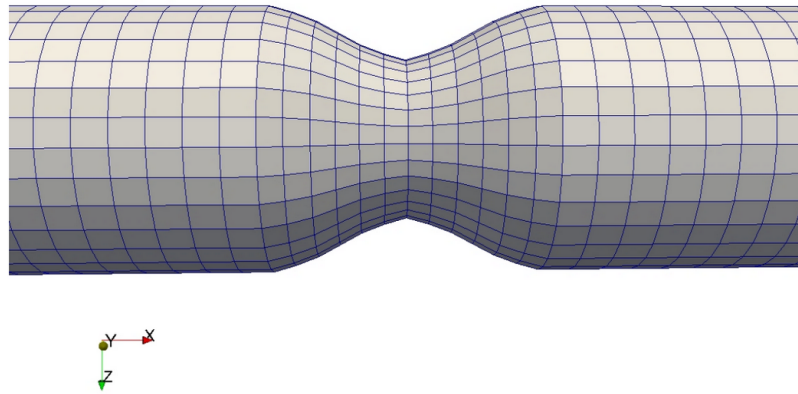


Figure 5.5: Grid for the stenosis region.

The details of the geometry and mesh of stenosed pipe with and without bypass are presented in Figure 5.4, 5.5, 5.6, 5.7. and 5.8.

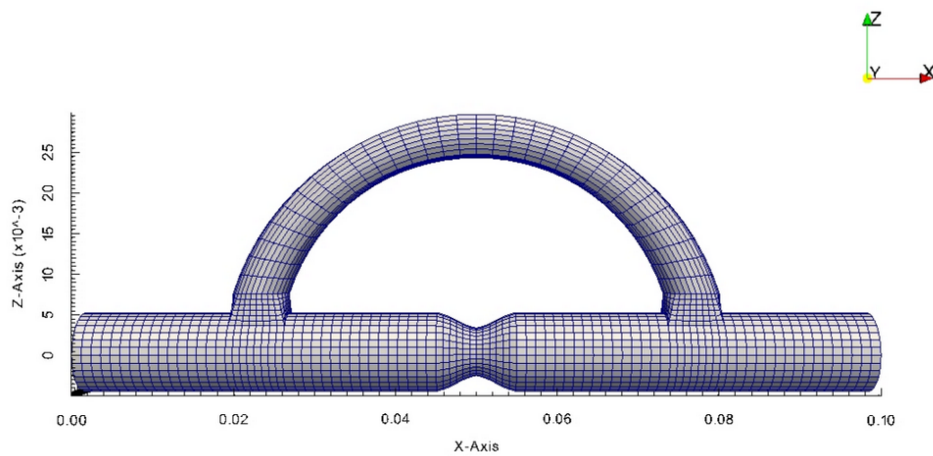


Figure 5.6: Numerical grid used for the stenosed bypass simulation.

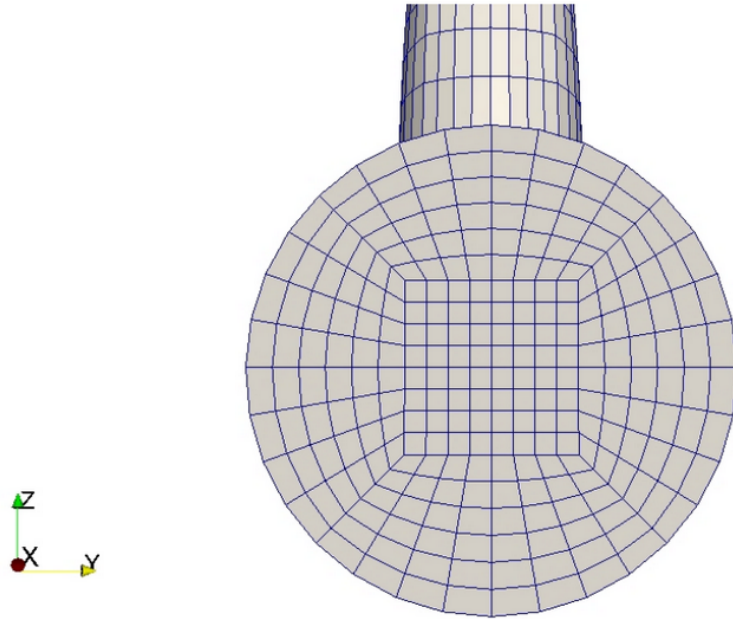


Figure 5.7: Inlet of the stenosed pipe with bypass.

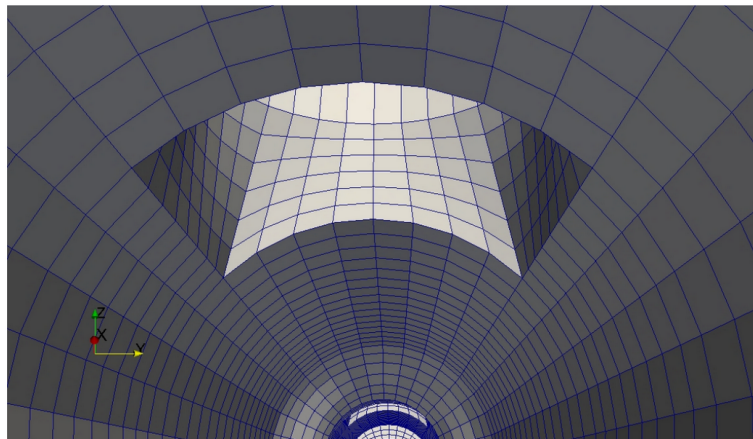


Figure 5.8: Intersection region as seen from the inside of the broad branch.

As it's seen from the figures, hexahedral meshes are used and icoFOAM solver is used for solving the case.

5.3 Test Cases

5.3.1 Fixed model

5.3.1.1 Flow in cylindrical pipe without stenosis

In this case, first of all, constant inlet value = 1 m/s and Womersley velocity profile are compared. After that Womersley velocity profile is used for all simulations,

because it gives more realistic results. Secondly, blood flow is assumed Newtonian and non-Newtonian. Results are compared for both cases.

Figure 5.9 shows the velocity and Figure 5.10 show the pressure on the pipe.

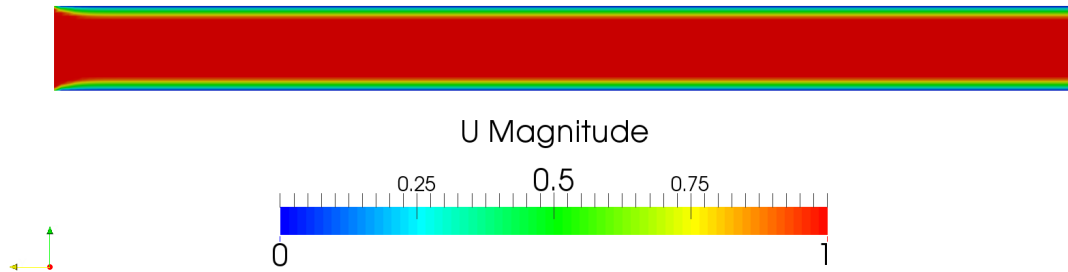


Figure 5.9: Velocity in cylindrical pipe without stenosis.

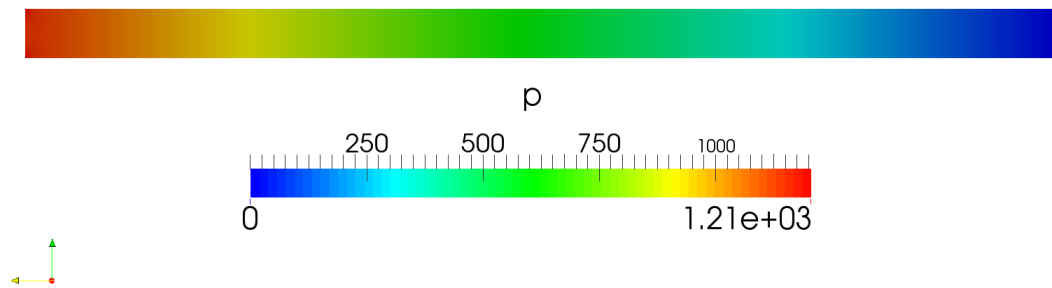


Figure 5.10: Pressure in cylindrical pipe without stenosis.

Figure 5.11 shows the residuals of the flow for constant inlet velocity 1 m/s. It can be concluded that flow velocities are computed with an acceptable accuracy and converged to an exact value.

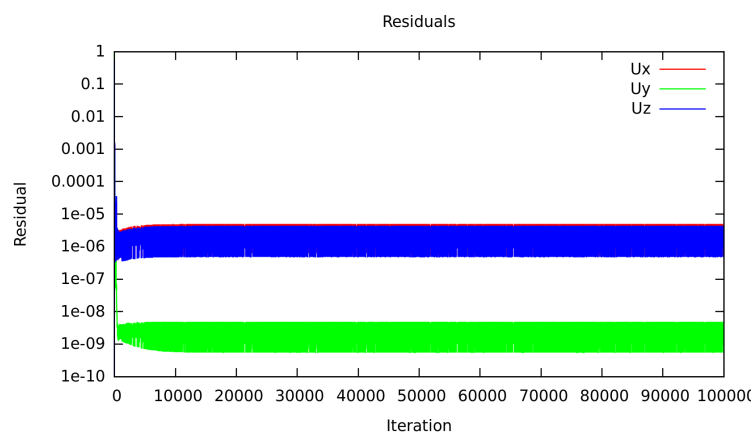


Figure 5.11: Residuals of the flow.

When we change the constant inlet velocity value to Womersley velocity profile, we get more realistic results. Womersley velocity profile is shown in Figure 5.12 and Figure 5.13 shows the residuals of the flow.

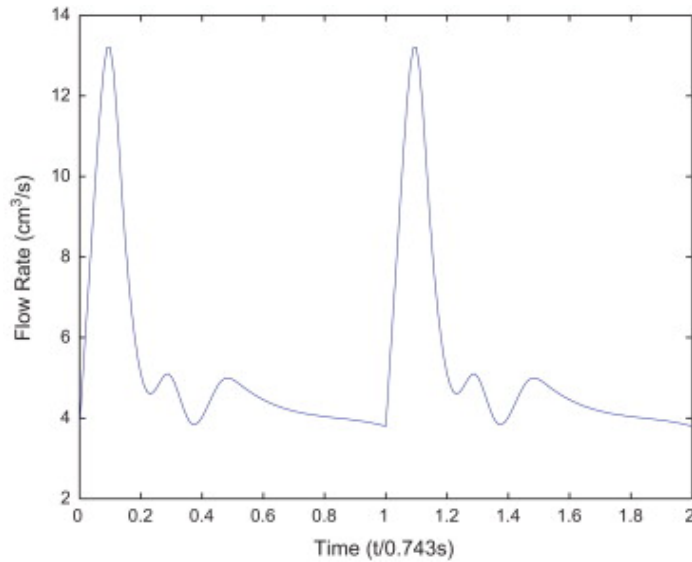


Figure 5.12: Womersley velocity inlet profile.

Figure 5.12 is the physiological flow rate in the artery for two cardiac cycles. The unit of flow rate is cm^3/s and the time is dimensionless (dividing real time by one cardiac cycle period, $T = 0.743s$). (Senol Piskin, M. Serdar Celebi, 2013. [64])

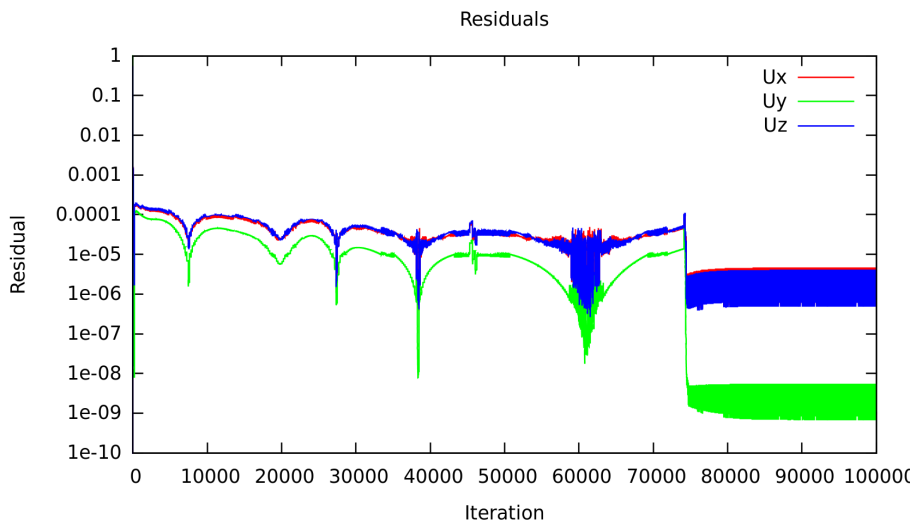


Figure 5.13: Residuals of the flow.

When we take a slice in the middle of the cylinder, we can see the difference between the constant inlet value and womersley velocity profile. Figure 5.14 and 5.15 show the differences between velocities.

When we compare Figure 5.14 and Figure 5.15, we understand that first one is undeveloped flow and the second one is developed flow. Blood flow is developed flow, so Womersley velocity profile will give more realistic results for our problem. Because of that, Womersley velocity profile will be used for all simulations.

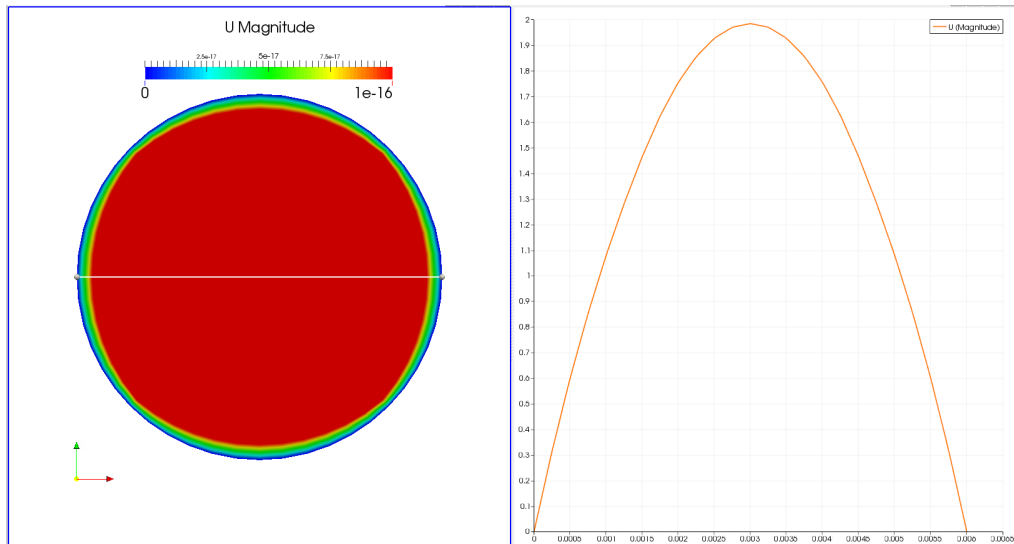


Figure 5.14: Velocity profile for constant value inlet.

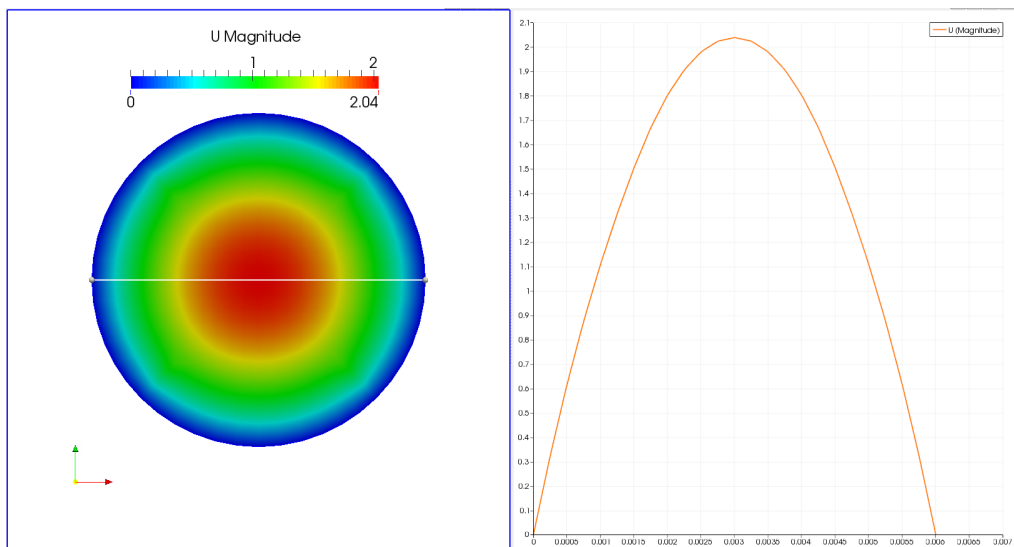


Figure 5.15: Velocity profile for womersley inlet profile.

Now, the difference between Newtonian, non-Newtonian and turbulent flow will be compared for the flow in cylindrical pipe without stenosis. A slice will be taken in the middle of the cylinder as in Figure 5.16. Then for a point that we choose on the top of the slice like in Figure 5.17, the pressure and wall shear stress distribution will be compared for Newtonian, non-Newtonian and turbulence models. Because of this point is on the wall and on the wall, velocity value is zero because of the no-slip boundary condition, the velocity profile can not be compared at this point. So velocity distribution results will be compared for Newtonian, non-Newtonian and turbulence models at a point that is chosen at the center of this slice.

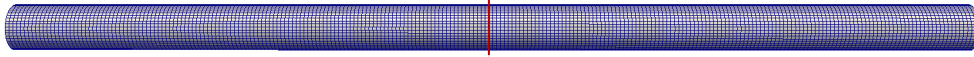


Figure 5.16: Taking a point at the center of the slice that took in the middle of the vessel.

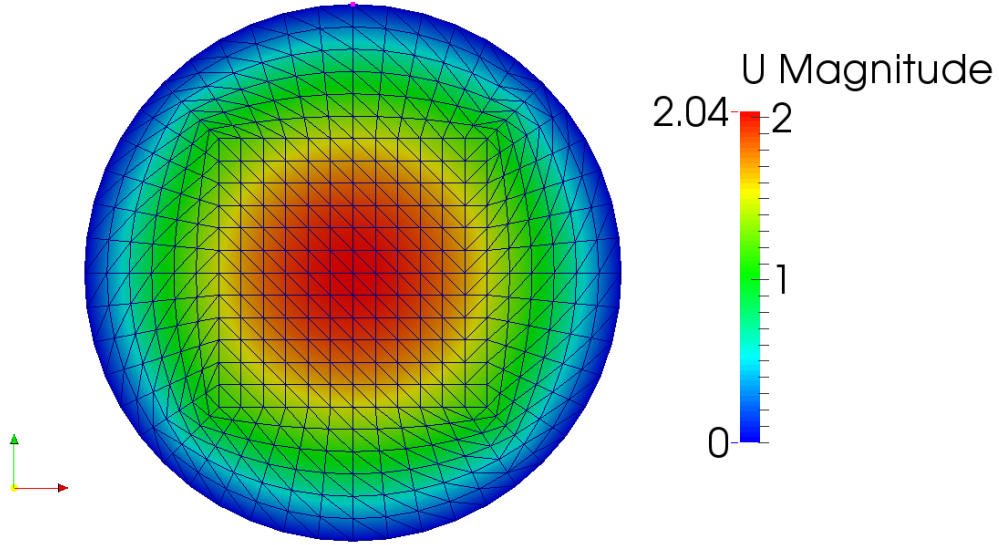


Figure 5.17: The point on the top of the slice (pink one).

For non-Newtonian flow, blood density will be taken as 1060 kg/m^3 and non-Newtonian dynamic viscosity will be denoted by the Carreau model. The Carreau blood model constitutive law and its parameters will be as following:

$$\mu_{eff}(\gamma) = \mu_{inf} + (\mu_0 - \mu_{inf})(1 + (\lambda \dot{\gamma})^2)^{\frac{n-1}{2}} \quad (5.1)$$

Table 5.1: Bird-Carreau model parameters.

μ_0	3.03E-02
μ_{inf}	3.67E-03
Power law index n	3.37E-01
λ	9.73E-01

Figure 5.18, Figure 5.19 and Figure 5.20 show the difference between wall shear stress, pressure and velocity of Newtonian, non-Newtonian and turbulent flow models.

Results show that, there is a good agreement in velocity and shear stress distributions. But, on the other hand, there is an important difference (% 200-250) in pressure distributions between Newtonian and non-Newtonian models.

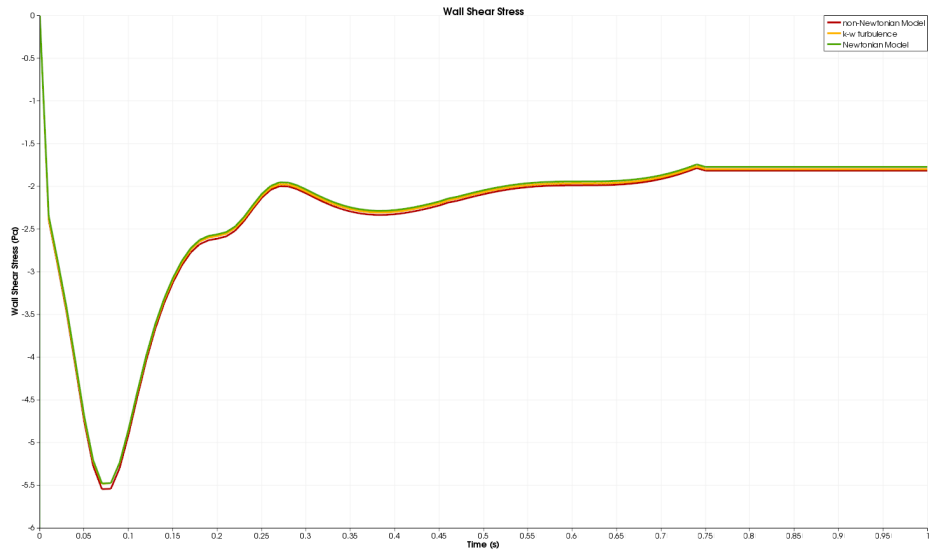


Figure 5.18: Comparison of wall shear stress distribution.

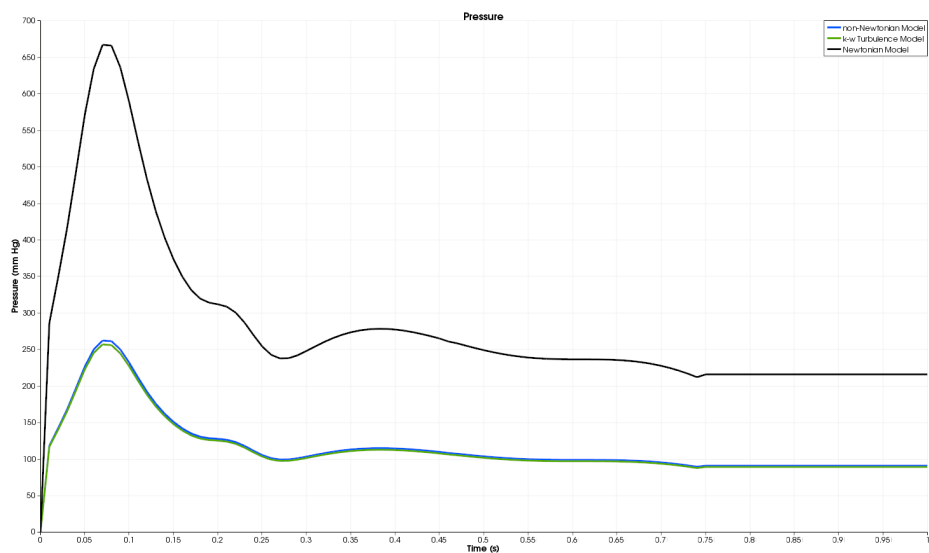


Figure 5.19: Comparison of pressure distribution.

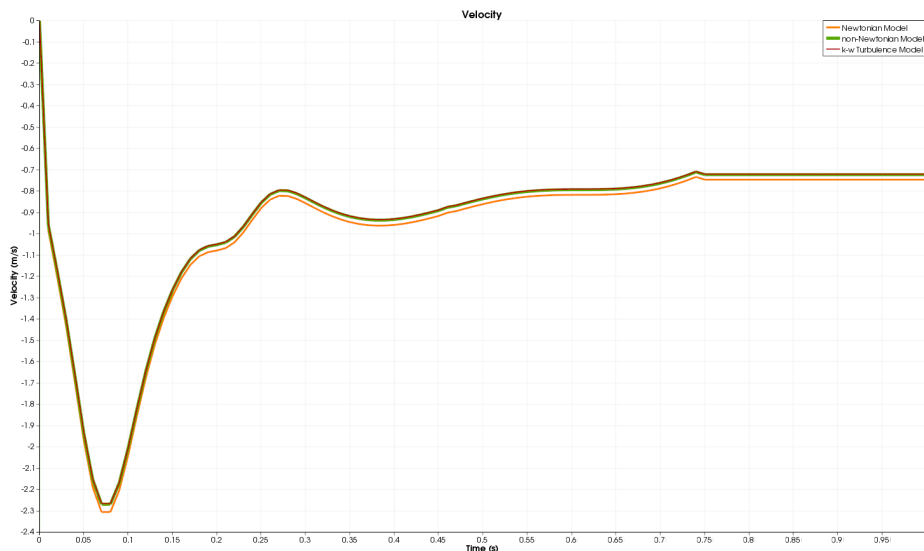


Figure 5.20: Comparison of velocity distribution.

5.3.1.2 Flow in cylindrical stenosed pipe

For the stenosed pipe, results are compared at three different slice points like in Figure 5.21.

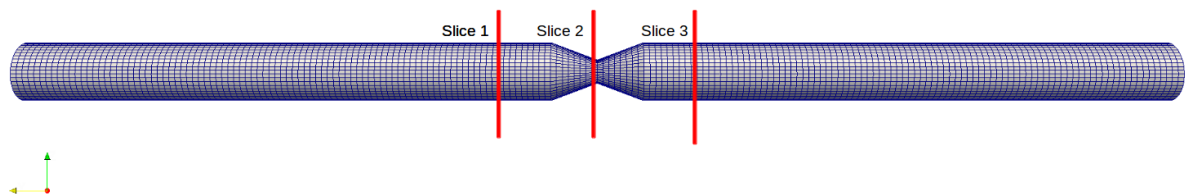


Figure 5.21: Slices that analyzed on the stenosed pipe.

At these slices a point has chosen on the top and on the middle of the slices. And at these points, hemodynamic factors like wall shear stress, velocity and pressure is calculated. Calculation and simulation results are below shown in figures.

Results showed that for Slice1, there is a good agreement in velocity and wall shear stress, like in cylindrical pipe without stenosis. But at Slice2 and Slice3 the differences are getting bigger. Especially at Slice3, after stenosis, there is a big difference between wall shear stress distributions because of the vortexes of flow. Also for all slices, there is an important difference (% 200-250) in pressure distributions between Newtonian and non-Newtonian models.

Figure 5.22, Figure 5.23 and Figure 5.24 show the results for the Slice 1.

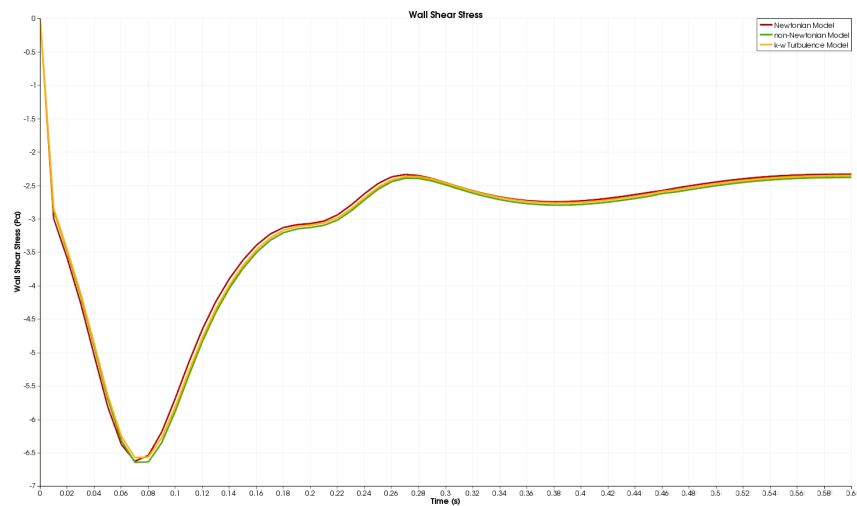


Figure 5.22: Comparison of wall shear stress distribution.

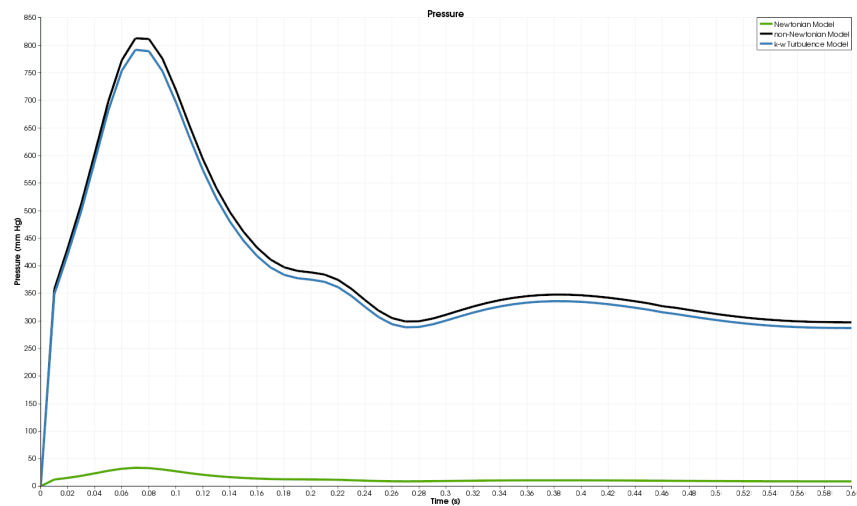


Figure 5.23: Comparison of pressure distribution.

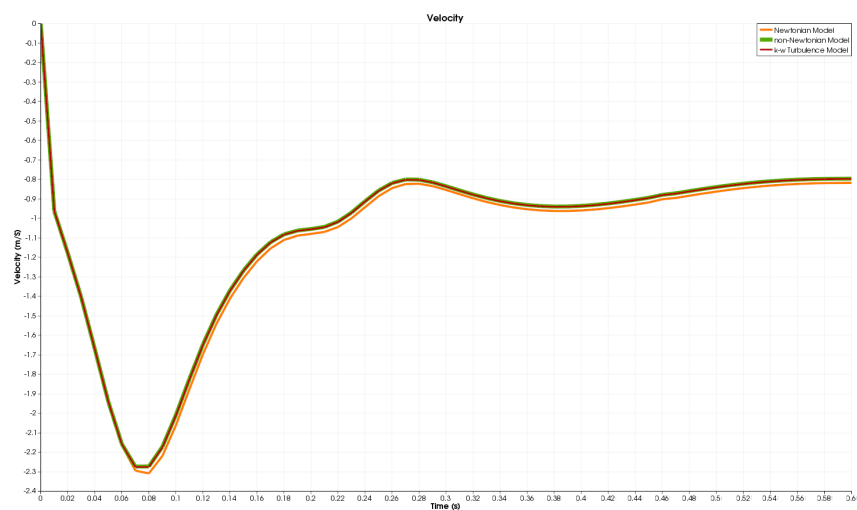


Figure 5.24: Comparison of velocity distribution.

Figure 5.25, Figure 5.26 and Figure 5.27 show the results for the Slice 2.



Figure 5.25: Comparison of wall shear stress distribution.

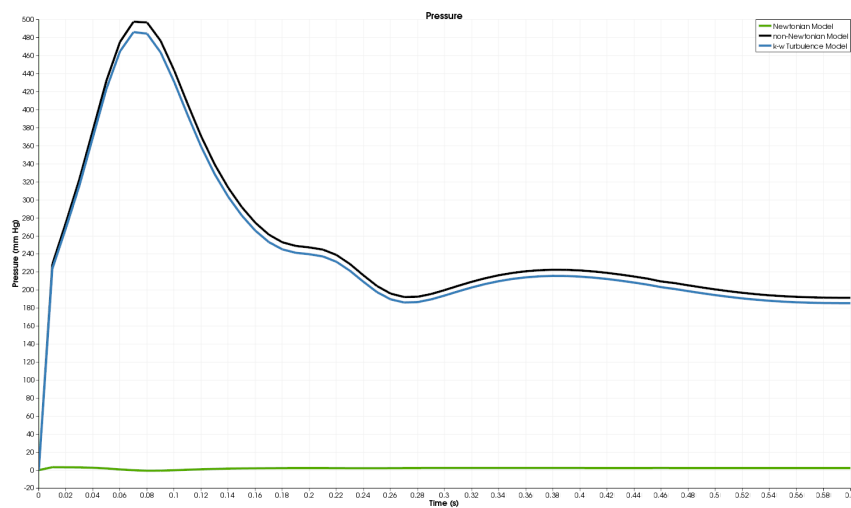


Figure 5.26: Comparison of pressure distribution.

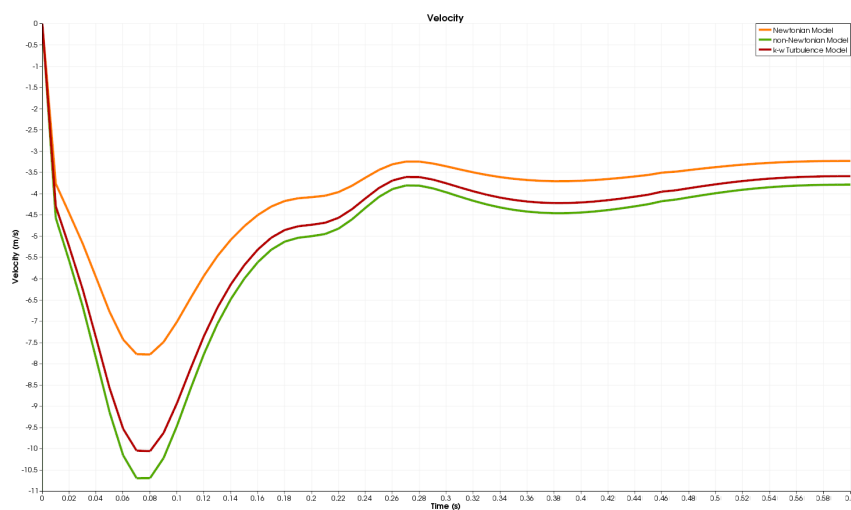


Figure 5.27: Comparison of velocity distribution.

Figure 5.28, Figure 5.29 and Figure 5.30 show the results for the Slice 3.

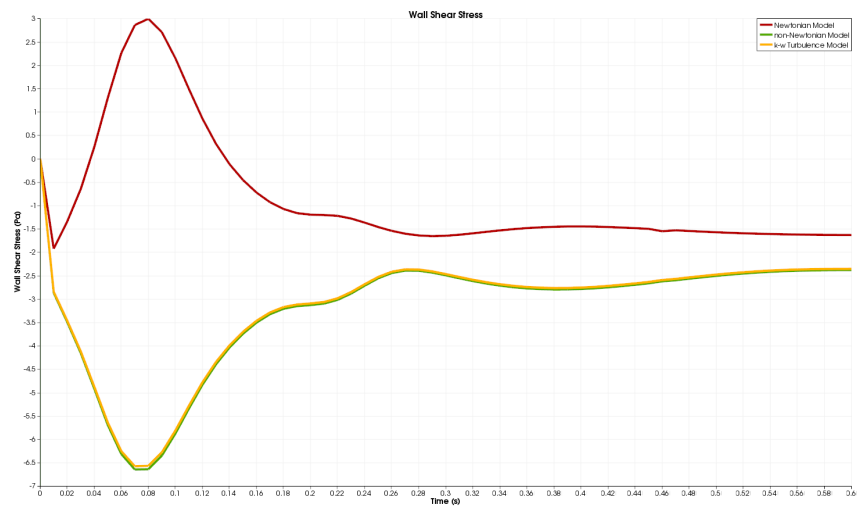


Figure 5.28: Comparison of wall shear stress distribution.

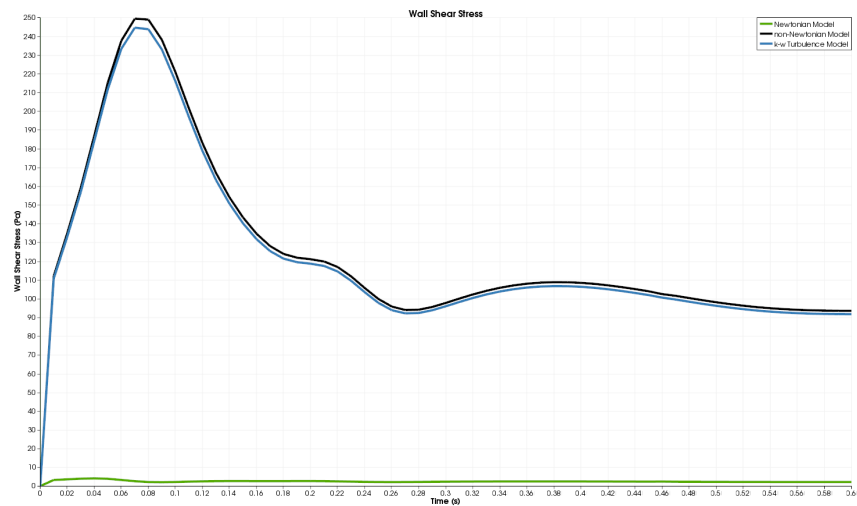


Figure 5.29: Comparison of pressure distribution.

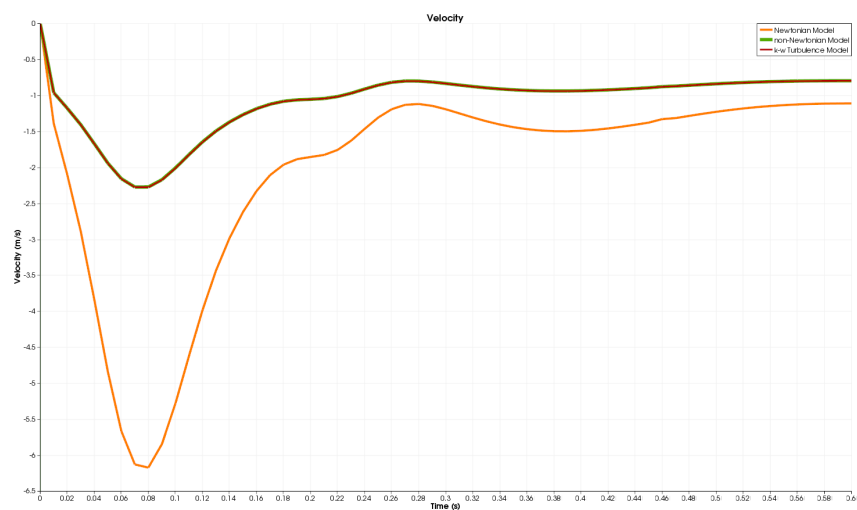


Figure 5.30: Comparison of velocity distribution.

After comparing flow results for three slices at cylindrical stenosed pipe, now we will compare the results for cylindrical stenosed pipe with bypass.

5.3.1.3 Flow in cylindrical stenosed pipe with bypass

And for the stenosed pipe with bypass, results are compared at ten different slice points like in the Figure 5.31.

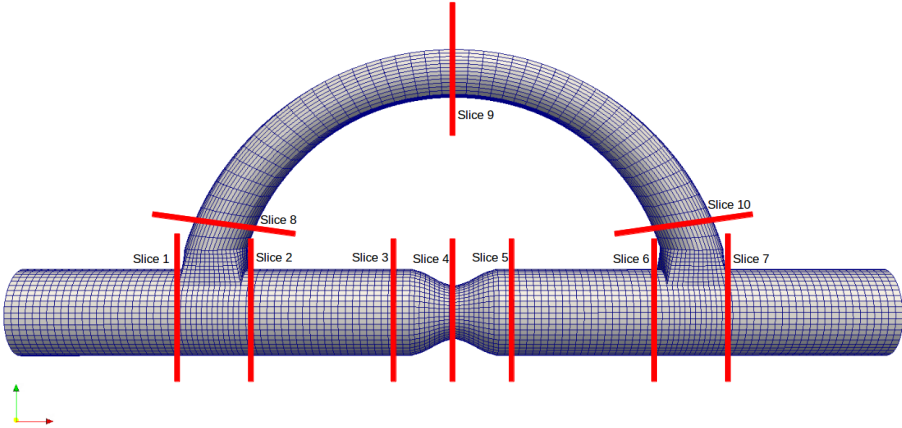


Figure 5.31: Slices that are analyzed on the stenosed pipe.

Figure 5.32, Figure 5.33 and Figure 5.34 show the results for Slice 1 of bypass.

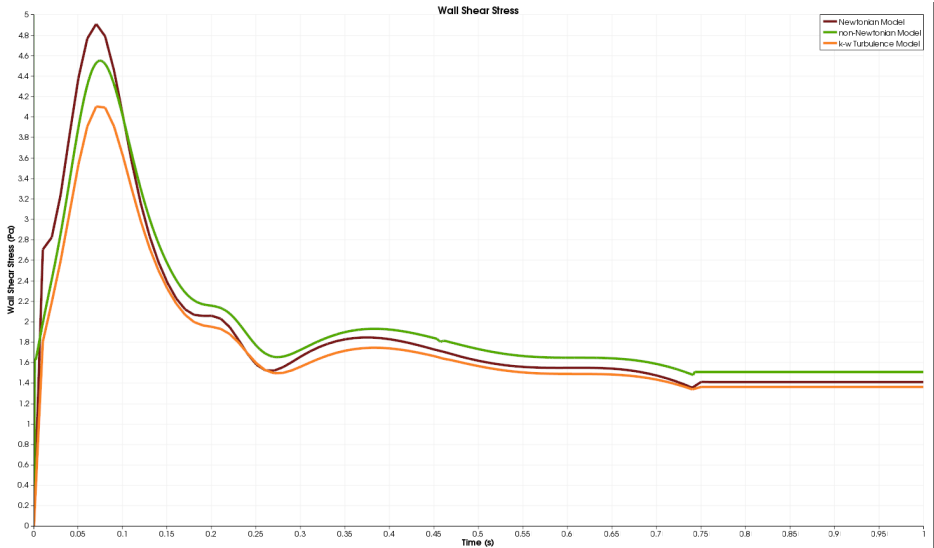


Figure 5.32: Comparison of wall shear stress distribution.

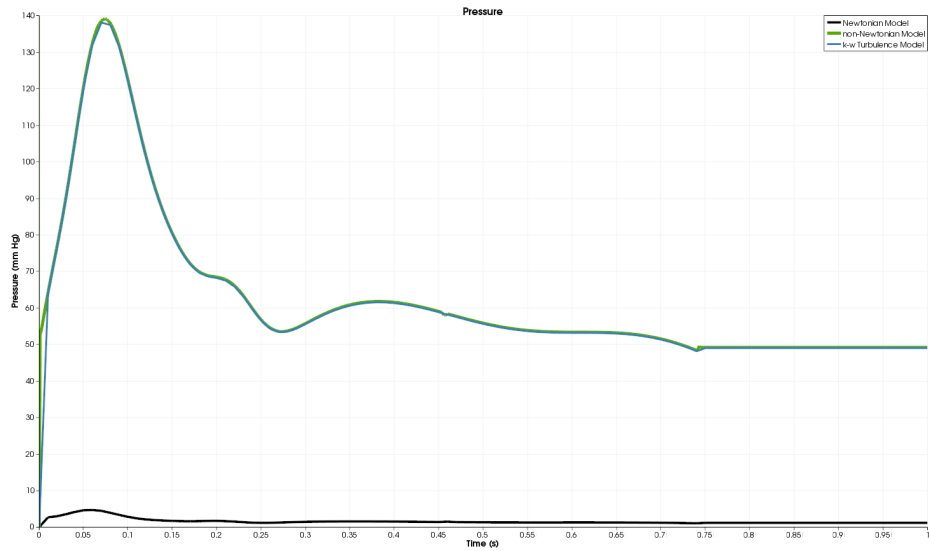


Figure 5.33: Comparison of pressure distribution.

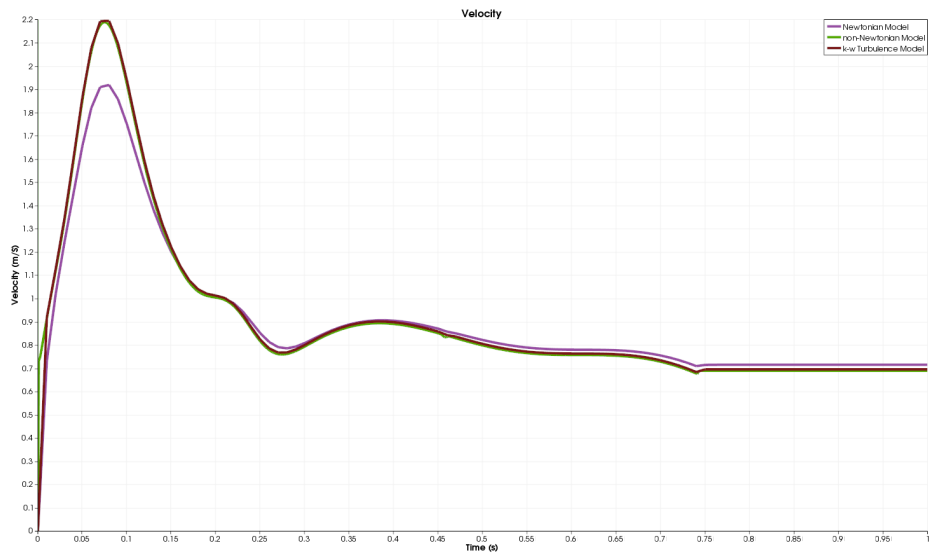


Figure 5.34: Comparison of velocity distribution.

Results for Slice1 showed that wall shear stress distributions are close to each other with Newtonian and non-Newtonian models like in Slice1 for stenosed pipe case. Because of that there is not a stenosis before Slice1, there is nothing to disturb the flow. So wall shear stress and velocity distributions are in a good agreement. On the other hand, still there is a big difference between pressure distributions for Newtonian and non-Newtonian models.

Figure 5.35, Figure 5.36 and Figure 5.37 show the results for the Slice 2.

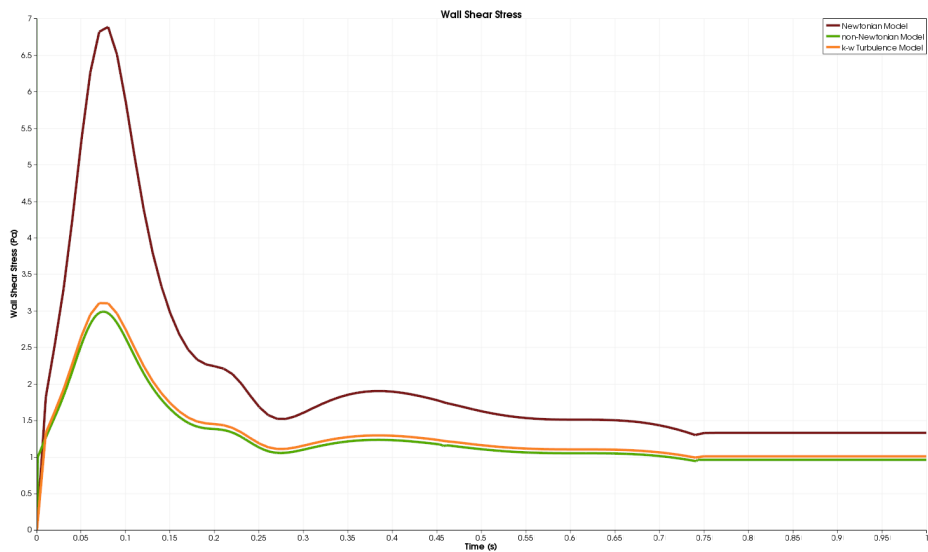


Figure 5.35: Comparison of wall shear stress distribution.

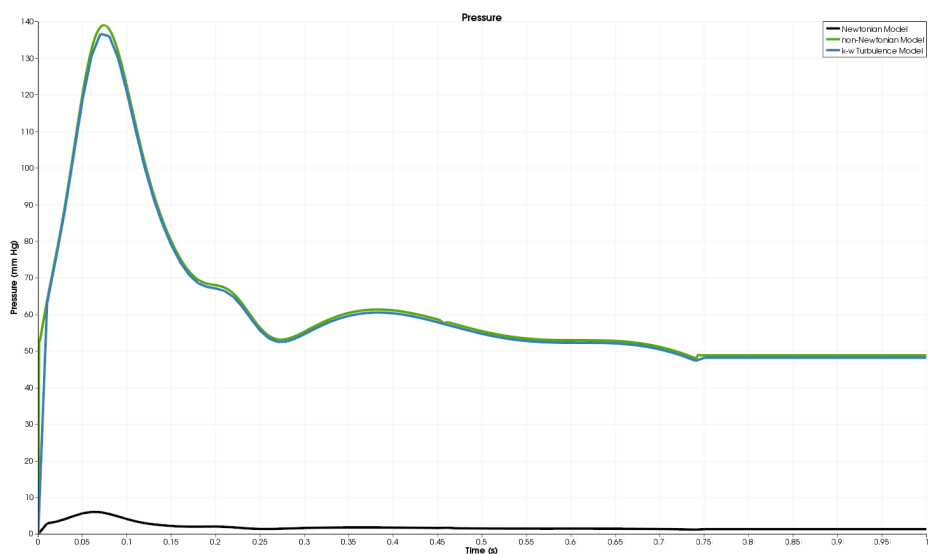


Figure 5.36: Comparison of pressure distribution.

Results for Slice2 showed that, the difference between wall shear stress distributions for Newtonian and non-Newtonian models are getting bigger. Because of Slice2 is after the head of bypass part, flow creates vortexes after seperating to bypass vessel. So it is acceptable that wall shear stress differences are getting bigger. Velocity distributions are in a good agreement for all models. And still there is a big difference between pressure distributions for Newtonian and non-Newtonian models.

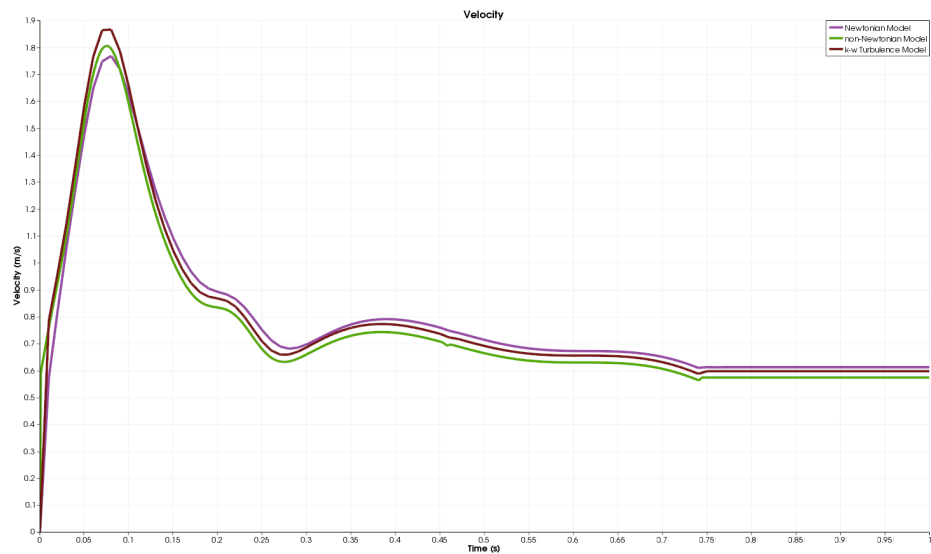


Figure 5.37: Comparison of velocity distribution.

Figure 5.38, Figure 5.39 and Figure 5.40 show the results for the Slice 3.

Results for Slice3 showed that like in Slice1, there is a good agreement between wall shear stress and velocity distributions for Newtonian and non-Newtonian models. It is because, like in the Slice1, there is nothing to disturb the flow and create large vortices. And for the pressure distribution, there is still a big difference (% 200-250) for Newtonian and non-Newtonian models. It can be because of non-Newtonian parameters affects the pressure more than Newtonian model.

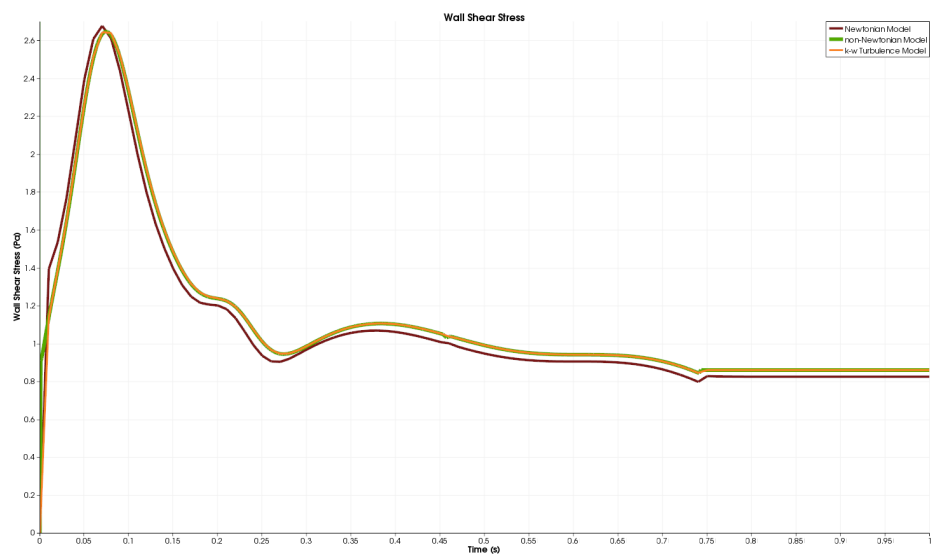


Figure 5.38: Comparison of wall shear stress distribution.

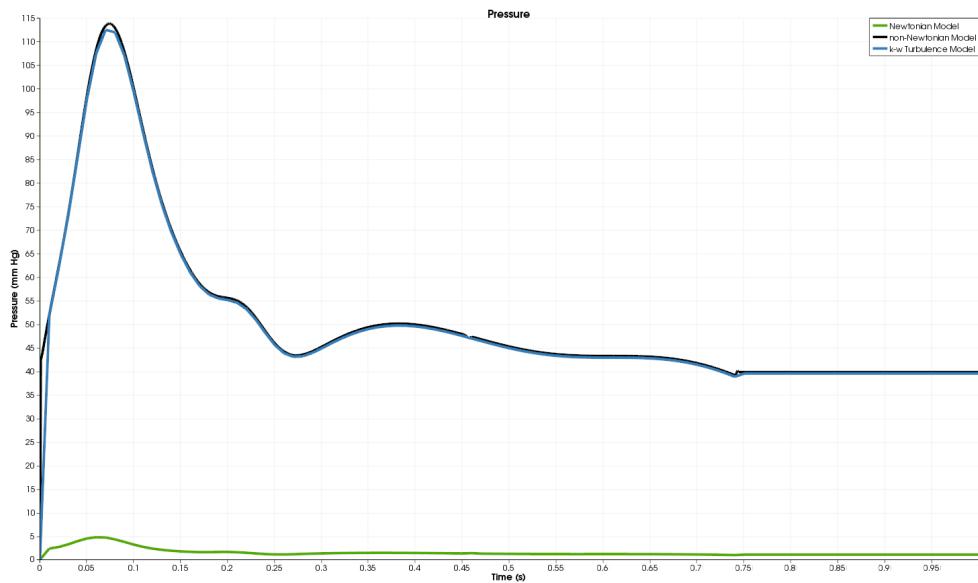


Figure 5.39: Comparison of pressure distribution.

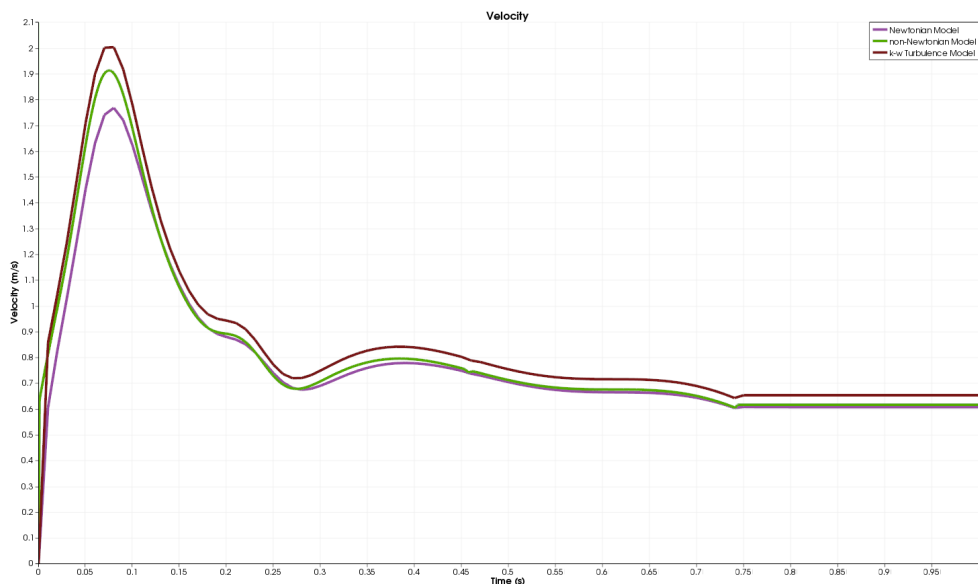


Figure 5.40: Comparison of velocity distribution.

Now we will analyze the simulation results for Slice4. It is the slice at the stenosis part like Slice2 in stenosed vessel geometry. It is expected to see that wall shear stress and velocity distributions difference get bigger than Slice3 in this case.

And also like in all simulation results, it is expected to have big differences for pressure distributions for Newtonian, non-Newtonian and turbulence models.

Figure 5.41, Figure 5.42 and Figure 5.43 show the results for the Slice 4.

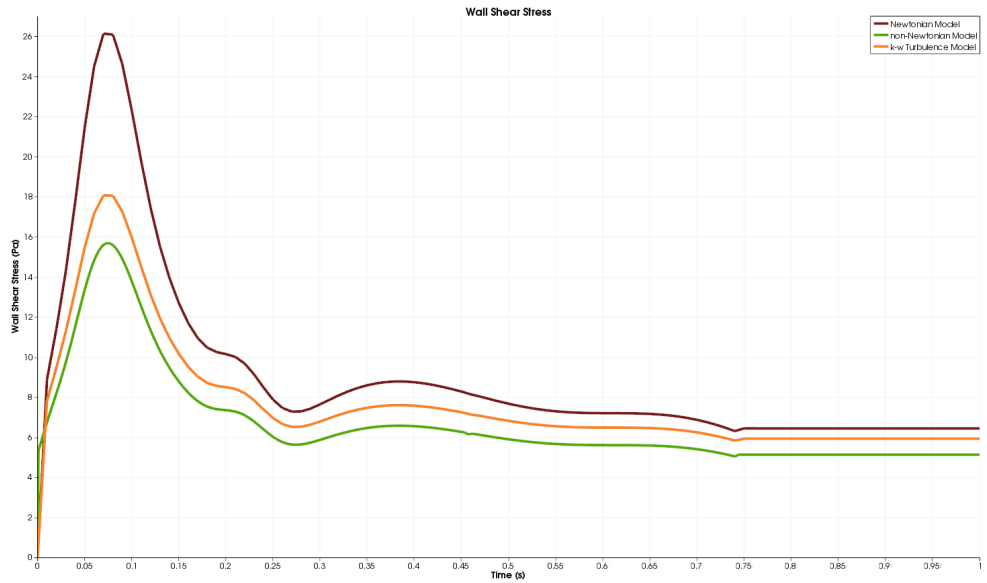


Figure 5.41: Comparison of wall shear stress distribution.

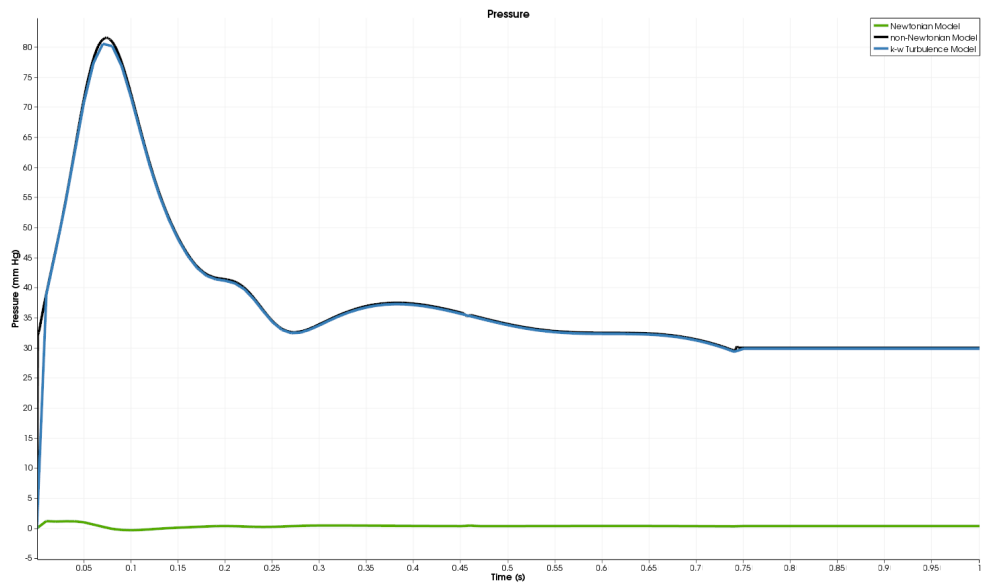


Figure 5.42: Comparison of pressure distribution.

Results for Slice4 showed that the differences between the wall shear stress and velocity distributions are bigger than Slice3, as expected. Because of the geometry of vessel is getting narrower at the stenosed part, it is expected to see that differences are getting bigger. And still there is a big difference for pressure distribution (% 200-250) for Newtonian, non-Newtonian and turbulence models.

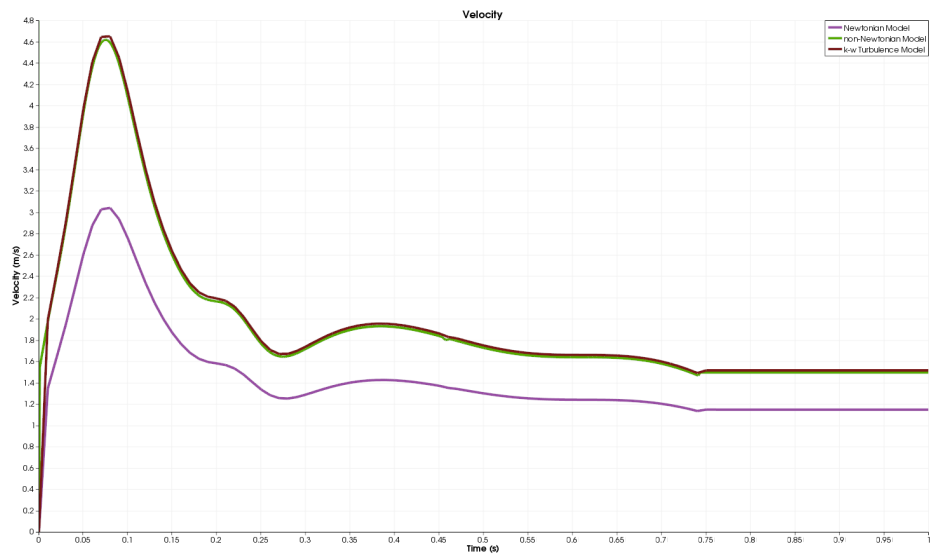


Figure 5.43: Comparison of velocity distribution.

Figure 5.44, Figure 5.45 and Figure 5.46 show the results for the Slice 5.

At Slice5, it is expected to see the results like in Slice3 at the stenosed vessel geometry. Because of the Slice5 is after the stenosed part, the wall shear stress and velocity distributions are expected to get bigger. Because of the vortexes after stenosis.

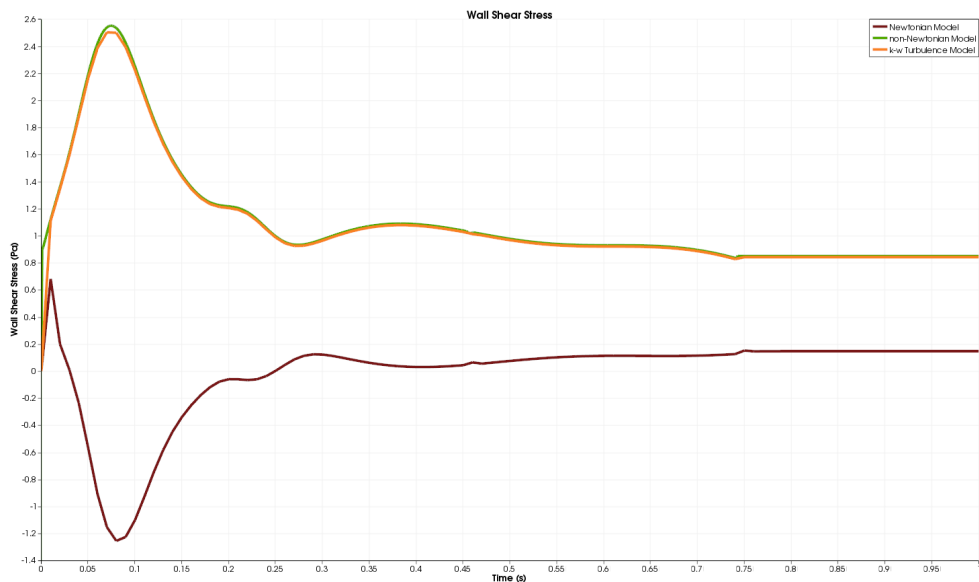


Figure 5.44: Comparison of wall shear stress distribution.

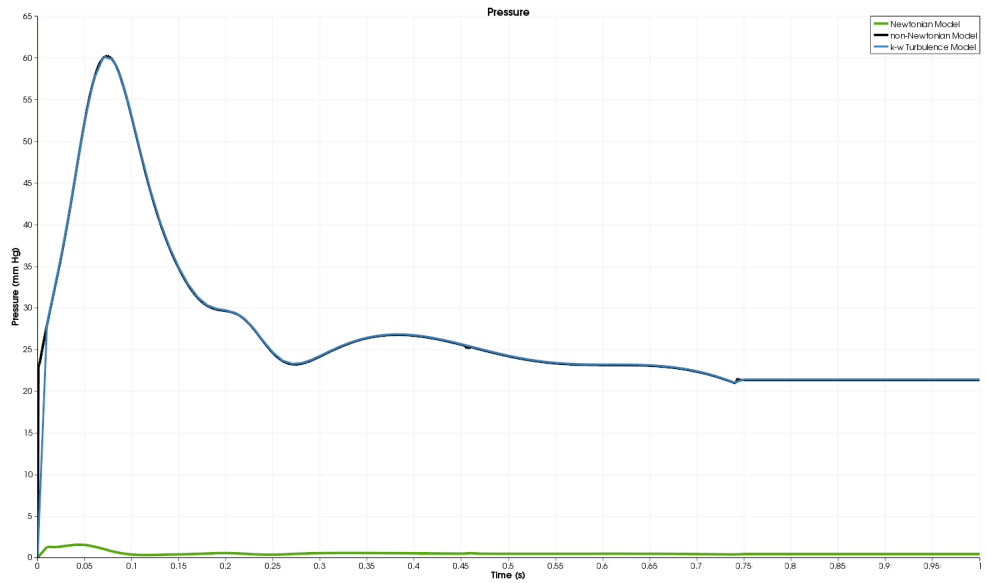


Figure 5.45: Comparison of pressure distribution.

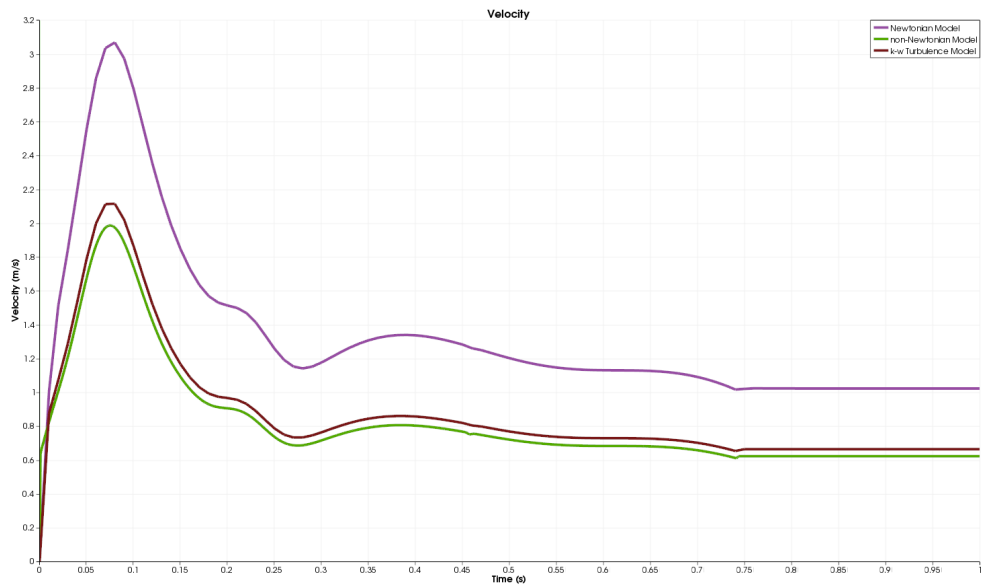


Figure 5.46: Comparison of velocity distribution.

Results for Slice5 showed that difference between wall shear stress and velocity distributions are getting bigger than the results of Slice4. It is because of that Slice5 is after the stenosis part and at stenosis part, velocity is getting bigger and create some vortex parts. So we see that there is a large difference between the wall shear stress distributions. And still there is a large difference between the pressure distributions for Newtonian, non-Newtonian and turbulence models as expected.

Figure 5.47, Figure 5.48 and Figure 5.49 show the results for the Slice 6.

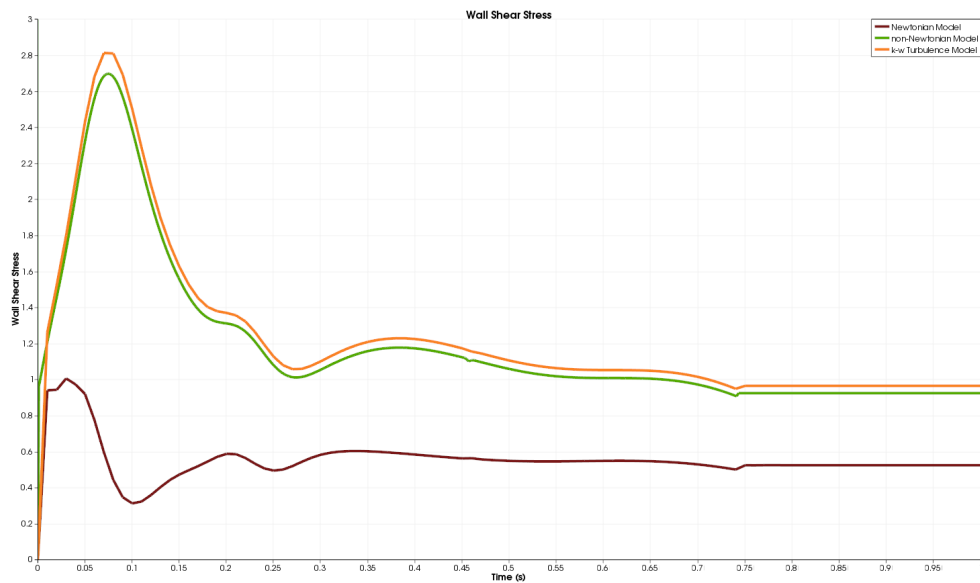


Figure 5.47: Comparison of wall shear stress distribution.

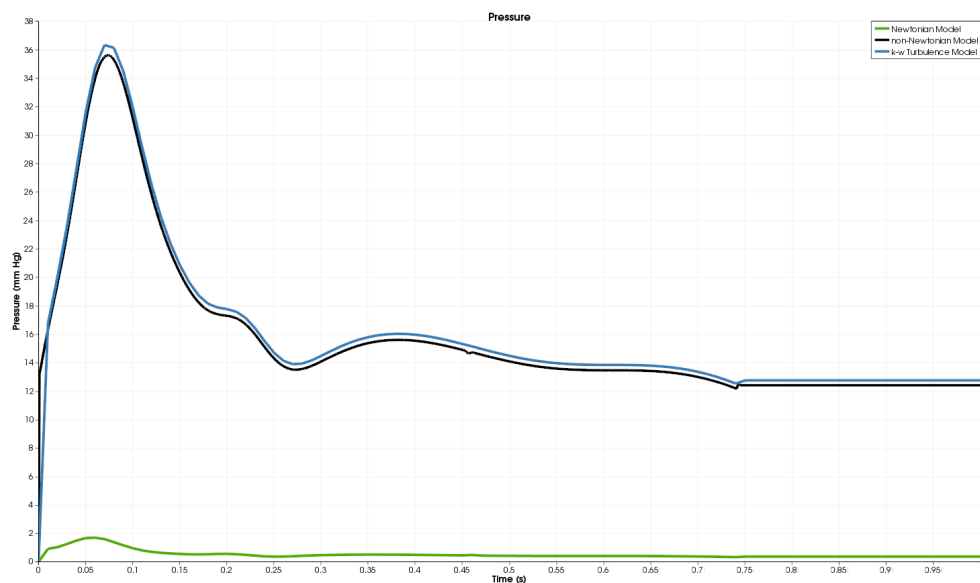


Figure 5.48: Comparison of pressure distribution.

Results for Slice6 showed that difference between wall shear stress and velocity distributions are not bigger than the results of Slice5, but still there is a large difference. It is because of that Slice6 is after the Slice5 where the differences are largest and before the Slice7 that near the toe of the bypass. So it is expected to see that differences are big for the wall shear stress and velocity distributions. And for the pressure distributions, still there is a big difference (% 200-250) for Newtonian and non-Newtonian models.

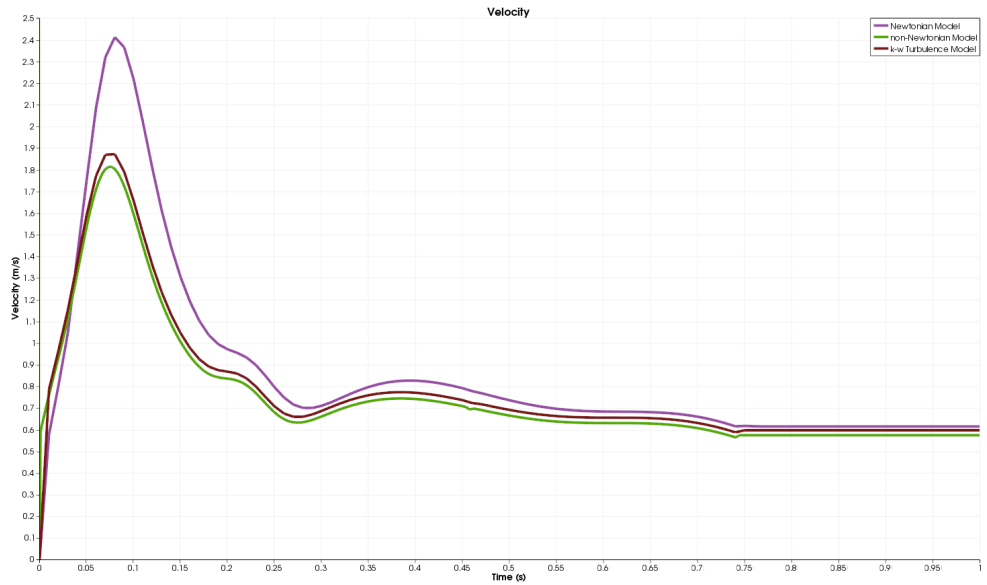


Figure 5.49: Comparison of velocity distribution.

Figure 5.50, Figure 5.51 and Figure 5.52 show the results for the Slice 7.

Slice7 is at the place after the toe of the bypass. So it is expected to see that the large differences between the wall shear stress and velocity distributions are getting smaller at this slice.

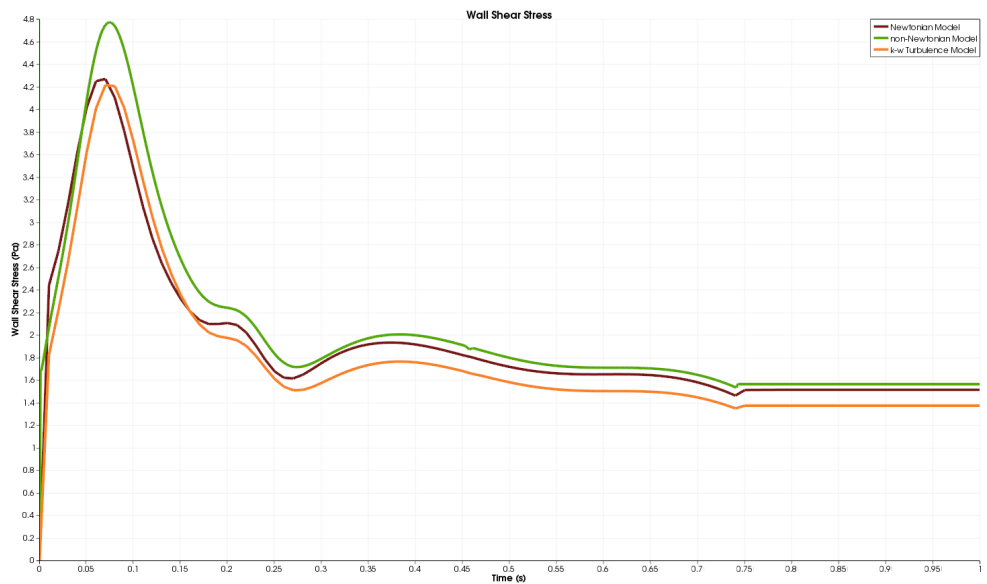


Figure 5.50: Comparison of wall shear stress distribution.

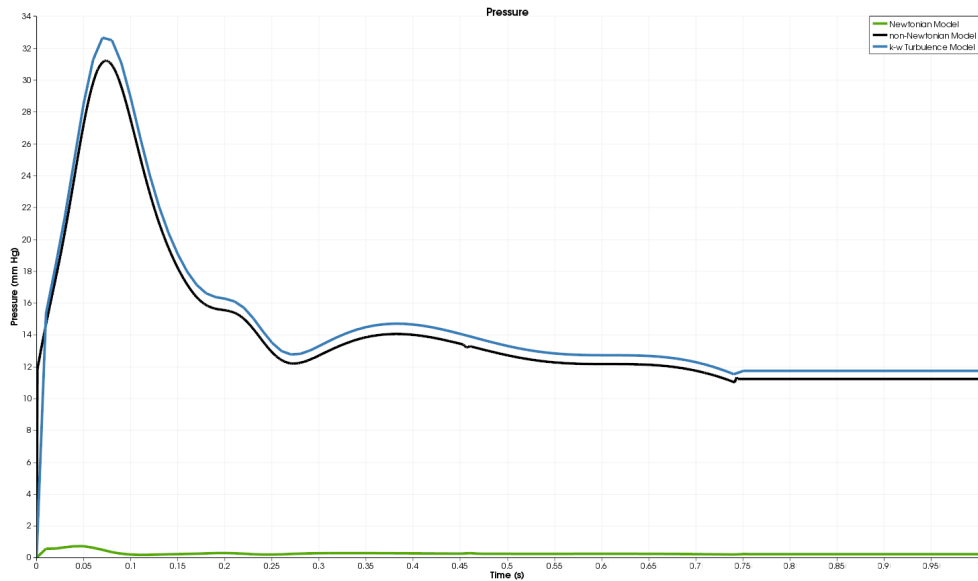


Figure 5.51: Comparison of pressure distribution.

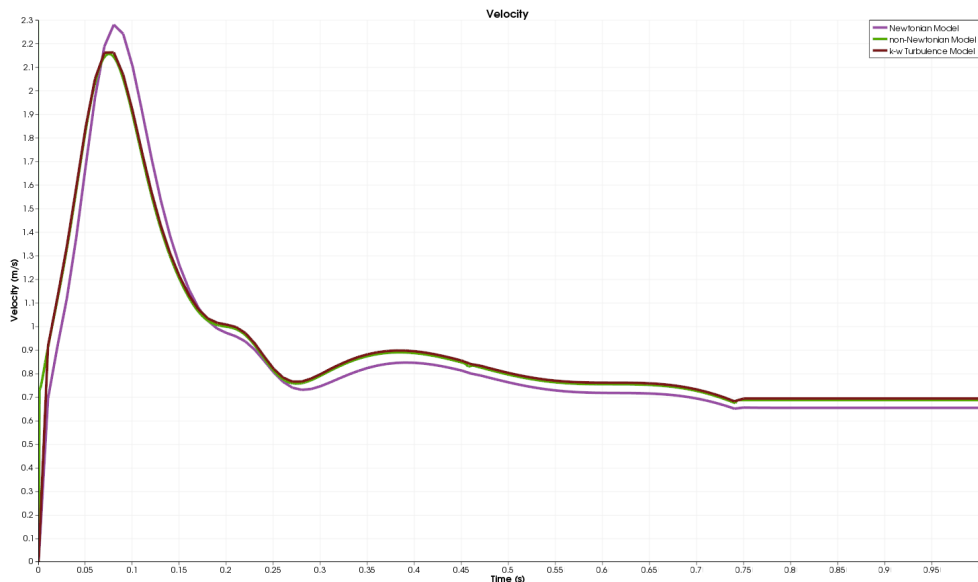


Figure 5.52: Comparison of velocity distribution.

Results for Slice7 showed that differences between the wall shear stress and velocity distributions are getting smaller as expected. The reason is as explained above, Slice7 is after the place of the toe of the bypass. So the large differences that comes from the Slice6 is getting smaller. Also still the difference between the pressure distributions are big (% 200-250) like in other simulation results between Newtonian and non-Newtonian models.

Figure 5.53, Figure 5.54 and Figure 5.55 show the results for the Slice 8.

Slice8 is at the place after the head of the bypass, so we expect that flow create vortex parts here and it will make a big differences between the wall shear stress and velocity distribution.

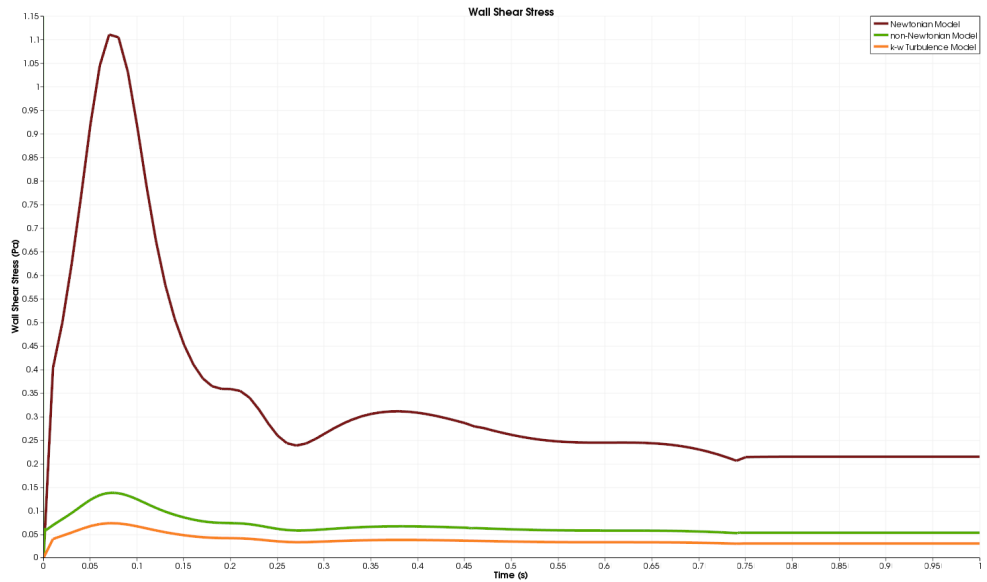


Figure 5.53: Comparison of wall shear stress distribution.

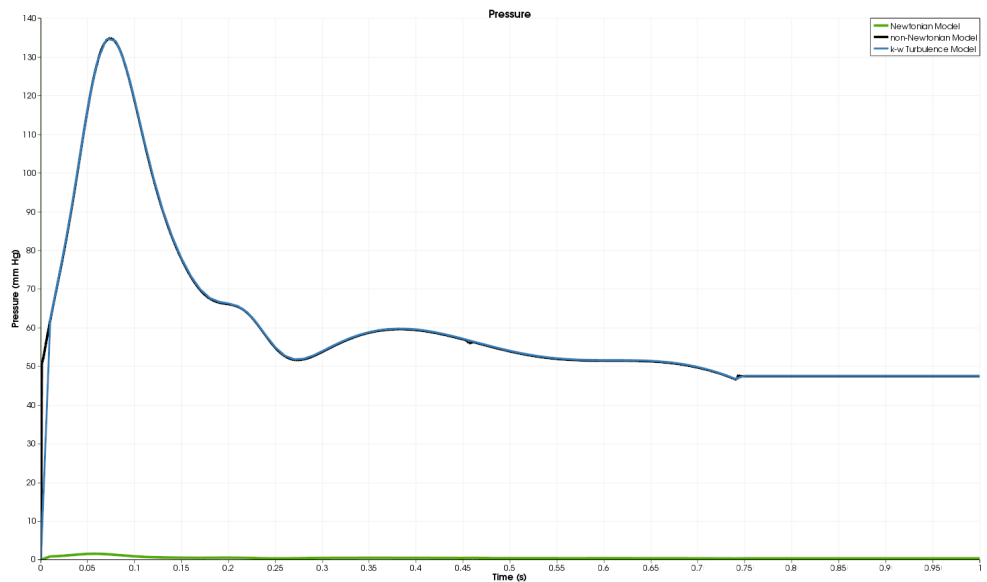


Figure 5.54: Comparison of pressure distribution.

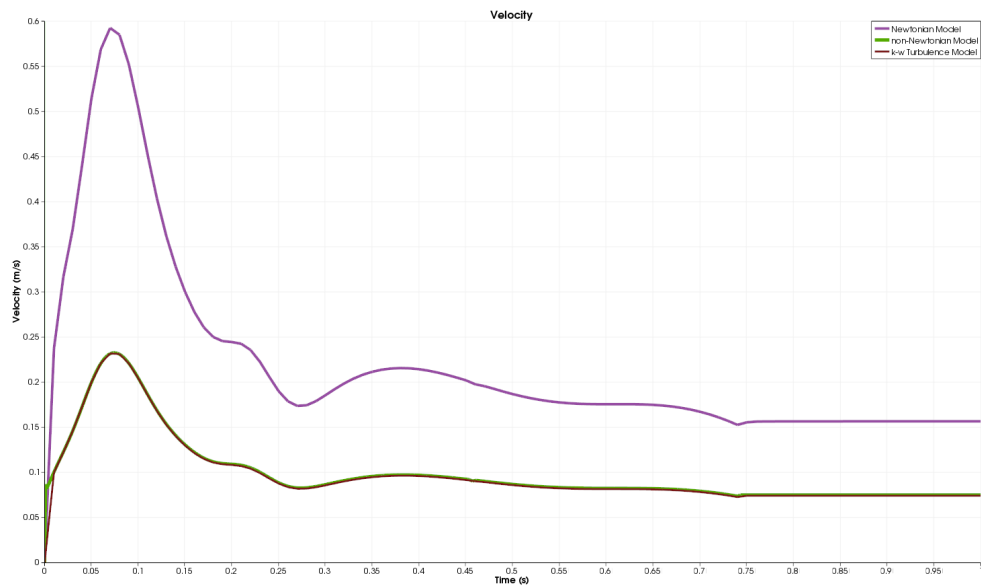


Figure 5.55: Comparison of velocity distribution.

Results for Slice8 showed that the difference between the wall shear stress and the velocity distribution is getting bigger as expected. And it is because of that the place of Slice8 as explained above. Also there are still a big difference between the pressure distributions (% 300-500) for Newtonian, non-Newtonian and turbulence models.

Figure 5.56, Figure 5.57 and Figure 5.58 show the results for the Slice 9.

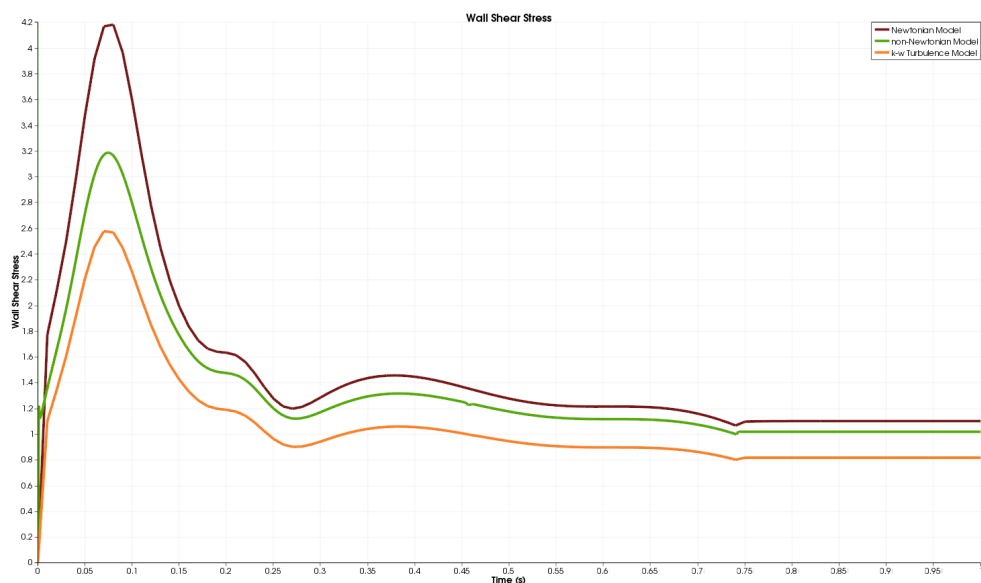


Figure 5.56: Comparison of wall shear stress distribution.

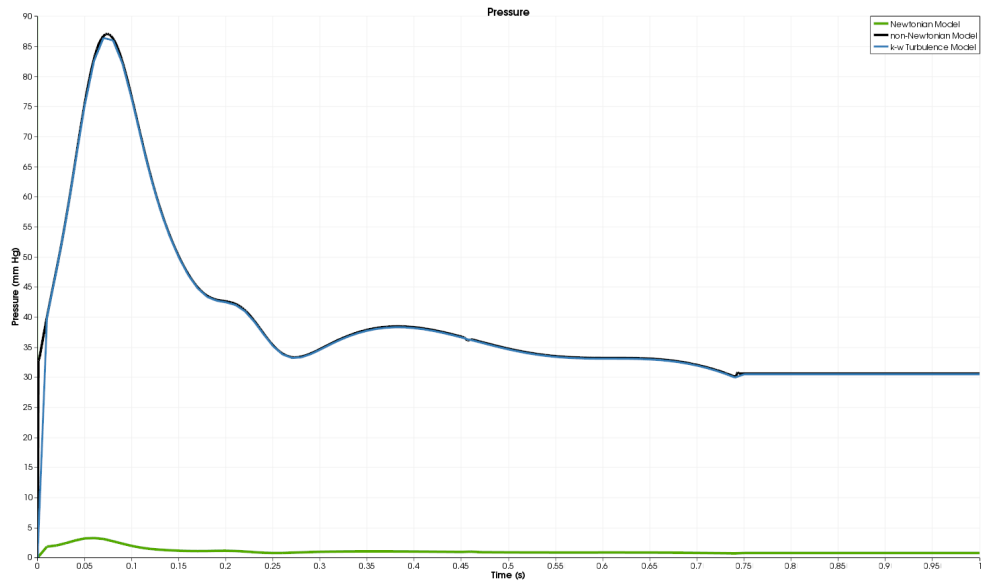


Figure 5.57: Comparison of pressure distribution.

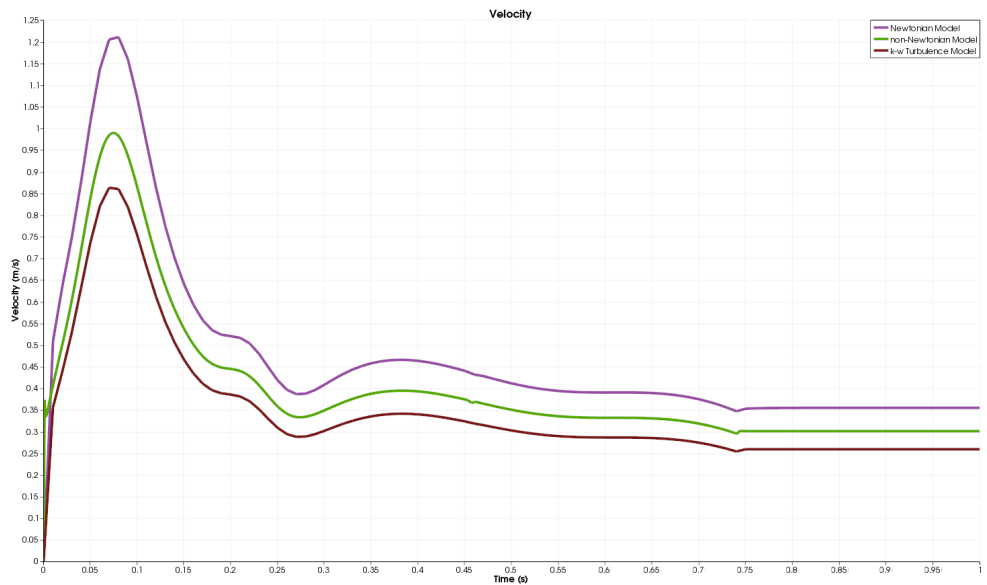


Figure 5.58: Comparison of velocity distribution.

The results for Slice9 showed that the differences between the wall shear stress and the pressure distributions are getting smaller than the results of Slice8. It is because of that the Slice8 was near the head of the bypass but there is not a place to disturb the flow near the Slice9. And Slice9 is at the middle of the bypass vessel, so the differences are getting smaller. And still the difference of the pressure distribution is large (% 500-700) for Newtonian, non-Newtonian and turbulence models.

Figure 5.59, Figure 5.60 and Figure 5.61 show the results for the Slice 10.

Slice10 is the last slice and it is on the place before the toe of the bypass. So it is expected that the differences between the wall shear stress and the pressure distribution is getting bigger.

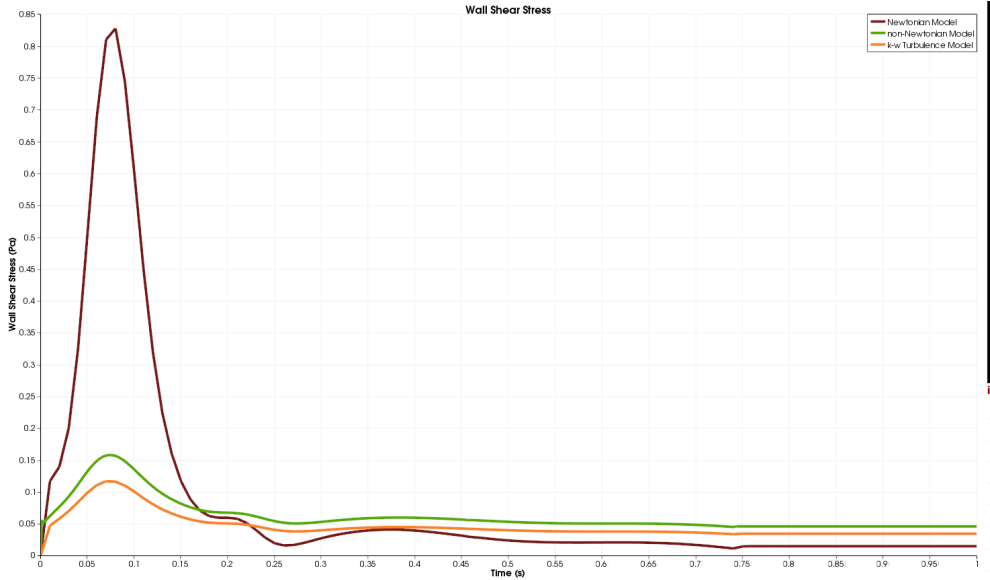


Figure 5.59: Comparison of wall shear stress distribution.

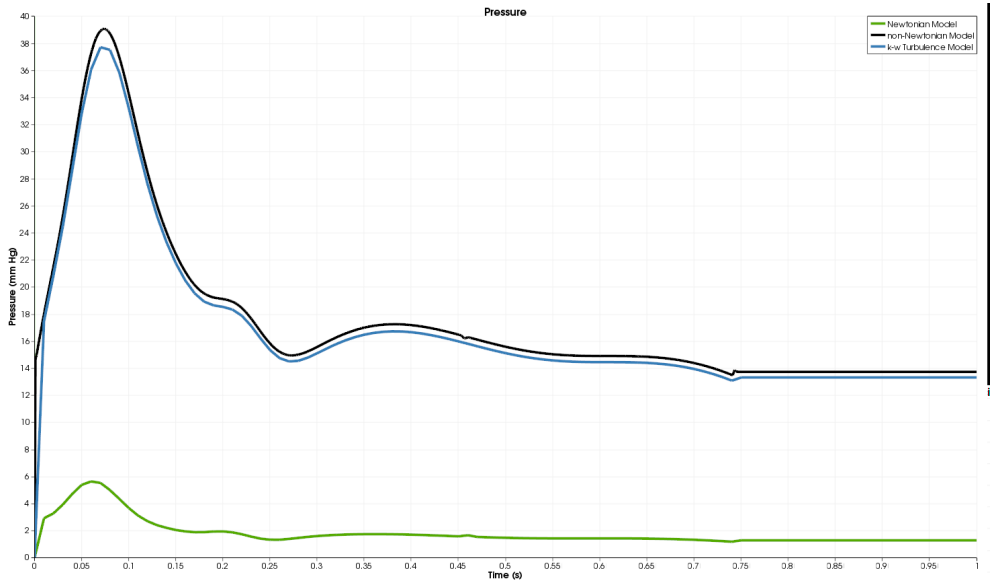


Figure 5.60: Comparison of pressure distribution.

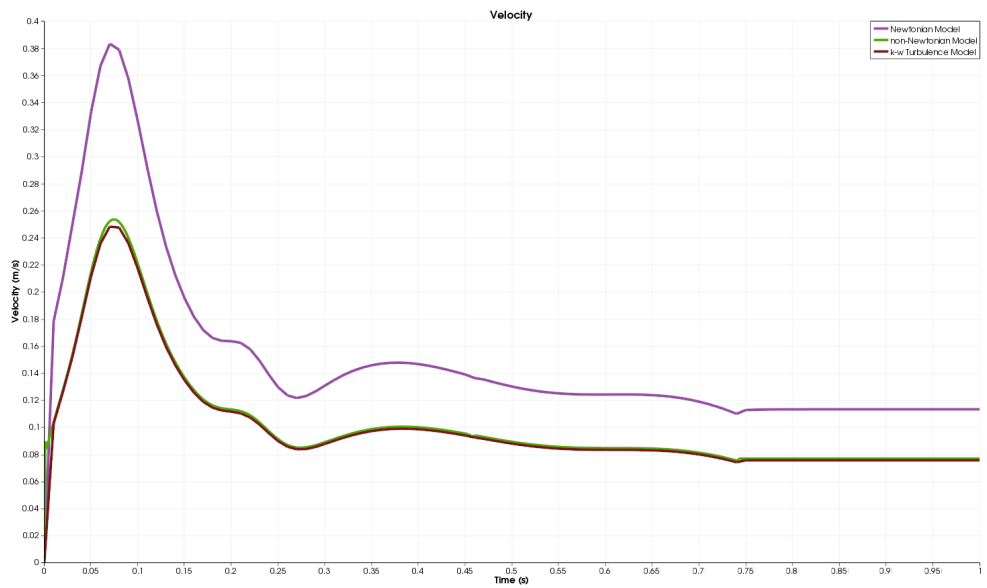


Figure 5.61: Comparison of velocity distribution.

Results for the Slice10 showed that there is a big difference between the wall shear stress and velocity distributions for the Newtonian and non-Newtonian models. It is because of the reason that the place of the Slice10, that we explained above. And for pressure distribution, difference between the Newtonian and non-Newtonian models are still very large (% 200-300).

All simulation results for the slices showed that, near the stenosis or bypass parts, differences between the wall shear stress and velocity distributions are getting bigger than other parts because of the flow creates vortex parts. And for all simulations we showed that pressure distributions have very large differences between the Newtonian, non-Newtonian and turbulence models. It is because of the parameters of non-Newtonian models that Newtonian model does not have. All results for the simulations are acceptable and as we expected.

Now we will create blood flow and vessel wall interaction model and we will compare the results for this case. We aim to show the simulation results for wall shear stress, velocity and pressure distributions and compare them with the blood flow and rigid wall interaction model.

5.3.2 FSI model

Two different meshes are constructed for FSI case, as shown in Figure 5.2 and 5.3 at pre-processing part. And Figure 5.16 shows the place where we take the slice for

the calculations, it is in the middle of the vessel. And the point is taken at the top of the slice for comparing wall shear stress and pressure distributions for Newtonian, non-Newtonian and turbulence models. Initial and boundary conditions are set carefully. Blood flow-vessel wall interaction case is studied only for fixed inlet velocity profile. Wall shear stress and pressure distributions results are obtained and compared with the rigid wall case for Newtonian model, Turbulence & non-Newtonian model and Fluid-Structure Interaction model. Figure 5.62 and 5.63 show the results.

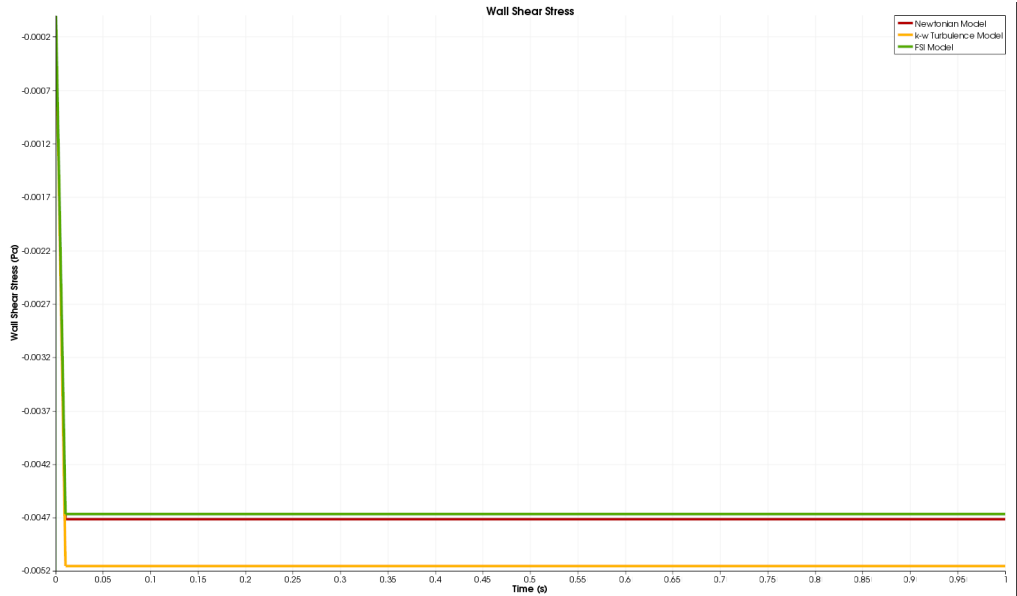


Figure 5.62: Comparison of wall shear stress distribution.

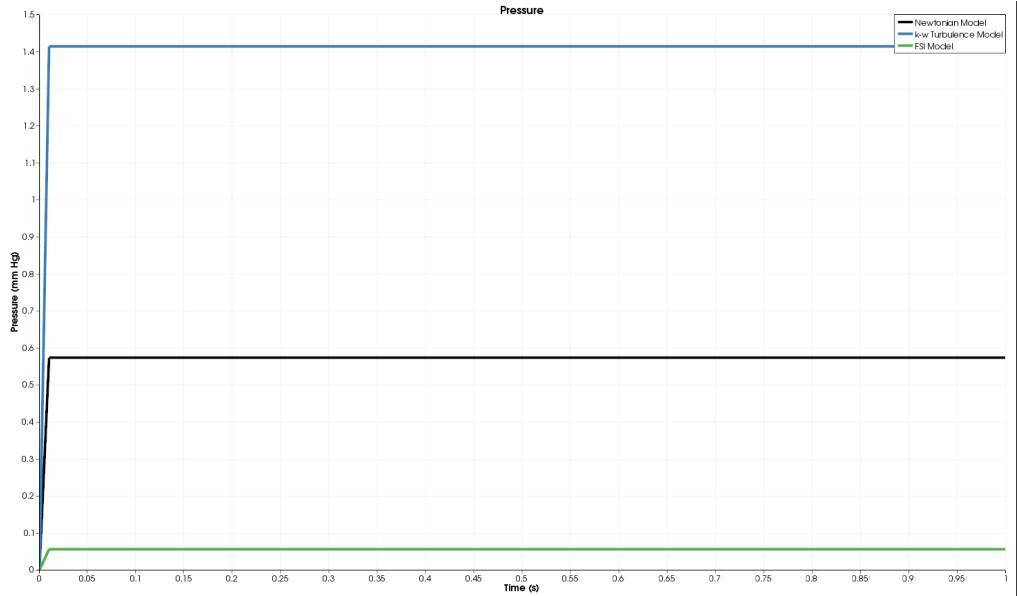


Figure 5.63: Comparison of pressure distribution.

Results of the fluid structure interaction model for the chosen slice showed that there is a difference between wall shear stress distribution for Newtonian, non-Newtonian and turbulence models. FSI results are close to Newtonian results. It can be because of FSI flow is Newtonian and there is not stenosis at the geometry to disturb the flow. So these results are acceptable and as expected. And also for pressure distribution, there is a large difference between Newtonian, non-Newtonian and turbulence models. Between FSI and Newtonian model, there is % 6 difference and between FSI and turbulence model, there is % 14 difference. Results show that FSI model give more realistic results compared to Newtonian, non-Newtonian and turbulence models.

Because of the inlet velocity profile is constant, the difference between the velocity profiles could not be compared. After implementing the Womersley velocity profile, results for the velocity distribution will be compared for all models too.

Studies are ongoing for implementing Womersley inlet profile for FSI. And also FSI solvers are being modified for non-Newtonian and turbulence flows. Then all results will be compared for all models. Then parametric studies will be continued, for example the depth or length of the stenosis and the distance and length of the bypass. After that simulation results will be compared for all parameters and the best options of parameters will be found for the patient.

5.4 Results and Discussions

We modeled the blood flow in coronary artery with and without stenosis and bypassed and without bypassed. All results are compared for Newtonian, non-Newtonian, turbulent flow. We showed the importance of non-Newtonian flow assumption in the blood flow simulations. Bird-Carreau model is used for non-Newtonian flow. Our results reveal that near the stenosis region, there is a strong need for low-Reynolds number turbulence model such as $k - \omega$ SST or kkl-omega transient RANS Model. We used $k - \omega$ SST model for turbulent case. For better simulation of bypass model, moving geometry (blood flow-vessel wall interaction) is required due to the fact that blood wave pressure distorts the vessel wall, vessel wall constrained the blood flow near the boundary layer. So we implemented loose-coupling fluid-structure interaction model between blood flow and vessel wall. Results showed that fluid structure interaction gives more realistic results, especially for wall shear stress. Fluid structure interaction model

is implemented for the cylindrical pipe without stenosis and constant velocity profile is used. Womersley velocity profile implementation to FSI for OpenFOAM studies are still in progress. And also fluid structure interaction model will be implemented for stenosed and bypass cases. Strongly-coupled model will be implemented and compared with loosely-coupled model. OpenFOAM has only icoFsiFoam solver for FSI models, so icoFsiFoam solver has to be modified and non-Newtonian and turbulence models has to be implemented to solve these cases and compare with the rigid wall case.

For future study, there is a need for wide range of tests for different stenosis and bypass parameters as shown in Figure 5.64, 5.65 and 5.66. And also there is a need for wide range of tests for flow conditions such as different velocities and viscosities (fixed and FSI cases).

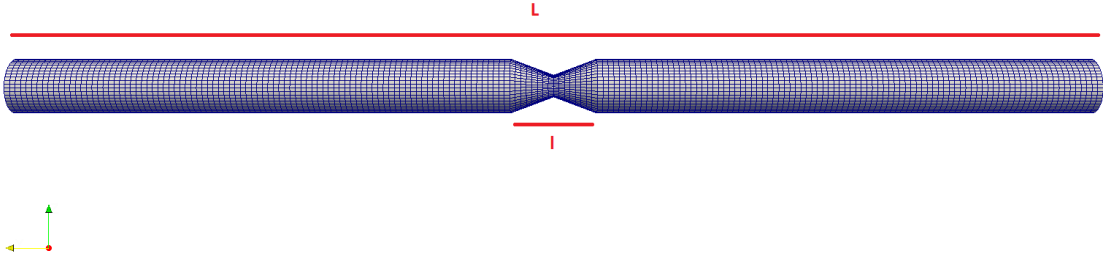


Figure 5.64: L: Length of the vessel, l: Length of stenosis region.

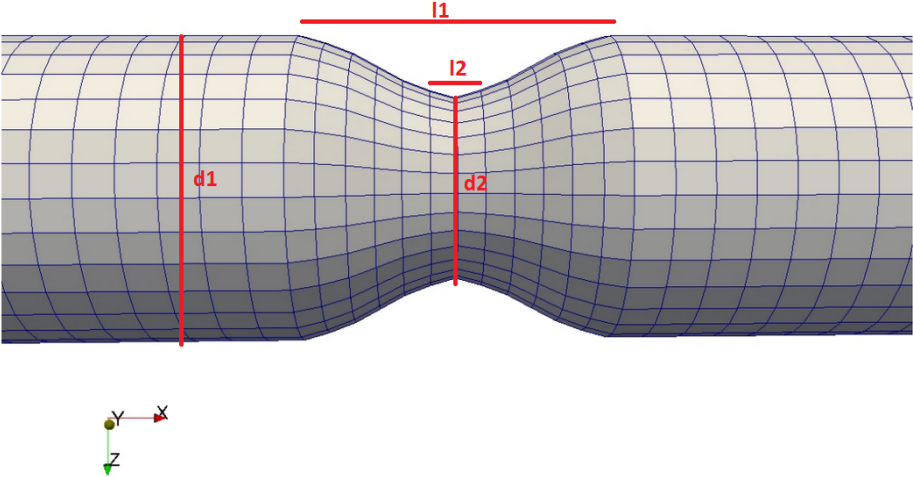


Figure 5.65: d1: Diameter of the vessel, d2: Diameter of stenosis region, l1: Length of stenosis region, l2: Length of stenosis.

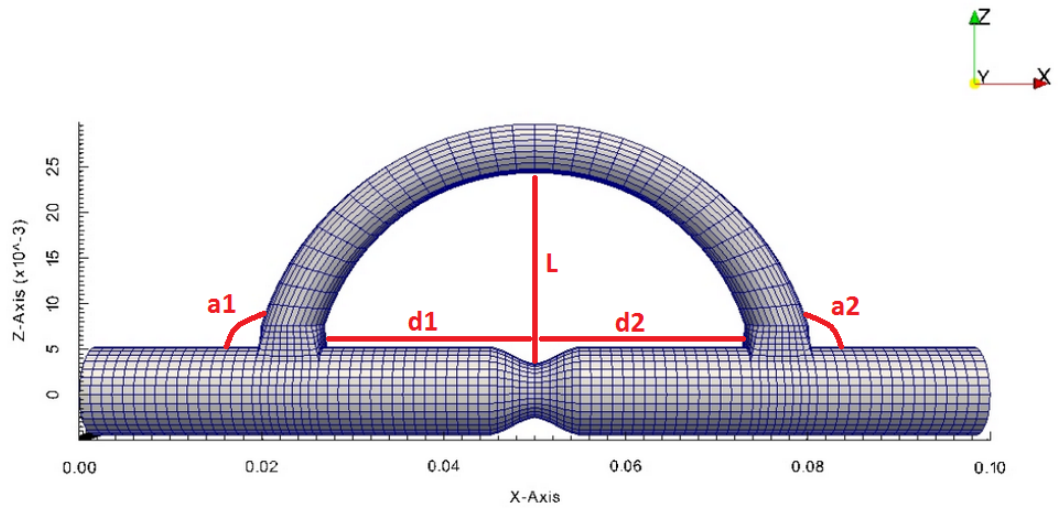


Figure 5.66: L: Length of bypass, a1,a2: Angle of bypass inlet and outlet, d1,d2: Distance of bypass inlet and outlet from the stenosis region.

Also different low-Reynolds turbulence models should be extensively tested. For non-Newtonian and turbulence models in FSI simulations, the solvers in OpenFOAM should be modified and the solvers developed for non-FSI case should be included in the FSI models.

6. CONCLUSION

In this study, three different artificial vessel geometries are constructed by using OpenFOAM software, first one is a cylindrical pipe without stenosis, second one is a cylindrical pipe with stenosis and the third one is a cylindrical stenosed pipe with bypass. Hexahedral mesh is created for all cases. Inlet velocity profile is implemented for constant and Womersley inlet profile and results are compared. Results showed that Womersley profile is a developed flow and for blood flow it gives more realistic results. So we used Womersley profile for all simulations. Flow is assumed as Newtonian, non-Newtonian and turbulent flow. For Newtonian model, icoFoam solver, which is a transient solver for incompressible, laminar flow of Newtonian fluids, is used. Bird-Carreau model is used for non-Newtonian flow and nonNewtonianIcoFoam solver, which is a transient solver for incompressible, laminar flow of non-Newtonian fluids, is used. $k-\omega$ SST turbulence model is used for turbulent flow and simpleFoam solver, which is a steady-state solver for incompressible, turbulent flow, is used. After boundary conditions and solvers are set carefully, the results of the simulations are obtained. All results are compared for Newtonian, non-Newtonian and turbulent flow models. Results showed that non-Newtonian model gives more realistic results than Newtonian model, but near the stenosis regions, turbulent model gives more realistic results because of at this regions, flow creates vortexes.

After these results, blood flow-vessel wall interaction model is studied. Fluid and solid meshes are created as hexahedral and boundary conditions are set between fluid and solid part. Inlet velocity profile is assumed as constant. icoFsiFoam solver is used which solves fluid-structure interaction by loose-coupling model. After the simulation results, wall shear stress and pressure values are compared with Newtonian, non-Newtonian and turbulence models. Results showed that FSI coupling approach gives more realistic results for the hemodynamic factors. Especially for wall shear stress and pressure distributions, it is analyzed that there is a large difference (% 6-20) between the fluid-structure interaction and rigid wall assumption models.

Studies are still ongoing for cylindrical stenosed pipe and cylindrical stenosed pipe with bypass. And also Womersley velocity implementation is being studied. But still there is a need of wide range of tests for different stenosis and bypass parameters. Also icoFsiFoam solver has to be modified and non-Newtonian and turbulence models has to be included to this solver.

REFERENCES

- [1] **WHOROE** (2002). European Health Report for 2002 in European Series 97, **Technical Report**, World Health Organization Regional Office for Europe, East Lansing, Michigan.
- [2] **ECDS**, British Heart Foundation of Health Promotion Research Group, <http://www.heartstats.org>.
- [3] **Ohayon, J., Finet, G., Gharib, M., Herzka, D., Tracqui, P., Heroux, J., Rioufol, G., Kotys, M., Elagha, A. and Pettigrew, R.** (2008). Necrotic core thickness and positive arterial remodeling index: emergent biomechanical factors for evaluating the risk of plaque rupture, *American Journal of Physiology*, H717–H727.
- [4] **Taylor, C., Hughes, T. and Zarins, C.** (1998). Finite element modeling of blood flow in arteries, *Computer Methods in Applied Mechanics and Engineering*, 155–196.
- [5] **Oshima, M., Torii, R., Kobayashi, T., Taniguchi, N. and Takagi, K.** (2001). Finite element simulation of blood flow in the cerebral artery, *American Journal of Physiology*, 661–671.
- [6] **Cebral, J., Castro, M., Soto, O., Lohner, R. and Alperin, N.** (2003). Blood-flow models of the circle of Willis from magnetic resonance data, *Journal of Engineering Mathematics*, 369–386.
- [7] **Shojima, M., Oshima, M., Takagi, K., Torii, R., Hayakawa, M., Katada, K., Morita, A. and Kirino, T.** (2004). Magnitude and Role of Wall Shear Stress on Cerebral Aneurysm: Computational Fluid Dynamic Study of 20 Middle Cerebral Artery Aneurysms, *Stroke*, **35**(11), 2500–2505.
- [8] **Salmon, S., Thiriet, M. and Gerbeau, J.** (2003). Medical image – based computational model of pulsatile flow in saccular aneurysms, *ESAIM: Mathematical Modelling and Numerical Analysis - Modélisation Mathématique et Analyse Numérique*, **37**(4), 663–679.
- [9] **Tezduyar, T.E., Sathe, S., Cragin, T., Nanna, B., Conklin, B.S., Pausewang, J. and Schwaab, M.** (2007). Modelling of fluid–structure interactions with the space–time finite elements: Arterial fluid mechanics, *International Journal for Numerical Methods in Fluids*, **54**, 901–922.
- [10] **Bazilevs, Y., Calo, V., Hughes, T. and Zhang, Y.** (2008). Isogeometric fluid-structure interaction: theory, algorithms, and computations, *Computational Mechanics*, **43**(1), 3–37.

- [11] **Piskin, S., Aribas, E. and Celebi, M.S.** (2011). A parametric (inlet) flow analysis of 3D human carotid artery using realistic geometry, *Journal of Biomechanics*, **44, Supplement 1(0)**, 17 –, abstracts of the Fifth International Participated National Biomechanics Congress Fifth International Participated National Biomechanics Congress.
- [12] **Piskin, S. and Celebi, M.** (2012). Numerical blood flow simulation with predefined artery movement, *Biomedical Engineering and Informatics (BMEI), 2012 5th International Conference on*, pp.654–658.
- [13] **Arıbaş, E., Şenol Pişkin and Çelebi, M.S.** (2011). 3D flow simulation at the geometry of thirteen main arteries of a human, *Journal of Biomechanics*, **44, Supplement 1(0)**, 16 –, abstracts of the Fifth International Participated National Biomechanics Congress Fifth International Participated National Biomechanics Congress.
- [14] **Shaaban, A. and Duerinckx, A.** (2000). Wall shear stress and early atherosclerosis: a review, *American Journal of Roentgenology*, 1657–1665.
- [15] **Sforza, D.M., Putman, C.M. and Cebal, J.R.** (2009). Hemodynamics of Cerebral Aneurysms, *Annual Review of Fluid Mechanics*, **41(1)**, 91–107.
- [16] **Levesque, M., Liepsch, D., Moravec, S. and Nerem, R.** (1986). Correlation of endothelial cell shape and wall shear stress in a stenosed dog aorta, *Arteriosclerosis*, 220–229.
- [17] **Kondo, S., Hashimoto, N., Kikuchi, H., Hazama, F., Nagata, I. and Kataoka, H.** (1997). Cerebral Aneurysms Arising at Nonbranching Sites: An Experimental Study, *Stroke*, **28(2)**, 398–404.
- [18] **Meng, H., Wang, Z., Hoi, Y., Gao, L., Metaxa, E., Swartz, D.D. and Kolega, J.** (2007). Complex Hemodynamics at the Apex of an Arterial Bifurcation Induces Vascular Remodeling Resembling Cerebral Aneurysm Initiation, *Stroke*, **38(6)**, 1924–1931.
- [19] **Okano, M. and Yoshida, Y.** (1994). Junction complexes of endothelial cells in atherosclerosis-prone and atherosclerosis-resistant regions on flow dividers of brachiocephalic bifurcations in the rabbit aorta, *Biorheology*, 155–161.
- [20] **Boussel, L., Rayz, V., McCulloch, C., Martin, A., Acevedo-Bolton, G., Lawton, M., Higashida, R., Smith, W.S., Young, W.L. and Saloner, D.** (2008). Aneurysm Growth Occurs at Region of Low Wall Shear Stress: Patient-Specific Correlation of Hemodynamics and Growth in a Longitudinal Study, *Stroke*, **39(11)**, 2997–3002.
- [21] **Figueroa, C., Vignon-Clementel, I., Jansen, K., Hughes, T. and Taylor, C.** (2006). A coupled momentum method for modeling blood flow in three-dimensional deformable arteries, *COMPUTER METHODS IN APPLIED MECHANICS AND ENGINEERING*, **195(41-43)**, 5685–5706.
- [22] **Wolters, B., Rutten, M., Schurink, G., Kose, U., de Hart, J. and van de Vosse, F.** (2005). A patient-specific computational model of fluid–structure

interaction in abdominal aortic aneurysms, *Medical Engineering and Physics*, **27**(10), 871 – 883.

- [23] **Bazilevs, Y., Calo, V., Zhang, Y. and Hughes, T.** (2006). Isogeometric Fluid–structure Interaction Analysis with Applications to Arterial Blood Flow, *Computational Mechanics*, **38**(4-5), 310–322.
- [24] **Torii, R., Oshima, M., Kobayashi, T., Takagi, K. and Tezduyar, T.E.** (2007). Influence of wall elasticity in patient-specific hemodynamic simulations, *Computers and Fluids*, **36**(1), 160 – 168, challenges and Advances in Flow Simulation and Modeling.
- [25] **Torii, R., Oshima, M., Kobayashi, T., Takagi, K. and Tezduyar, T.E.** (2006). Computer modeling of cardiovascular fluid–structure interactions with the deforming-spatial-domain/stabilized space–time formulation, *Computer Methods in Applied Mechanics and Engineering*, **195**(13–16), 1885 – 1895, a Tribute to Thomas J.R. Hughes on the Occasion of his 60th Birthday.
- [26] **Torii, R., Oshima, M., Kobayashi, T., Takagi, K. and Tezduyar, T.** (2006). Fluid–structure Interaction Modeling of Aneurysmal Conditions with High and Normal Blood Pressures, *Computational Mechanics*, **38**(4-5), 482–490.
- [27] **Scotti, C.M. and Finol, E.A.** (2007). Compliant biomechanics of abdominal aortic aneurysms: A fluid–structure interaction study, *Computers and Structures*, **85**(11–14), 1097 – 1113.
- [28] **Bazilevs, Y., Gohean, J., Hughes, T., Moser, R. and Zhang, Y.** (2009). Patient-specific isogeometric fluid–structure interaction analysis of thoracic aortic blood flow due to implantation of the Jarvik 2000 left ventricular assist device, *Computer Methods in Applied Mechanics and Engineering*, **198**(45–46), 3534 – 3550, models and Methods in Computational Vascular and Cardiovascular Mechanics.
- [29] **Torii, R., Oshima, M., Kobayashi, T., Takagi, K. and Tezduyar, T.** (2008). Fluid–structure interaction modeling of a patient-specific cerebral aneurysm: influence of structural modeling, *Computational Mechanics*, **43**(1), 151–159.
- [30] **Torii, R., Oshima, M., Kobayashi, T., Takagi, K. and Tezduyar, T.E.** (2009). Fluid–structure interaction modeling of blood flow and cerebral aneurysm: Significance of artery and aneurysm shapes, *Computer Methods in Applied Mechanics and Engineering*, **198**(45–46), 3613 – 3621.
- [31] **Bazilevs, Y., Hsu, M.C., Benson, D., Sankaran, S. and Marsden, A.** (2009). Computational fluid–structure interaction: methods and application to a total cavopulmonary connection, *Computational Mechanics*, **45**(1), 77–89.
- [32] **Takizawa, K., Christopher, J., Tezduyar, T.E. and Sathe, S.** (2010). Space–time finite element computation of arterial fluid–structure interactions with patient-specific data, *International Journal for Numerical Methods in Biomedical Engineering*, **26**(1), 101–116.

- [33] **Rissland, P., Alemu, Y., Einav, S., Ricotta, J. and Bluestein, D.** (2009). Abdominal aortic aneurysm risk of rupture: patient-specific FSI simulations using anisotropic model, *Journal of Biomechanical Engineering*, **131**(3).
- [34] **Bazilevs, Y., Hsu, M.C., Zhang, Y., Wang, W., Liang, X., Kvamsdal, T., Brekken, R. and Isaksen, J.** (2010). A fully-coupled fluid-structure interaction simulation of cerebral aneurysms, *Computational Mechanics*, **46**(1), 3–16.
- [35] **Bazilevs, Y., Hsu, M.C., Zhang, Y., Wang, W., Kvamsdal, T., Hentschel, S. and Isaksen, J.** (2010). Computational vascular fluid–structure interaction: methodology and application to cerebral aneurysms, *Biomechanics and Modeling in Mechanobiology*, **9**(4), 481–498.
- [36] **Takizawa, K., Moorman, C., Wright, S., Christopher, J. and Tezduyar, T.** (2010). Wall shear stress calculations in space–time finite element computation of arterial fluid–structure interactions, *Computational Mechanics*, **46**(1), 31–41.
- [37] **Takizawa, K., Moorman, C., Wright, S., Purdue, J., McPhail, T., Chen, P.R., Warren, J. and Tezduyar, T.E.** (2011). Patient-specific arterial fluid–structure interaction modeling of cerebral aneurysms, *International Journal for Numerical Methods in Fluids*, **65**(1-3), 308–323.
- [38] **Isaksen, J.G., Bazilevs, Y., Kvamsdal, T., Zhang, Y., Kaspersen, J.H., Waterloo, K., Romner, B. and Ingebrigtsen, T.** (2008). Determination of Wall Tension in Cerebral Artery Aneurysms by Numerical Simulation, *Stroke*, **39**(12), 3172–3178.
- [39] **Taylor, C. and Humphrey, J.** (2009). Open problems in computational vascular biomechanics: Hemodynamics and arterial wall mechanics, *Computer Methods in Applied Mechanics and Engineering*, **198**, 3514–3523.
- [40] **Holzappel, G.** (2000). *Nonlinear Solid Mechanics: A Continuum Approach for Engineering*, WILEY.
- [41] **Humphrey, J.D.** (2002). *Cardiovascular Solid Mechanics: Cells, Tissues, and Organs*, Springer.
- [42] **Idelsohn, S., Oñate, E. and Pin, F.D.** (2003). A Lagrangian meshless finite element method applied to fluid–structure interaction problems, *Computers and Structures*, **81**(8–11), 655 – 671, k.J Bathe 60th Anniversary Issue.
- [43] **Cottet, G.H., Maitre, E. and Milcent, T.** (2008). Eulerian formulation and level set models for incompressible fluid-structure interaction, *ESAIM-Math. Model. Numer. Anal.*, **42**(3), 471–492.
- [44] **Scovazzi, G. and Hughes, T.** (2007). Lecture notes on continuum mechanics on arbitrary moving domains, **Technical Report**, Sandia National Laboratories, Albuquerque (NM).

- [45] **Hughes, T.J., Liu, W.K. and Zimmermann, T.K.** (1981). Lagrangian-Eulerian finite element formulation for incompressible viscous flows, *Computer Methods in Applied Mechanics and Engineering*, **29**(3), 329 – 349.
- [46] **Donea, J., Giuliani, S. and Halleux, J.** (1982). An arbitrary lagrangian-eulerian finite element method for transient dynamic fluid-structure interactions, *Computer Methods in Applied Mechanics and Engineering*, **33**(1–3), 689 – 723.
- [47] **Tezduyar, T., Behr, M. and Liou, J.** (1992). A new strategy for finite element computations involving moving boundaries and interfaces—The deforming-spatial-domain/space-time procedure: I. The concept and the preliminary numerical tests, *Computer Methods in Applied Mechanics and Engineering*, **94**(3), 339 – 351.
- [48] **Mittal, S. and Tezduyar, T.** (1994). Massively parallel finite element computation of incompressible flows involving fluid-body interactions, *Computer Methods in Applied Mechanics and Engineering*, **112**(1–4), 253 – 282.
- [49] **Farhat, C., Geuzaine, P. and Grandmont, C.** (2001). The Discrete Geometric Conservation Law and the Nonlinear Stability of ALE Schemes for the Solution of Flow Problems on Moving Grids, *Journal of Computational Physics*, **174**(2), 669 – 694.
- [50] **Farhat, C. and Geuzaine, P.** (2004). Design and analysis of robust ALE time-integrators for the solution of unsteady flow problems on moving grids, *Computer Methods in Applied Mechanics and Engineering*, **193**(39–41), 4073 – 4095, the Arbitrary Lagrangian-Eulerian Formulation.
- [51] **Taltec, P.L. and Mouro, J.** (2001). Fluid structure interaction with large structural displacements, *Computer Methods in Applied Mechanics and Engineering*, **190**(24–25), 3039 – 3067, advances in Computational Methods for Fluid-Structure Interaction.
- [52] **Leuprecht, A., Perktold, K., Prosi, M., Berk, T., Trubel, W. and Schima, H.** (2002). Numerical study of hemodynamics and wall mechanics in distal end-to-side anastomoses of bypass grafts, *Journal of Biomechanics*, **35**(2), 225 – 236.
- [53] **Leuprecht, A., Kozerke, S., Boesiger, P. and Perktold, K.** (2003). Blood flow in the human ascending aorta: a combined MRI and CFD study, *Journal of Engineering Mathematics*, **47**(3–4), 387–404.
- [54] **Heil, M.** (2004). An efficient solver for the fully coupled solution of large-displacement fluid–structure interaction problems, *Computer Methods in Applied Mechanics and Engineering*, **193**(1–2), 1 – 23.
- [55] **Quarteroni, A., Tuveri, M. and Veneziani, A.** (2000). Computational vascular fluid dynamics: problems, models and methods, *Computing and Visualization in Science*, **2**(4), 163–97.
- [56] **Grandmont, C. and Maday, Y.** (2000). Fluid-Structure Interaction: A Theoretical Point of View, *Revue Européenne des Éléments*, **9**(6–7), 633–653.

- [57] **Hart, J.D., Baaijens, F., Peters, G. and Schreurs, P.** (2003). A computational fluid-structure interaction analysis of a fiber-reinforced stentless aortic valve, *Journal of Biomechanics*, **36**(5), 699 – 712, cardiovascular Biomechanics.
- [58] **Peskin, C. and McQueen, D.** (1995). A general method for the computer simulation of biological systems interacting with fluids, *Symposia of the Society for Experimental Biology*, **49**, 265–276.
- [59] **Ángel Fernández, M. and Tallec, P.L.** (2003). Linear stability analysis in fluid–structure interaction with transpiration. Part II: Numerical analysis and applications, *Computer Methods in Applied Mechanics and Engineering*, **192**(43), 4837 – 4873.
- [60] **Deparis, S., Fernández, M.A. and Formaggia, L.** (2003). Acceleration of a fixed point algorithm for fluid-structure interaction using transpiration conditions, *ESAIM: Mathematical Modelling and Numerical Analysis*, **37**, 601–616.
- [61] **Zhou, M., Sahni, O., Kim, H., Figueroa, C., Taylor, C., Shephard, M. and Jansen, K.** (2010). Cardiovascular flow simulation at extreme scale, *Computational Mechanics*, **46**(1), 71–82.
- [62] **Turkeri, H., Piskin, S. and Celebi, M.S.** (2011). A comparison between non-Newtonian and Newtonian blood viscosity models, *Journal of Biomechanics*, **44**, *Supplement 1*(0), 17 –, abstracts of the Fifth International Participated National Biomechanics Congress Fifth International Participated National Biomechanics Congress.
- [63] **Demir, G., Dogan, F. and Celebi, M.S.** (2011). Calculation of material coefficients of viscoelastic gel for validating soft tissue deformations, *Journal of Biomechanics*, **44**, *Supplement 1*(0), 16 –, abstracts of the Fifth International Participated National Biomechanics Congress Fifth International Participated National Biomechanics Congress.
- [64] **Piskin, S. and Celebi, M.S.** (2013). Analysis of the effects of different pulsatile inlet profiles on the hemodynamical properties of blood flow in patient specific carotid artery with stenosis, *Computers in Biology and Medicine*, **43**(6), 717–728.

CURRICULUM VITAE



Name Surname: Yağmur GÜLKANAT

Place and Date of Birth: Sivas, 1987

E-Mail: yagmurgulkanat87@gmail.com, yagmur.gulkanat@be.itu.edu.tr

B.Sc.: Ege University, Faculty of Science, Mathematics (2011)

M.Sc.: Istanbul Technical University, Informatics Institute, Computational Science and Engineering (2014)